Hochschule für Angewandte Wissenschaften Hamburg
Hamburg University of Applied Sciences

Masterarbeit

Jonathan Hilger

Nonlinear Aeroelastic Simulations and Stability Analysis of a Highly Flexible Wing

Fakultät Technik und Informatik
Department Fahrzeugtechnik und Flugzeugbau

Faculty of Engineering and Computer Science
Department of Automotive and Aeronautical Engineering

Jonathan Hilger

Nonlinear Aeroelastic Simulations and Stability Analysis of a Highly Flexible Wing

Masterarbeit eingereicht im Rahmen der Masterprüfung

im Studiengang Flugzeugbau
am Department Fahrzeugtechnik und Flugzeugbau
der Fakultät Technik und Informatik
der Hochschule für Angewandte Wissenschaften Hamburg

in Zusammenarbeit mit:
Deutsches Zentrum für Luft- und Raumfahrt
Institut für Aeroelastik, Abteilung Lastanalyse und Entwurf
Bunsenstraße 10
37073 Göttingen

Erstprüfer: Prof. Dr.-Ing Hartmut Zingel
Zweitprüfer: Dr.-Ing. Markus Ritter

Abgabedatum: 28.01.2021

Jonathan Hilger

Title of Thesis

Nonlinear Aeroelastic Simulations and Stability Analysis of a Highly Flexible Wing

Keywords

Aeroelasticity, Vortex Lattice Method, Geometric Nonlinearities, Large Deformations, FEM, Linearisation, Discrete-time State-space Model, Stability Analysis

Abstract

The goal of this thesis is the extension of the existing simulation tools at DLR and their application for aeroelastic modelling and validation of the highly flexible Pazy wing wind tunnel model. As large deformations are expected due to the wing's special design, the simulations should in particular account for the nonlinear behaviour of force-structure interaction (follower force problem) and geometric nonlinearities. Therefore, an aeroelastic solver developed at DLR is used, coupling a geometrically nonlinear vortex lattice method with the nonlinear static solution sequence SOL400 of the finite element solver Nastran. Besides determining steady aeroelastic equilibrium points by the means of this solver, the aeroelastic stability of the wing in terms of flutter is also to be investigated. Since common flutter speed prediction methods are only applicable to rigid structures undergoing small deformations, an important part of this thesis is the development of a method for stability analysis of highly flexible wings. Therefore, the whole aeroelastic system is linearised at static equilibrium points with large deformations using linear discrete-time state-space models. The proposed method is then verificated using nonlinear simulation tools in the time domain. Subsequently, static coupling simulations are performed for a range of onflow velocities and angles of attack. Since the structural properties are affected by the deformation of the wing, the change of mode shapes and eigenvalues is evaluated afterwards as a function of the deformation. Finally, the aeroelastic stability of the wing is determined by means of the proposed method. The results are validated with reference results obtained from the Nastran aeroelastic flutter analysis solver SOL145 and with data computed by an approach similar to the method developed in this thesis.

Jonathan Hilger

Thema der Arbeit

Nichtlineare aeroelastische Simulationen und Stabilitätsanalyse für einen hochflexiblen Flügel

Stichworte
Aeroelastik, Wirbelleiterverfahren, Geometrische Nichtlinearitäten, Große Deformationen, FEM, Linearisierung, Zeitdiskretes Zustandsraummodell, Stabilitätsanalyse

Kurzzusammenfassung

Das Ziel dieser Arbeit ist die Erweiterung der bereits existierenden Simulationstools am DLR und ihre Anwendung zur aeroelastischen Modellierung und Validierung des hochflexiblen Pazy Wing Windkanalmodells. Da aufgrund des speziellen Designs des Flügels große Deformationen erwartet werden, sollten die Simulationen vor allen Dingen das nichtlineare Verhalten der Kraft-Struktur-Interaktion (follower force problem) und geometrische Nichtlinearitäten berücksichtigen. Zu diesem Zweck wird ein am DLR entwickelter aeroelastischer Solver verwendet, der ein geometrisch nichtlineares Wirbelleiterverfahren mit der nichtlinearen statischen Lösungssequenz SOL400 des FEM-Lösers Nastran koppelt. Neben der Bestimmung stationärer aeroelastischer Gleichgewichtspunkte wird die aeroelastische Stabilität des Flügels in Bezug auf Flattern untersucht. Da herkömmliche Flatterlöser nur auf starre Strukturen, die kleine Verformungen aufweisen, angewendet werden können, besteht ein wichtiger Teil dieser Arbeit aus der Entwicklung einer Methode zur Stabilitätsanalyse hochflexibler Flügel. Folglich wird das gesamte aeroelastische System um statische Gleichgewichtspunkte mit großen Deformationen linearisiert. Hierfür wird ein lineares zeitdiskretes Zustandsraummodell verwendet. Die vorgeschlagene Methode wird anschließend mit Hilfe nichtlinearer Simluationstools im Zeitbereich verifiziert. Die statisch gekoppelten Simulationen werden für eine Reihe verschiedener Anströmgeschwindigkeiten und Anstellwinkel durchgeführt. Da die strukturellen Eigenschaften durch die Deformation des Flügels beeinflusst werden, wird die Änderung der Eigenformen und -frequenzen in Abhängigkeit der Deformation untersucht. Abschließend wird die vorgestellte Methode zur aeroelastischen Stabilitätsanalyse des Flügels verwendet. Die Ergebnisse werden mit Referenzergebnissen aus dem Flatterlöser SOL145 in Nastran und mit Daten aus einem zur entwickelten Methode ähnlichen Verfahren validiert.

Acknowledgements

I would like to thank several people without whose support and guidance this thesis could not have been possible. First I want to thank Professor Hartmut Zingel not only for supervising this thesis as well as other major projects in the course of my studies, but also for taking the time and effort to motivate me to complete them. He clearly inspired my interest in aerodynamics and aeroelasticity. I am also very thankful to my supervisor Markus Ritter at DLR for his excellent guidance and support for this thesis, as well as his leadership of the Large Deflection Working Group. His proposal of this topic and the collegial working atmosphere have taken significant influence on both the enjoyment and quality of this work. Especially the numerous and detailed discussions about the linearisation were particularly important for the progress of this project. I am very much looking forward to working with him in the future. Furthermore, I would thankfully like to mention the members of the Large Deflection Working Group of the 3rd Aeroelastic Prediction Workshop for their contributions to the work on the Pazy wing: the colleagues from Technion for providing simulation models and experimental data and the colleagues from Imperial College London for sharing computational results.

I will always be grateful to my girlfriend Anne for her immense support, her continuous patience and for accepting the numerous hours I spend on this document. Finally, I would like to thank my parents for their ongoing motivation and for believing in the success of my studies. Without their immeasurable support this thesis would not have been written.

Contents

List of Figures

List of Tables

List of Abbreviations

AIC	Aerodynamic Influence Coefficients
AoA	Angle of Attack
CBEAM	MSC Nastran finite beam element
CFD	Computational Fluid Dynamics
CFRP	Carbon Fibre Reinforce Plastic
CQUAD4/CTRIA3	MSC Nastran finite shell element
DLM	Doublet Lattice Method
DLR	Deutsches Zentrum fuer Luft- und Raumfahrt, German Aerospace Center
DOF	Degree of Freedom
FEM	Finite Element Method
FSI	Fluid-structure Interaction
HALE	High Altitude Long Endurance
IP	In-plane
LCO	Limit Cycle Oscillation
LTI	Linear Time Invariant
MSC	MSC Software Corporation
NACA	National Advisory Committee for Aeronautics
Nastran	NASA Structural Analysis, commercial finite element analysis software
OOP	Out-of-plane
RHS	Right Hand Side
SHARPy	Simulation of High-Aspect Ratio aeroplanes in Python, aeroelastic simulation toolbox developed at Imperial College London
SOL145	MSC Nastran aeroelastic flutter solution sequence
SOL400	MSC Nastran nonlinear solution sequence
SPC1	MSC Nastran single point constraint
UAV	Unmanned Aerial Vehicle
w.r.t.	with respect to
WIC	Wake Influence Coefficients

List of Symbols

Latin Symbols and Scalars

A_p	Area of aerodynamic panel
a_w	Lift curve slope
b	Wing span
c	Wing chord
ec	Distance between aerodynamic centre and elastic axis
f	Frequency
GJ	Torsional stiffness
k	Reduced frequency
L	Lift
q	Dynamic pressure
s	Wing span
t	Time
u, v, w	Velocity components in x, y and z direction
V	Airspeed
x	Coordinate in chordwise direction
x, y, z	General notation for axes in cartesian coordinates
y	Coordinate in spanwise direction
z	Eigenvalue of discrete-time state-space system
Δt	Time step size

Greek Symbols

∇	Nabla Operator
∂	Partial derivative
∇^2	Laplace operator
α	Angle of Attack
θ	Twist angle
λ	Structural eigenvalue; Eigenvalue of continuous-time state-space system

ρ	Fluid density
ψ	IP bending angle
ω	Natural frequency
ϵ	Scaling factor of eigenvectors
ϕ	Velocity potential; OOP bending angle

Indices

∞	Undisturbed onflow conditions
A	aerodynamic
b	bound
c	w.r.t. collocation point
d	Displacement transfer
D	Induced drag component
eff	effective
el	elastic
f	Force transfer
n	Discrete time step
p	Panel
q	w.r.t. quarter point
rb	Rigid body
s	Steady component
S	structural
u	Unsteady component
w	Wake

Matrices and Vectors

$\boldsymbol{A}$	Dynamics matrix
$\boldsymbol{AIC}$	Aerodynamic influence coefficients matrix
$\boldsymbol{B}$	Control matrix/Input matrix
$\boldsymbol{C}$	Sensor matrix/Output matrix
$\boldsymbol{D}$	Damping matrix; Direct term/Feed-through Matrix
$\bar{\boldsymbol{D}}$	Generalised damping matrix
$\boldsymbol{F}$	Force vector of aerodynamic panel; Discrete nodal forces
$\boldsymbol{f}$	External nodal loads vector; Forces vector
$\bar{\boldsymbol{f}}$	Generalised forces vector
$\boldsymbol{H}$	Coupling matrix
$\boldsymbol{I}$	Identity matrix

$\boldsymbol{K}$	Stiffness matrix
$\bar{\boldsymbol{K}}$	Generalised stiffness matrix
$\boldsymbol{M}$	Mass matrix; Shifting matrix for wake-shedding process; Interpolation matrix
$\bar{\boldsymbol{M}}$	Generalised mass matrix
$\tilde{\boldsymbol{n}}$	Equivalent matrix of normal vectors of all aerodynamic panels
$\boldsymbol{n}$	Normal vector of aerodynamic panel
$\boldsymbol{q}$	Vector of generalised coordinates
$\boldsymbol{r}$	Internal nodal forces vector; Quarter chord line vector of aerodynamic panel
$\boldsymbol{R}$	Skew-symmetric matrix of vector $\boldsymbol{r}$
$\tilde{\boldsymbol{R}}$	Equivalent matrix of skew-symmetric matrices all aerodynamic panels
$\boldsymbol{RHS}$	Vector of kinematic boundary conditions at collocation points of aerodynamic panels
$\boldsymbol{u}$	Input vector; Flow velocity vector; Nodal displacement vector; Displacement field
$\boldsymbol{u}_b$	Velocity vector at collocation point of aerodynamic panel
$\boldsymbol{v}$	Eigenvector of state-space system
$\boldsymbol{V}_{bodystreamwise}$	Velocity of aerodynamic panel induced by streamwise segments of bound vortex rings and all segments of wake vortex rings
$\boldsymbol{V}_{el}$	Velocity of aerodynamic panel induced by structural deformation
$\boldsymbol{V}_{gust}$	Velocity of aerodynamic panel induced by gust
$\boldsymbol{V}_{rb}$	Velocity of aerodynamic panel due to onflow velocity and rigid body motion
$\tilde{\boldsymbol{V}}_{rb}$	Equivalent matrix of rigid body velocity vectors of all aerodynamic panels
$\boldsymbol{V}_{wake}$	Velocity of aerodynamic panel induced by wake panels
$\boldsymbol{WIC}$	Wake influence coefficients matrix
$\boldsymbol{x}$	State vector
$\boldsymbol{y}$	Output vector
$\boldsymbol{\Gamma}$	Vector of circulations of aerodynamic panels
$\boldsymbol{\Phi}$	Eigenvectors of structural modes (modal matrix)
$\boldsymbol{\Omega}$	Matrix of natural eigenvalues

1 Introduction

1.1 Motivation

In cooperation with the German Aerospace Center (DLR) and others, the University of Manchester published a study in September 2020, reporting on "The Contribution of global aviation to anthropogenic climate forcing for 2000 to 2018" [1]. It was estimated that the cumulative emissions of global aviation between 1940 and 2018 are 32.6 billion tonnes of CO_2 and account for 1.5% of total anthropogenic CO_2-Emissions in history. Approximately 50% of this amount was emitted in the last 20 years, with emissions from aviation representing 2.4% of global anthropogenic CO_2-Emissions in 2018 [1]. Until the beginning of the COVID-19 pandemic in 2020, strong growth of global aviation was expected to maintain current levels and to be dependent on the combustion of fossil fuels for some considerable time into the future. As a consequence of this and in response to the Paris Agreement the International Civil Aviation Organization (ICAO) developed the Carbon Offsetting and Reduction Scheme for International Aviation (CORSIA), which was adopted by the involved states in 2016. The two main goals of this global market-based measure scheme are to improve energy efficiency by 2% per year until 2050 and to achieve carbon neutral growth from 2020 onwards [2, 3]. Furthermore, Airbus announced the ZeroE programme, revealing three concept aircraft powered by hydrogen with the ambition to develop a zero-emission commercial aircraft by 2035 [4].

The striving for higher fuel efficiency already led to an increased use of Carbon Fibre Reinforced Plastics (CFRP) in aircraft components over the last decade. In order to achieve the ambitious goals mentioned above, however, the importance of lightweight structures will further increase in the future. In addition to the construction of entire airframes using composite materials, recent developments have shown an increasing flexibility of flight vehicles [5, 6]. This is not only the case for Unmanned Aerial Vehicles (UAV) but also for large transport aircraft and can bring advantages in terms of airframe stress and passenger comfort [7]. In addition, achieving higher efficiency by reducing the induced drag requires a wing with a high aspect ratio. This

leads to an increased wing span and thus to greater flexibility of the wing, especially if a lightweight structure of composite materials is used, which is mainly the case for UAVs and sail planes [8]. Thus, the geometrical nonlinearities due to large deformations have to be taken into account in the design process. From an aeroelastic point of view, the existing linear methods may therefore no longer be suitable to describe the behaviour of very flexible flight vehicle configurations. A remarkable example in this context is the Helios mishap in 2003. The Helios Prototype shown in Fig. 1.1 was a solar-powered High Altitude Long Endurance (HALE) UAV developed by Aero-Vironment under NASA's Environmental Aircraft and Sensor Technology (ERAST) programme. On a remotely piloted flight, the aircraft encountered turbulence and turned into a persistent high-dihedral configuration, which caused very divergent pitch mode oscillations. Due to the exceeding air speed, the wing leading edge structure on the outer wing failed and the aircraft was destroyed in flight. Two root causes were identified following the mishap report [9]:

- "Lack of adequate analysis methods led to an inaccurate risk assessment of the effects of configuration changes leading to an inappropriate decision to fly an aircraft configuration highly sensitive to disturbances."
- "Configuration changes to the aircraft, driven by programmatic and technological constraints, altered the aircraft from a spanloader to a highly point-loaded mass distribution on the same structure significantly reducing design robustness and margins of safety."

One of the key recommendations was the development of multidisciplinary (structures, aerodynamic, controls, etc) models, which can describe the nonlinear dynamic behaviour of aircraft modifications, as well as more advanced *time-domain* analysis methods appropriate to highly-flexible, morphing vehicles [9]. As a result, the development of nonlinear models and analysis methods has become significantly more important in the global aeroelastic community. Hence, nonlinearities of highly flexible flight vehicles are a current field of research at the Institute of Aeroelasticity at DLR in Göttingen. Besides various aerodynamic nonlinearities known and investigated so far, interest is focused mainly on structural nonlinearities caused by geometrically large deformations. This is the case, since the capabilities of current aerodynamic analysis, such as CFD methods, are already far advanced, but there is a lack of adequate methods on the structural side. Most common aeroelastic simulation tools are still based on a linear description of the airframe and are expressed in the frequency domain. Therefore, recent studies on flexible aircraft and wing structures often use and improve nonlinear modal approaches to account for structural effects of large

Figure 1.1: NASA's Helios HP01 High-Altitude Configuration during flight [9]

deformations, e.g. in references [10], [11] and [8]. However, both the analysis of aeroelastic systems as well as their optimisation require sufficient methods to predict and possibly use structural nonlinearities, e.g. for passive load alleviation.

For this purpose, the Large Deflection Working Group was formed as part of the *3rd Aeroelastic Prediction Workshop* initiated by NASA. Objective of this group is the aeroelastic investigation of the highly flexible Pazy wing wind tunnel model, which was designed at the Technion - Israel Institute of Technology. Due to the design of the model, very large static deformations are generated at corresponding dynamic pressures and angles of attack in the wind tunnel. Furthermore, the aeroelastic stability in terms of flutter behaviour shall be determined at large deformations.

1.2 Objectives of this thesis

The main goal of this thesis is the extension of the existing simulation tools at DLR and their application for aeroelastic modelling and validation of the Pazy wing wind tunnel model. After familiarisation with the model and the theoretical fundamentals, steady static coupling simulations for a range of dynamic pressures and angles of attack will be performed. Therefore an aeroelastic solver developed at the Institute of Aeroelasticity will be used, which couples a vortex lattice method with the commercial finite element solver MSC Nastran. An incompressible flow field can be assumed regarding the operating range of the wing, thus potential-based methods should be suitable to

describe the steady and unsteady aerodynamics of the system. The geometrical nonlinearities will be taken into account by using the nonlinear Nastran SOL400 sequence. Since the structural properties are affected by the deformation of the wing, the change of mode shapes and eigenvalues will be determined afterwards as a function of the deformation. A very important part of this work will be the linearisation of the whole aeroelastic system at static equilibrium points with large deformations. This will be done by describing the aeroelastic system by a linear state-space model, which can then be used to determine the aeroelastic stability at this equilibrium point. In addition, the influence of the structural nonlinearities on the stability shall be investigated. Overall, an extension of the existing aeroelastic solver is required to implement the developed method for stability analysis.

The theoretical fundamentals for this thesis are presented in Chapter 2. After a short introduction on aircraft aeroelasticity, the unsteady and steady vortex lattice method used for the aerodynamic modelling are explained. This is followed by a description of the structural dynamics, where nonlinear finite element methods as well as the normal modes analysis of nonlinear methods and the modal approach are addressed. The chapter is then closed with an overview of fluid-structure interaction. The derivation of the linearised method for stability analysis itself is part of Chapter 3. It begins with a detailed description of the framework of the aeroelastic solver, accounting for both the basic aerodynamic solver as well as the interface of the aerodynamic and structural model. Afterwards, the linearisation of the aeroelastic system is explained, starting with the basics of linear state-space models, which will then be used for the derivation of the aerodynamic and finally the whole aeroelastic model. Chapter 4 includes a documentation of the verification and validation of the linearisation. The verification of the aerodyamic model is done by the application of an unsteady vortex lattice solver in the time domain, the aeroelastic model is verified by a modal solver. Furthermore, the linearised method is validated using the aeroelastic flutter analysis solver SOL145 in Nastran. The results of the Pazy wing test case are presented subsequently, with an introduction of the key features of the model at first, followed by the steady static coupling simulations. In addition, the influence of large deformations on structural properties as well as the results of the aeroelastic stability analysis are discussed later on. A validation of the test case with computational results contributed by other members of the Large Deflection Working Group concludes Chapter 4. Finally, a conclusion and an outlook for future research on the topic of this thesis are given in Chapter 5.

2 Theoretical Fundamentals

2.1 Introduction to Aircraft Aeroelasticity

The interaction of aerodynamics, inertial and elastic forces are described in the subject of aeroelasticity. Besides various examples from nature, aeroelastic phenomena also occur in many areas of technology. Due to the flexibility of (especially modern) aircraft structures, structural deformations induce additional aerodynamic forces, which in turn result in additional structural deformations. These interactions may result in a stable state of equilibrium, but may also tend to cause static or dynamic instabilities under certain conditions. In the history of aviation, the first recorded aeroelastic phenomenon appeared on the Handley-Page 0/400 bomber in 1916, which encountered tail flutter. While this aircraft was a biplane construction, the first aeroelastic wing problems occurred mainly due to the development of monoplanes with higher speeds at the end of World War I and led to first specific aeroelastic investigations. Since then rapid technological advances in aerospace engineering have brought new challenging problems to light, so that aeroelastic effects have had a major influence on aircraft design. Nowadays, this is the case in the design of structural members as well as in mass distribution, lifting surface planforms and control system design [12, 13].

In general, aeroelasticity can be divided into static and dynamic aeroelastic problems. The former include phenomena where interactions between aerodynamic and elastic forces are involved. In addition, the latter are referred to as phenomena involving interactions among inertial, aerodynamic and elastic forces. The various problems have been classified by Collar [14] by means of a triangle of forces, as seen in Fig. 2.1. Therein, aerodynamic, elastic and inertial forces are placed at the vertices of a triangle and the different aeroelastic phenomena are located depending on the forces involved. Thus, static aeroelastic problems, such as divergence, lie outside of the triangle, whereas dynamic problems, for example flutter, lie within the triangle. Although all of these phenomena have to be considered in the design process, some of them may be more important than others [12].

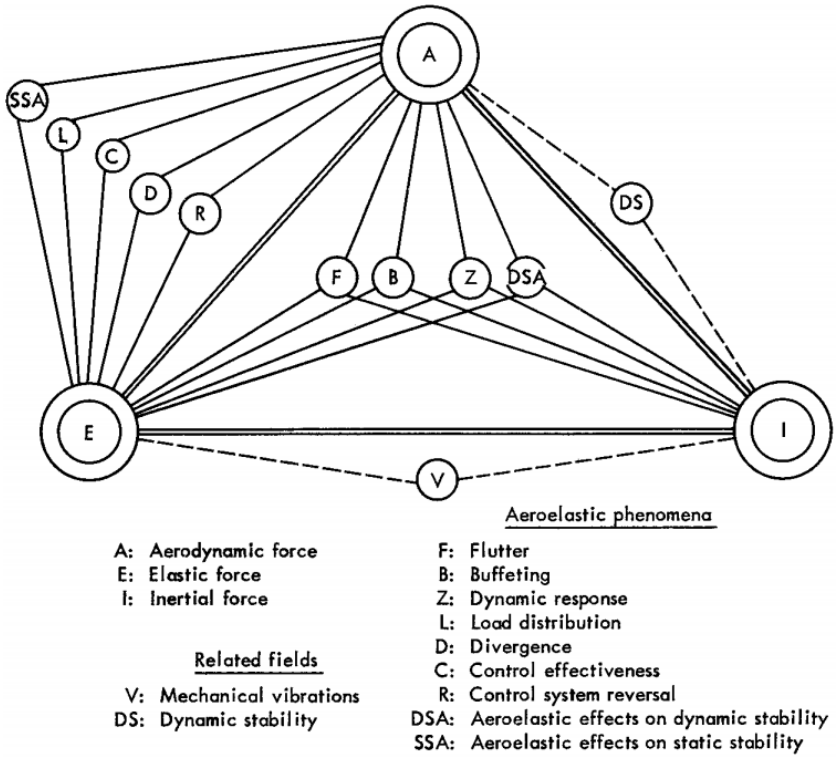

Figure 2.1: Collar's aeroelastic triangle of forces [12]

In case of static aeroelasticity, one of the most common problems is wing torsional *divergence*. Considering a straight wing with the centre of twist located behind the aerodynamic centre, the torsional divergence speed is reached, when the "increment in aerodynamic torsional moment due to an arbitrary increment in twist angle is exactly equal to the increment of elastic restoring torque" [12]. Exceeding this speed causes the increment in aerodynamic torsional moment to exceed the increment in elastic restoring torque, resulting in static instability of the wing. A common approach to raise the divergence speed is to move the centre of twist forward to reduce the distance between centre of twist and aerodynamic centre. Another important effect of static aeroelasticity is *control system reversal*. For example, a downward or upward deflection of the aileron normally leads to increased or decreased lift on the wing, hence producing a rolling moment. However, the aileron deflections also cause an elastic deformation of the wing (wing twist due to an additional aerodynamic moment caused by a change of camber), resulting in a decrease or increase of angle of attack. This counteracts the desired effect of the aileron deflection and reduces the rolling moment. While the wing twist moment increases with increasing speed, the elastic restoring torque remains constant. It is obvious that there exists a speed similar to

the divergence speed, where aileron deflections will not produce a rolling moment any more and thus is called aileron reversal speed. When this speed is exceeded, the effect of ailerons is actually reversed [12].

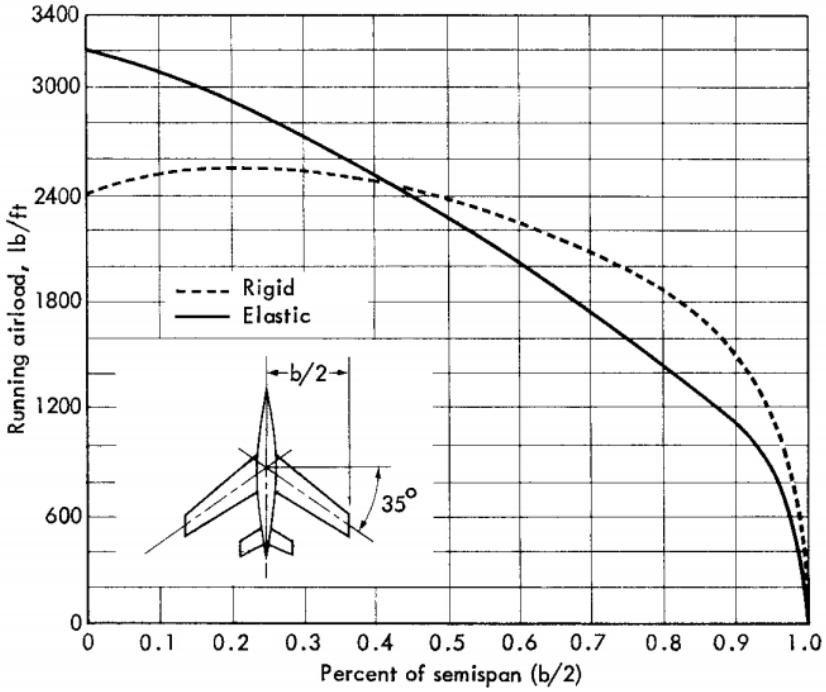

Figure 2.2: Airload distribution on swept rigid and elastic wing for same total lift [12]

Taking into account the increased use of highly flexible structures in aerospace industry, *load distribution* is also becoming increasingly important. Especially large deformations of the structure may cause a redistribution of airloads and lead to a very different lift distribution than that computed assuming complete rigidity, as can be seen in Fig. 2.2. Under consideration of a wing with the centre of twist behind the aerodynamic centre, the lift at the aerodynamic centre and the resulting torsional moment tend to twist the wing and thus increase the angle of attack. This raises the lift further, causing another increment in twist. The increments of twist and lift become smaller, reaching a stable equilibrium known as static aeroelastic equilibrium, as long as speed remains below the divergence speed. For a swept wing, as shown in Fig. 2.2, the centre of pressure is shifted towards the root of the wing due to the deformations, whereas in case of a straight wing like the Pazy wing, loads are redistributed mainly outboard of the wing, which is discussed in Section 4.2 and following [12].

In terms of dynamic aeroelasticity, *flutter* is maybe one of the most important aeroelastic phenomena. In general, flutter can be described as an "unstable self-excited vibration in which the structure extracts energy from the air and often results in

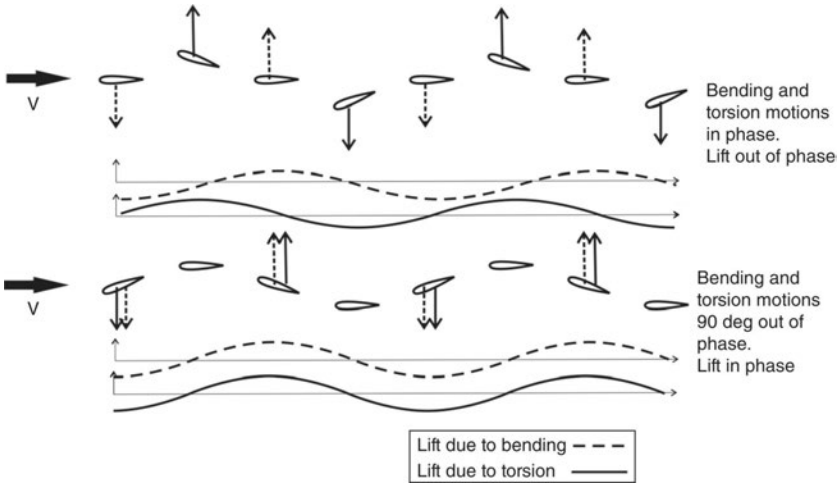

Figure 2.3: Lift components due to different phasing of bending and torsion motion [13]

catastrophic structural failure" [13]. The classical binary type of flutter is caused by an unfavourable coupling of two modes of vibration due to the associated aerodynamic forces. When some critical speed, called flutter speed, is reached, any initial disturbance results in structural oscillations, which are damped out below the flutter speed. Above the flutter speed, normally one of the modes becomes undamped and growing oscillations occur, often leading to structural failure. Typical forms of flutter involve two interacting modes, e.g. wing bending/torsion as shown in Fig. 2.3, wing torsion/control surface or wing/engine. To prevent flutter or increase the flutter speed, common measures include an increased stiffness, especially torsional stiffness and adjustments in mass distribution. Besides flutter, there are another two important phenomena that should be mentioned when speaking of dynamic aeroelasticity. One of these is called *buffeting*, which can be described as highly-frequent vibrations, for example in the tail due to aerodynamic impulses from the wing wake, often encountered by fighter aircraft during high speed pull-up manoeuvrers. At last, *dynamic response* problems have to be considered primarily in the structural design. The two main problems of this category are gust and landing problems, with the gust condition usually controlling the strength condition in large aircraft [12, 13].

Since this thesis deals with the development of a method for stability analysis of highly flexible wings, the next sections will focus on the effect of wing flexibility on lift distribution. Furthermore, a brief overview on different methods of flutter prediction will be given.

2.1.1 Static Aeroelastic Behaviour of a Flexible Wing

In the following, a flexible rectangular wing fixed at the root with semi-span *s*, chord *c*, a symmetric airfoil section and the flexural axis at distance *ec* behind the aerodynamic centre is considered. The wing torsional stiffness is *GJ* and with application of the aerodynamic strip theory, the lift curve slope is given as a_w. For simplification, the wing twist is assumed to be linear by the relation [13]

$$\theta = \frac{y}{s}\theta_T \ , \tag{2.1}$$

with θ_T being the twist at the wing tip and y being the variable coordinate in spanwise direction. Accordingly, the twist increases with distance from the wing root. Using aerodynamic strip theory, the lift of an elemental strip can be determined by

$$dL = q\, c\, a_w \left(\theta_0 + \frac{y}{s}\theta_T\right) dy \ , \tag{2.2}$$

where q is the dynamic pressure and θ_0 is the wing root incidence. Thus the lift also increases with distance from the wing root. The calculation of the total lift on the wing is done by integrating over the wing semi-span and is used for further derivation of the elastic tip twist, finally resulting in

$$\theta_T = \frac{3q\, ec^2 s^2 a_w}{6GJ - 2q\, ec^2 s^2 a_w}\theta_0 \ . \tag{2.3}$$

As already mentioned above, the aerodynamic torsional moment will overcome the elastic restoring torque when divergence is reached, causing the twist to tend to infinity and the structure to be destroyed. The critical divergence speed or dynamic pressure is given by

$$q_w = \frac{3GJ}{ec^2 s^2 a_w} \ . \tag{2.4}$$

It can be seen, that the divergence speed can be increased either by reducing the distance ec between flexural axis and aerodynamic centre or increasing the torsional rigidity GJ. If the flexural axis lies on or before the aerodynamic centre, the aerodynamic moment is zero or becomes negative, thus no divergence will occur. From a design point of view, however, only the first two measurements can be used and therefore divergence always has to be taken into account in the aeroelastic design process. With the wing twist being determined, the lift distribution can be determined

by calculating the lift per unit span, which is found as

$$\frac{dL}{dy} = q\, c a_w \left(1 + \frac{3\,(q/q_w)}{2\,(1-(q/q_w))}\frac{y}{s}\right)\theta_0\ . \tag{2.5}$$

Again, the total lift is computed by integrating Eq. (2.5) along the wing semi-span. A closer look reveals that the lift per unit span is linear dependent on the spanwise coordinate and increases along the wing span. The linearity is due to the assumption of a linear relation between twist and spanwise coordinate in Eq. (2.1) and is basically only valid for simple wing shapes, e.g. rectangular wings subjected to a single tip loading. For a highly flexible wing undergoing large deformations, which is subject of this thesis, it is obvious that the wing twist behaves in a strongly nonlinear manner, as can be seen in Section 4.2. The increment in lift is then no longer only dependent on the incremental twist, but also affected by the change of local incidence due to the wing bending deflection. However, the above equations and theoretical fundamentals have been included for the sake of completeness and to give an overview on simple divergence estimation. Although the explained method is not applicable to very flexible wings, the principles of divergence and wing twist are also valid for an elastic rectangular wing. Further derivations can be found in reference [13].

2.1.2 Standard Flutter Speed Prediction Methods

Over the years a range of different methods for flutter prediction has been developed, which will be briefly discussed in this section. Therefore some additional principles of unsteady aerodynamics have to be mentioned first. Considering a two-dimensional airfoil with chord c at a small initial angle of incidence α and air speed V, the effect of an instantaneous change in angle of incidence $\Delta\alpha = \alpha/2$ is investigated. In case of a quasi-steady aerodynamic model, the lift would instantaneously increase to the new lift value caused by the change of incidence. When an unsteady model is used, the lift instantaneously changes to half of the additional lift due to $\Delta\alpha$, as shown in Fig. 2.4a. The lift then increases asymptotically, reaching 90% of the steady value approximately 15 semi-chords behind the change of incidence. This time dependent change of lift due to a change of incidence can be modelled with *Wagner's function*. In the next step, the airfoil is now considered in sinusoidal pitch oscillation with frequency ω. For this particular case it is seen that the magnitude of the unsteady forces is reduced (compared to the quasi-steady forces) and a phase lag is introduced between the airfoil motion and the unsteady forces. In addition, the magnitude of forces decrease and the phase lag changes with increasing frequency, according to Fig. 2.4b. The

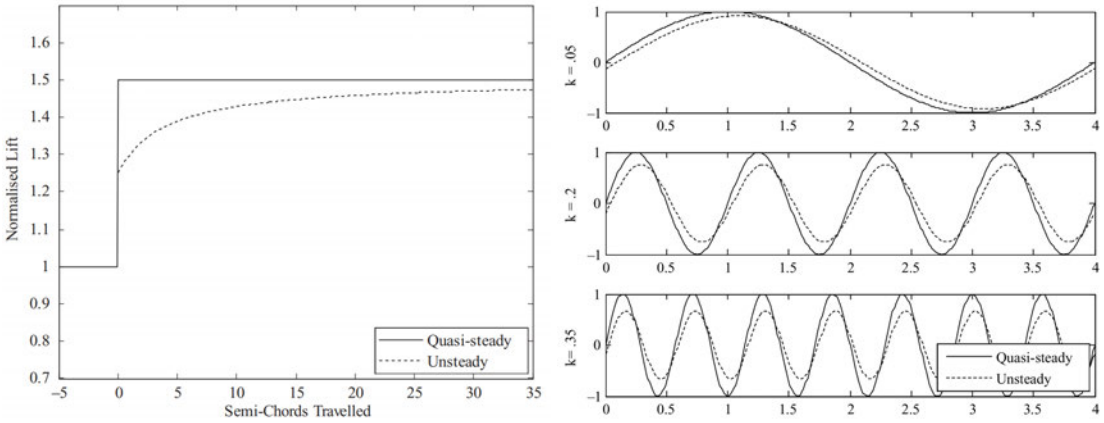

(a) Wagner's function (b) oscillating airfoil

Figure 2.4: Change of lift due to an instantaneous change in angle of incidence (a) and comparison of unsteady and steady lift for airfoil pitch oscillation at different reduced frequencies (b) [13]

amplitude and phase lag changes are a function of the so-called reduced frequency k, which describes "the number of oscillations undergone by the airfoil during the time taken for the airflow to travel across the chord of the airfoil, multiplied by 2π" [13]. It is found by

$$k = \frac{\omega b}{V} = \frac{\omega}{V}\frac{c}{2}\,, \tag{2.6}$$

where b is the semi-chord and V is the air speed. The changes in amplitude and phase between the sinusoidal unsteady aerodynamic forces and the quasi-steady forces are modelled using the complex *Theodorsen's function* $C(k)$. Shown in figure Fig. 2.5, the real part or magnitude of Theodorsen's function decreases as k increases, while the imaginary part or phase lag increases until $k = 0.3$ and is then reduced again.

Based on the provided background material, a short overview of the flutter equations in general and some specific methods for flutter calculation in particular shall be presented. The classical or general form of aeroelastic equations of motion considering both the aerodynamic forces and the structural equations is [13]

$$\boldsymbol{A}\ddot{\boldsymbol{q}} + (\rho V \boldsymbol{B} + \boldsymbol{D})\,\dot{\boldsymbol{q}} + \left(\rho V^2 \boldsymbol{C} + \boldsymbol{E}\right)\boldsymbol{q} = 0\,, \tag{2.7}$$

with $\boldsymbol{A}$, $\boldsymbol{B}$, $\boldsymbol{C}$, $\boldsymbol{D}$, $\boldsymbol{E}$ being the structural inertia, aerodynamic damping, aerodynamic stiffness, structural damping and structural stiffness matrices, while q are the generalised coordinates, usually in modal coordinates. Here, the aerodynamic matrices $\boldsymbol{B}$ and $\boldsymbol{C}$ are dependent on the reduced frequency and thus have to be recalculated for each reduced frequency. In order to determine the stability of the aeroelastic system

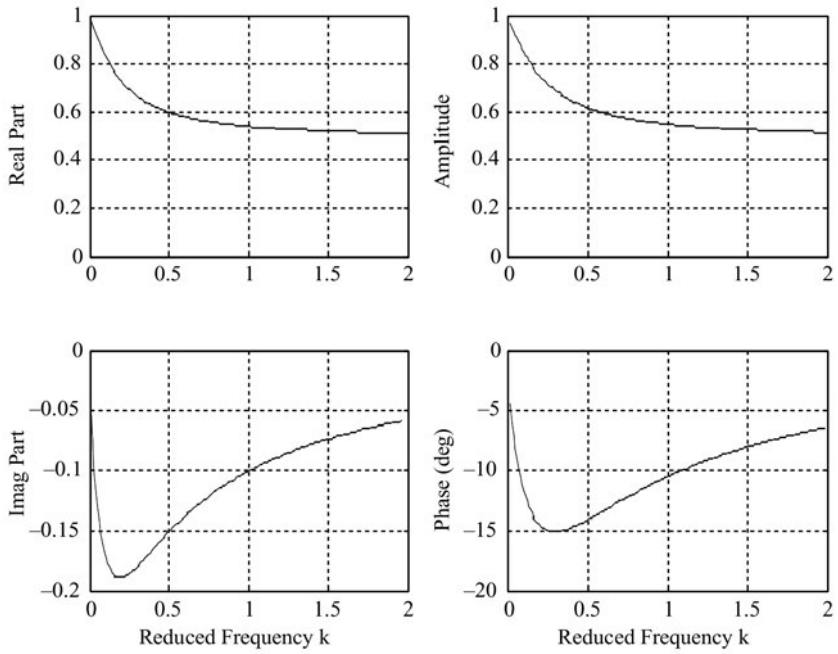

Figure 2.5: Graphic representation of Theodorsen's function [13]

or the system frequencies and damping ratios respectively, an eigenvalue analysis is applied on Eq. (2.7). Since this is an oscillatory system, the eigenvalues λ appear in conjugate complex pairs of the form

$$\lambda_j = -\zeta_j \omega_j \pm i\omega_j \sqrt{1-(\zeta_j)^2}\ ; \quad j = 1, 2, ..., N\ . \tag{2.8}$$

In this case, ω_j represent the system's natural frequencies and ζ_j represent the damping ratios for N degrees of freedom. A positive real part of the eigenvalues means that the system becomes unstable, while the system remains stable as long as all real parts of the eigenvalues are negative. The mode shapes in terms of generalised coordinates can be extracted from the corresponding eigenvectors, which also occur in conjugate complex form and therefore represent complex modes. Finally, the determination of the aeroelastic stability of a system is done by solving the eigenvalue problem of the flutter equation for a range of different air speeds or altitudes, followed by the calculation of the corresponding frequencies and damping ratios. These are then plotted in frequency and damping trends or so-called V-ω and V-g plots, shown in Fig. 2.6, and the flutter speed is determined either by eye, by trial and error from the air speed at which zero damping ratio occurs or by interpolation [13].

One drawback of the illustrated method is that it does not account for the aerodynamic stiffness and damping matrices being dependent on the reduced frequency,

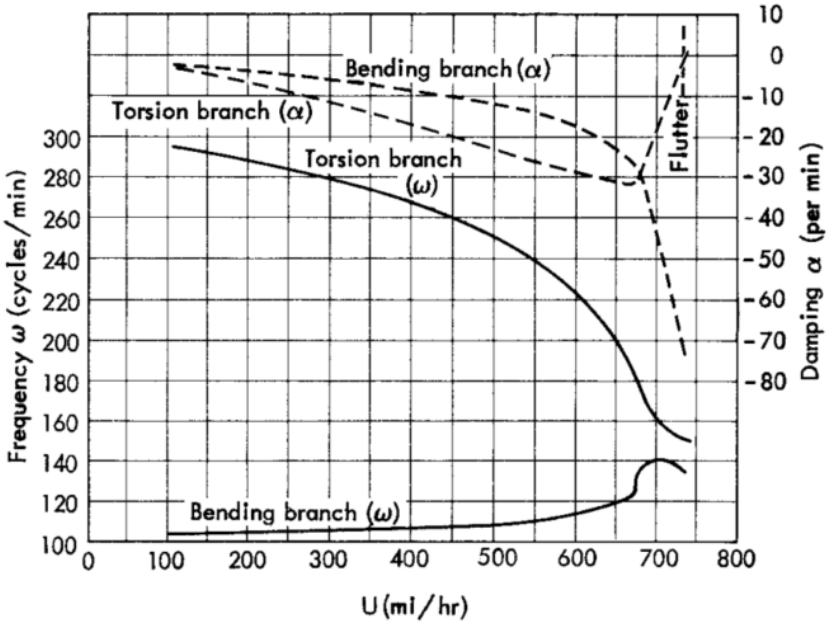

Figure 2.6: Frequency and damping trend for the bending and torsion mode of an aircraft wing [12]

as mentioned earlier in this section. Considering this dependence, the eigenvalue problem of Eq. (2.7) cannot be solved any more, since the relevant $\boldsymbol{B}$ and $\boldsymbol{C}$ matrices cannot be formed unless the reduced frequency is known, which in turn is a result of the solved eigenvalue problem. Therefore, a frequency-matching approach has to be used, with the two commonly used methods briefly described here. In case of the *k method*, a harmonic solution is introduced into the flutter equation. For each reduced frequency of interest, the corresponding $\boldsymbol{B}$ and $\boldsymbol{C}$ matrices are calculated and the eigenvalue problem is solved to find the complex eigenvalues λ. Then the frequencies and damping ratios are determined and allocated to the corresponding air speed using Eq. (2.6) for the reduced frequency. This sequence is repeated for all relevant reduced frequencies and the frequency and damping ratios are afterwards summarised in V-g and V-ω plots, giving an indication of the aeroelastic stability [13].

The basic assumption of a harmonic motion and the resulting introduction of artificial damping has led to many discussions in the industry. It is known that the frequency and damping ratios produced by the *k* method are inappropriate to describe the system behaviour, if the damping ratio is not equal or close to zero [15]. Therefore, another frequency matching approach, called the *p-k method*, has been developed. For each air speed and mode of interest, the frequency of the mode is estimated at first and the corresponding reduced frequency is calculated. The matrices $\boldsymbol{B}$ and $\boldsymbol{C}$ are determined afterwards, followed by the calculation of the frequencies using the

solution of the eigenvalue problem. Taking the frequency solution closest to the initial guess and using it as a new estimate, this sequence is repeated until the frequency converges. With the damping ratio obtained from the converged solution, this is done for all modes and air speeds of interest. After finishing this process, the V-g and V-ω trends can be plotted for the correct reduced frequencies and the flutter speed may be found where the damping is zero. While both the *k* and the *p-k* method provide the same results regarding the flutter speed, it comes to differences in the subcritical behaviour below the flutter speed [13].

Unfortunately, all methods presented for flutter estimation are tied to the assumption of an undeformed or minor deformed wing and are thus not suitable for highly flexible wings. On the one hand, a significant change of the wing geometry due to large deformations clearly leads to a change of both the magnitude or distribution (cf. Fig. 2.2) and the direction of aerodynamic forces (follower force problem). On the other hand, geometrically nonlinear displacements have a considerable impact on the structural properties, e.g. the natural frequencies and the mode shapes of the wing. As these aspects also cause a change of the dynamic behaviour, their consideration is crucial for the correct determination of the stability of the aeroelastic system. Hence, over the last years there have been several studies to modify existing methods or to develop new approaches for the aeroelastic stability analysis of wings with large deformations, which also account for geometrical as well as structural nonlinearities. A short overview on the most recent works will be given at the beginning of Section 3.2. The *p-k* method, however, is used in Section 4.2.5 as part of the Nastran SOL145 aeroelastic analysis for validation of the proposed method.

2.2 The Vortex Lattice Method

As already mentioned before, the aeroelastic solver used for this thesis combines a vortex lattice method (VLM) with a nonlinear finite element (FE) solver. The principles of VLM theory are presented in this section while the basics of nonlinear FE methods will be covered in Section 2.3.1. Although a variety of different aerodynamic methods exists, there are several reasons for the usage of a VLM in an aeroelastic toolbox [16]:

- It is computationally less expensive and faster than other solutions such as Euler or CFD codes, which typically require high mesh resolutions.

- The method represents a medium-fidelity tool that incorporates 3D effects and interferences between wakes and lifting surfaces, that are neglected in 2D strip theory.
- The results are insensitive to large deformations in contrast to the doublet lattice method (DLM), which is a linear method restricted to small out-of-plane displacements.

Due to the long and successful history of the vortex lattice method, a wide range of literature is available. The principles drawn upon in this thesis are mainly based on the comprehensive work of Katz and Plotkin [17]. Since the formulation of the stability analysis in Section 3.2 is based on the unsteady VLM, this will be addressed first. The conversion of the unsteady formulation for the particular case of steady flows is described afterwards.

Considering the flow conditions of the investigated wing, several assumptions can be introduced to simplify the fluid dynamic conservation laws. The flow field is characterised by low air speeds with Mach numbers below 0.3, thus it is regarded as incompressible. Furthermore, high Reynolds numbers are expected so that the viscosity only has a minor influence and can therefore be neglected. This also excludes the effect of boundary layers and the flow field is seen to be irrotational. Supposing an incompressible fluid, the continuity equation can be reduced to

$$\nabla \cdot \boldsymbol{u} = \frac{\partial u}{\partial x} + \frac{\partial v}{\partial y} + \frac{\partial w}{\partial z} = 0 \,, \tag{2.9}$$

where $\boldsymbol{u}$ is the flow velocity vector with its components u, v and w along the Cartesian axes x, y and z. If an irrotational and inviscid flow is assumed, the vorticity is set to zero. Under these conditions it is then possible to obtain the velocity at each point of a flow field by the gradient of the so-called velocity potential ϕ:

$$\boldsymbol{u} = \nabla\phi = \frac{\partial \phi}{\partial x} + \frac{\partial \phi}{\partial y} + \frac{\partial \phi}{\partial z} \,. \tag{2.10}$$

This equation can be combined with the continuity equation Eq. (2.9) and the velocity potential is found by the linear differential equation

$$\nabla \cdot \boldsymbol{u} = \nabla \cdot \nabla\phi = \nabla^2\phi = 0 \,, \tag{2.11}$$

which is also known as *Laplace's equation*. This elliptic differential equation can be used to calculate the velocity field of an inviscid, incompressible and irrotational flow. Although it is not necessary to apply a no-slip boundary condition on a solid-

fluid boundary due to the neglect of viscosity, the solution of Eq. (2.11) leads to a boundary problem. In case of aerodynamic problems the boundary conditions have to be defined on all solid surfaces and at infinity. For solid walls the boundary condition is specified so that there is no normal flow through the solid surface on the boundary. The second boundary condition states that the disturbances due to a body moving through a fluid at rest vanish at infinity. When the flow determined is exterior to the body and a space-fixed reference frame is used, these boundary conditions represent the *Neumann* exterior problem which is

$$\frac{\partial \phi}{\partial n} = \boldsymbol{n} \cdot \boldsymbol{u_B} \qquad \text{on body,} \tag{2.12a}$$

$$\nabla \phi \to 0 \qquad \text{at infinity.} \tag{2.12b}$$

Here, $\frac{\partial \phi}{\partial n}$ denotes the normal derivative of the velocity potential, $\boldsymbol{n}$ the surface normal vector and $\boldsymbol{u_B}$ the velocity on the surface. Since the velocity field itself cannot be used directly for the calculation of aerodynamic forces and moments, the pressure distribution has to be obtained from the velocity field first. A general solution for Laplace's Equation can be derived applying one of Green's identities. This implicates that the solution of Eq. (2.11) is possible by using a distribution of elementary solutions, e.g. sources or doublets, on the boundaries of the problem. While this elementary solutions fulfil the boundary condition Eq. (2.12b) of decaying disturbances at infinity, the velocity becomes singular at the location of the elements themselves. For the problem solution it is then only necessary to find a distribution of the so-called singularity elements, which fulfils the (zero) normal flow condition in Eq. (2.12a). Thereby the specific form of Laplace's Equation allows both the use of one singularity element and a linear combination of two different singularity types. With the flow field being discretised by singularity elements influencing each other, the problem finally reduces to a set of algebraic equations [10]:

$$\boldsymbol{AIC} \cdot \boldsymbol{\Gamma} = \boldsymbol{RHS} \; . \tag{2.13}$$

The normal component of the velocity induced by each element at certain control points, called collocation points, is expressed by the *aerodynamic influence coefficients* matrix $\boldsymbol{AIC}$. On the other hand, the boundary conditions, namely the zero normal flow condition and the Kutta condition are enforced in the right hand side $\boldsymbol{RHS}$, where the Kutta condition states: "The flow leaves the sharp trailing edge of an airfoil smoothly and the velocity there is finite" [17]. Thus Eq. (2.13) can be interpreted to mean that the normal flow through the solid surface has to be cancelled by the velocities induced due to the chosen singularity elements. The equation solved for the circulation $\boldsymbol{\Gamma}$ of each element, which can then be used to calculate pressures,

aerodynamic loads and velocity components respectively.

Besides the source and doublet elements, the velocity potential can also be formulated for a point vortex with a tangential velocity component only and a decay behaviour similar to that of two-dimensional source elements. This foundation is used in the case of the vortex lattice method, where the singularity elements are horseshoe vortices or vortex rings. Since the aerodynamic solver described later in Section 3.1.1 uses the vortex ring formulation, the following explanations will focus on this particular method. Therefore, a thin wing planform with infinitesimal thickness and a free wake is assumed, divided into N quadrilateral surface panels and N_w additional wake panels containing rectilinear vortex rings, as shown in Fig. 2.7. Each vortex ring consists of a closed vortex line, with the leading segment located on the panel's quarter chord line and the collocation point at the centre of the three-quarter chord line. While the location of the leading segment at the quarter chord line is due to satisfy the two-dimensional Kutta condition, the panel normal vector is defined at the collocation point. The circulation Γ of the vortex segments is used to model the lift of each panel and is defined positive according to the right-hand rotation convention.

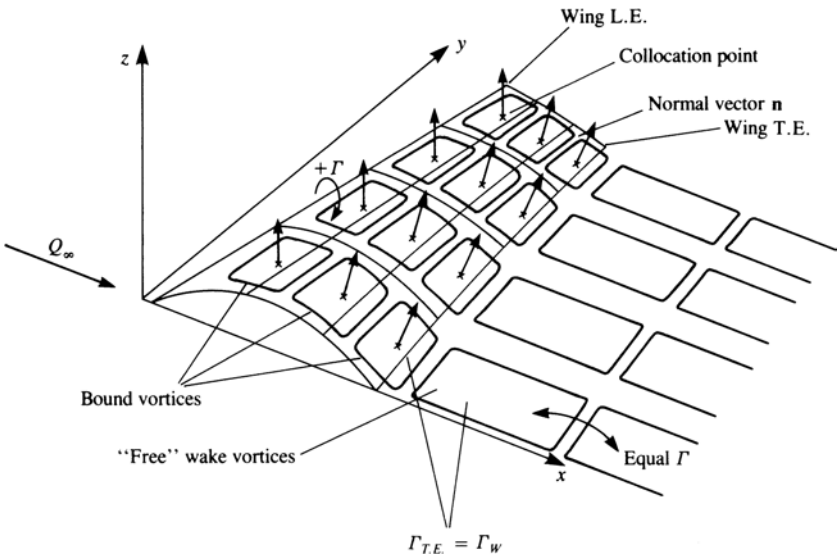

Figure 2.7: Lifting surface and (steady) wake discretised by vortex rings [17]

When the discretisation of the flow domain and the grid generation is finished, the zero normal flow condition is enforced. The normal component of the velocity contains the self-induced velocity, the kinematic or rigid body velocity and the wake-induced velocity. While the latter two are known and can therefore be moved to the right-hand side of Eq. (2.13), the former can be expressed by a combination of influence coefficients. In general, the calculation of this influence coefficients is based on the

Biot-Savart law for the velocity induced at a point *P* by a straight vortex segment, which is found by

$$\Delta u = \frac{\Gamma}{4\pi} \frac{d\boldsymbol{l} \times \boldsymbol{r}}{r^3} \,, \tag{2.14}$$

where $d\boldsymbol{l}$ denotes the direction of the segment and $\boldsymbol{r}$ is the distance between the vortex segment and point *P*. As the Circulation Γ is still unknown at this point of the solution progress, a uniform strength vortex with circulation $\Gamma = 1.0$ is used for evaluating the induced velocities. The influence coefficients a_{ij} represent the normal component of these velocities and can then be determined using the relation

$$a_{ij} = \boldsymbol{u_{ij}}(\Gamma_j = 1) \cdot \boldsymbol{n_i} \,, \tag{2.15}$$

with $\boldsymbol{u_{ij}}$ being the velocity induced at collocation point *i* by a unit vortex at point *j*, and $\boldsymbol{n_i}$ being the panel normal vector at the collocation point. The right hand side $\boldsymbol{RHS}$ of the equation is established by enforcement of the zero normal flow boundary condition on the surface body and contains all kinematic velocity components of the wing. This includes the rigid body motion of the wing and the velocities induced by the wake vortices, as well as any velocity due to an elastic deformation of the wing or encountered gusts:

$$RHS_i = -\left(\boldsymbol{V}_{rb,i} + \boldsymbol{V}_{wake,i} + \boldsymbol{V}_{gust,i} + \boldsymbol{V}_{elastic,i}\right) \cdot \boldsymbol{n}_i \,. \tag{2.16}$$

With both the aerodynamic influence coefficients and the boundary conditions summarised in the AIC matrix and the RHS vector respectively, Eq. (2.13) can be rewritten as a set of algebraic equations:

$$\begin{pmatrix} a_{11} & a_{12} & \dots & a_{1m} \\ a_{21} & a_{22} & \dots & a_{2m} \\ \vdots & \vdots & \ddots & \vdots \\ a_{m1} & a_{m2} & \dots & a_{mm} \end{pmatrix} \begin{pmatrix} \Gamma_1 \\ \Gamma_2 \\ \vdots \\ \Gamma_m \end{pmatrix} = \begin{pmatrix} RHS_1 \\ RHS_2 \\ \vdots \\ RHS_m \end{pmatrix} \,. \tag{2.17}$$

Here, the shape of the AIC matrix is $m \times m$, which will become important in the derivation of the linearisation. This equation is solved for the unknown circulation Γ_i of each panel, which in turn can be used to determine the local pressure distribution and loads. The calculation of aerodynamic forces will be presented in Section 3.1.1, as this is part of the specific implementation of the aerodynamic solver used.

In order to describe an unsteady flow field, the solution process presented has

to be embedded into a time stepping loop with time step size Δt. Beginning with the first time step only the lifting surface is discretised and there are no free wake elements. During the second time step the wing travelled some distance and a wake panel with a vortex strength equal to its circulation in the previous time step is shed by the trailing edge vortex panel, as shown in Fig. 2.8. This procedure is repeated

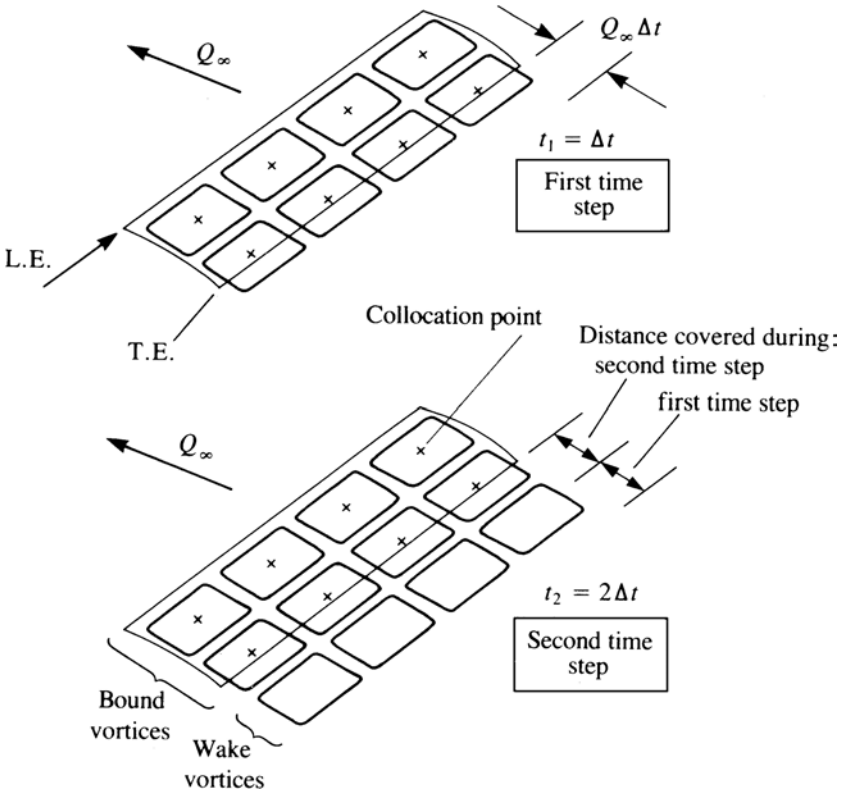

Figure 2.8: Wake shedding procedure for unsteady lifting surface discretised by vortex rings [17]

at each time step, generating a new row of wake vortex rings with the length of the wake vortex ring being dependent on the velocity of the wing and the time step size. The strength of the wake vortex rings remains unchanged once they have been shed. Hence, this model inherently fulfils the *Kelvin theorem*, according to which the total circulation surrounding both the wing and the wake remains unchanged:

$$\frac{D\Gamma}{Dt} = \frac{1}{\Delta t} \left(\Gamma_{airfoil} + \Gamma_{wake} \right) = 0 \, . \tag{2.18}$$

In summary, for each time step the calculations explained above are performed, starting with the determination of the AIC matrix. Once all steps are done and the wake has been shed, the solution sequence is repeated for the next time step. However, as long

as the wing is not deformed, the AIC matrix evaluated during the first time step remains valid for all following time steps. Thus, its calculation only needs to be performed once and can be neglected in the further process in order to save computational costs. A detailed illustration of an unsteady solution sequence is included in Section 3.1.1.

In case of a steady flow field being examined, the time loop and wake shedding procedure are obsolete and the strength of all wake vortex panels is equal to the shedding trailing edge panel (see Fig. 2.7). The wake vortices can therefore be seen as horseshoe-like vortices with side vortex lines parallel to the free-stream, since the spanwise vortex lines cancel each other. Using the *Kutta-Joukowski theorem*, the lift of each bound vortex ring can be found by

$$\Delta L_{i,j} = \rho V_\infty \left(\Gamma_{i,j} - \Gamma_{i-1,j}\right) \Delta y_{i,j} \ , \tag{2.19}$$

where V_∞ denotes the free-stream velocity, $\Gamma_{i-1,j}$ denotes the circulation of the adjacent upstream vortex segment and $\Delta y_{i,j}$ is the panel bound vortex projection normal to the free-stream. The indices *i* and *j* are the chordwise and spanwise counters of the panels respectively.

2.3 Structural Dynamics

So far only a general introduction to aircraft aeroelasticity has been given and aerodynamic modelling using the vortex lattice method has been addressed. The principles of structural dynamics are therefore presented in the following. Since this thesis deals with the nonlinear aeroelastic analysis of a highly flexible wing, the focus will be on nonlinear finite element methods at first. Besides an overview on different types of nonlinearities, the fundamentals of nonlinear static analysis are described. In addition, the specific case of a modal analysis on a preloaded structure with large deformations will be discussed. The section is then concluded with a detailed description of the modal approach in structural-dynamic equations, which will be used for the proposed method of stability analysis in Section 3.2.

2.3.1 Nonlinear Finite Element Methods

Since its development in the mid 1950s finite element procedures have become a standard tool in engineering analysis. Accordingly, today a large number of software

solutions is available for almost every type of problem, however this section concentrates on the basics of static structural analysis. In case of a linear analysis of a structural problem, the finite element formulation is based on several assumptions. The displacements and strains of the structure are considered to be very small and the material as linearly elastic. Furthermore it is assumed that the boundary conditions do not change when forces are applied to the finite element assemblage. The finite element equilibrium equations then result in

$$\boldsymbol{K}\boldsymbol{u} = \boldsymbol{f} \ , \tag{2.20}$$

where the displacement vector $\boldsymbol{u}$ is defined as a linear function of the applied load vector $\boldsymbol{f}$ [18]. Assuming a linear elastic material the stiffness remains constant and the stiffness matrix $\boldsymbol{K}$ is independent from both displacements and loads. The linearity of this equation indicates that an increase of loads results in a proportional increase not only of displacements, but also of stresses and strains. Once the stiffness matrix is determined, the structural response to many different load-cases can be evaluated, making this method a simple and very cost effective-way of analysis [19].

However, it is obvious that the simplifications made for linear analysis, e.g. small displacements, no longer apply when flexible structures undergoing large deformations are concerned. Additionally, in many cases the deflections and strains cannot be related linearly to the loads. Therefore it is necessary to perform a nonlinear analysis which accounts for these effects. The stiffness can then not be considered constant any more, but changes due to the deflection of the structure. This leads to a change of the structural response, which in turn affects the stiffness. In order to solve this problem, nonlinear analysis methods are based on incremental solution schemes, where the calculation is divided into steps with increasing load factor and the stiffness matrix is updated after each step. A very generic example for the differences between linear and nonlinear analysis is shown in Fig. 2.9. Here, a follower tip force emulating the resultant of non-conservative aerodynamic forces is applied to a cantilever beam with 1 m span. The deformation of the beam due to different load factors is determined using a linear and a nonlinear FE method. As can be seen, the two methods lead to significant differences regarding the displacements in the y and z direction, especially at high load factors. While the length of the beam remains constant with the nonlinear approach and a displacement in z is related to a displacement in the y direction, there are no horizontal displacements of the beam nodes in the linear approach. This can be attributed to the usual assumption of small deformations in linear analyses and results in an artificial extension of the beam with increasing tip load. In case of the beam representing an aircraft wing, this would lead to an increase of the wing area and in

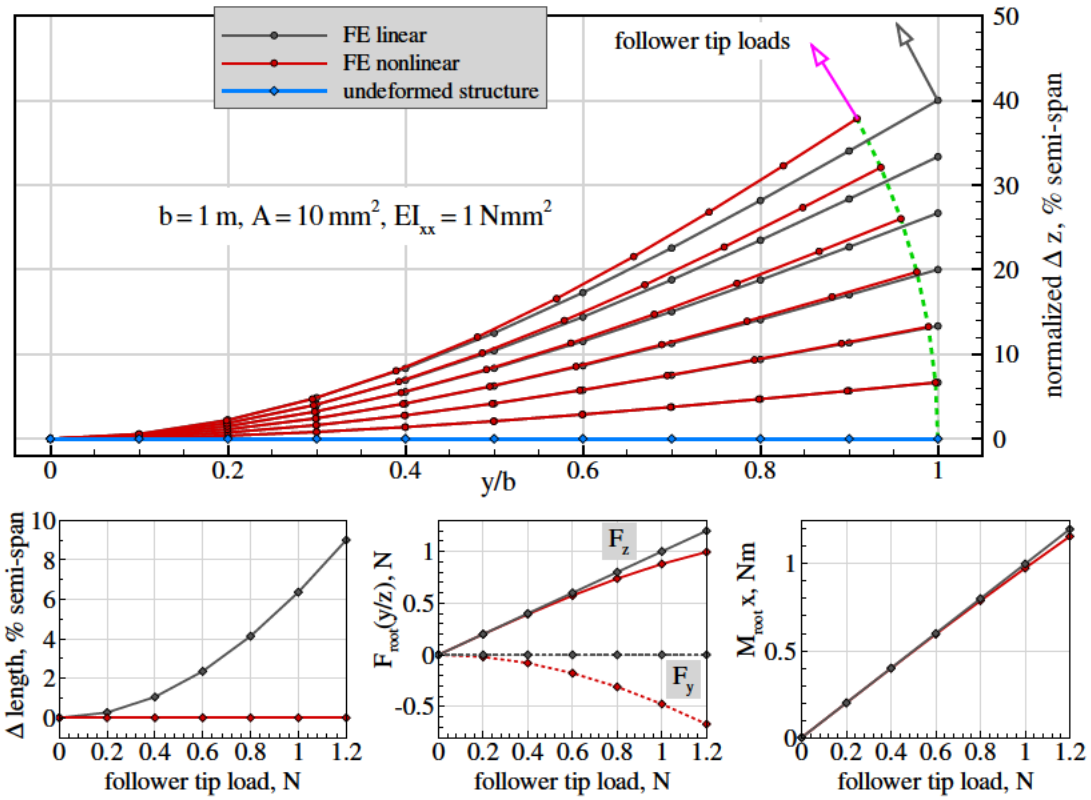

Figure 2.9: Linear and nonlinear FE simulation for a generic beam with tip loading [8]

turn to a change in aerodynamic loads. Besides that, increasing tip loads also result in diverging shear forces in the y and z direction. The root bending moment, however, does not seem to be strongly influenced by the choice of a linear or a nonlinear solution. Regarding the nonlinear solution, the moment increases with increasing tip load, since the applied force is rotated due to the displacements. On the other hand, in the linear case the applied force is not rotated and only acts in the z direction, thus the increased bending moment is caused by the greater length of the beam. Nevertheless, application of a nonlinear method is mandatory for the purpose of this thesis, since the two solutions result in different distributions and locations of masses [8]. In addition, this will lead to a change of modal properties of the preloaded structure, which in turn influences the dynamic stability of the system.

The general formulation of a nonlinear analysis describes a state of equilibrium between external and internal forces and moments with regard to the deformed geometry. In case of a static analysis the solution is time independent and the equilibrium condition is defined by [18]

$$\boldsymbol{f}^{(n)} - \boldsymbol{r}^{(n)} = \boldsymbol{0}\,, \tag{2.21}$$

where $\boldsymbol{f}$ represents the externally applied nodal point forces at the incremental load step n and $\boldsymbol{r}$ represents the internal nodal point forces corresponding to the finite element stresses. This equation must be fulfilled for the current deformed geometry as well as for the next state. Considering an incremental load step $n+1$ the equilibrium is defined as

$$\boldsymbol{f}^{(n+1)} - \boldsymbol{r}^{(n+1)} = \boldsymbol{0} \; . \tag{2.22}$$

When the solution at load step n is already known and the applied forces $\boldsymbol{f}^{(n+1)}$ are assumed to be independent of the deformations, the internal forces can be expressed using

$$\boldsymbol{r}^{(n+1)} = \boldsymbol{r}^{(n)} + \Delta\boldsymbol{r} \; . \tag{2.23}$$

Here, $\Delta\boldsymbol{r}$ denotes the increment in nodal forces due to the increase of element displacements and stresses between load step n and $n+1$. The internal force increment can be determined using the linear relation

$$\Delta\boldsymbol{r} = \boldsymbol{K}^{(n)}\Delta\boldsymbol{u} \; , \tag{2.24}$$

with $\Delta\boldsymbol{u}$ being the vector of incremental nodal displacements. The tangent stiffness matrix $\boldsymbol{K}^{(n)}$, which is related to the current geometric and material characteristics at load step n, is found as

$$\boldsymbol{K}^{(n)} = \frac{\partial^{(n)}\boldsymbol{r}}{\partial^{(n)}\boldsymbol{u}} \; . \tag{2.25}$$

Introducing these equations into Eq. (2.22) yields the following linear relation:

$$\boldsymbol{K}^{(n)}\Delta\boldsymbol{u} = \boldsymbol{f}^{(n+1)} - \boldsymbol{r}^{(n)} \; . \tag{2.26}$$

This equation is solved for $\Delta\boldsymbol{u}$ and the exact displacements at load step $n+1$ corresponding to the applied loads $\boldsymbol{f}^{(n+1)}$ can then be obtained by

$$\boldsymbol{u}^{(n+1)} = \boldsymbol{u}^{(n)} + \Delta\boldsymbol{u} \; . \tag{2.27}$$

It is important to note that Eq. (2.24) only represents an approximation for the increment in nodal forces due to element stresses. Depending on the load step size the results may be very different from the actual solution or even be unstable if the sequence presented above is only performed once per load step. Therefore the introduction of an iterative solution process is necessary, usually based on the Newton-Raphson method. In this case the total displacements $\boldsymbol{u}^{(n+1)}$ calculated are used for

another solution of the same load step n. The above equations become

$$\boldsymbol{K}_{(i-1)}^{(n+1)} \Delta \boldsymbol{u}_{(i)} = \boldsymbol{f}^{(n+1)} - \boldsymbol{r}_{(i-1)}^{(n+1)}, \tag{2.28a}$$

$$\boldsymbol{u}_{(i)}^{(n+1)} = \boldsymbol{u}_{(i-1)}^{(n+1)} + \Delta \boldsymbol{u}_{(i)} \ , \tag{2.28b}$$

where $i = 1, 2, 3, ...$ denotes the iteration loop and the initial conditions are

$$\boldsymbol{u}_{(0)}^{(n+1)} = \boldsymbol{u}^{(n)}; \qquad \boldsymbol{K}_{(0)}^{(n+1)} = \boldsymbol{K}^{(n)}; \qquad \boldsymbol{r}_{(0)}^{(n+1)} = \boldsymbol{r}^{(n)} \ . \tag{2.29}$$

For the initial iteration loop $i = 1$ the right hand side of Eq. (2.28a) is not in balance due to the internal forces caused by element stresses. This results in an increase and update of the nodal displacements, which is repeated until the increment in displacements is small and a predefined convergence criterion is satisfied [18].

Another important point of nonlinear analysis is the calculation of the tangent stiffness matrix $\boldsymbol{K}_{(i-1)}^{(n+1)}$. A proper and regularly updated tangent stiffness matrix is crucial for fast convergence and few iteration loops, but its evaluation is also a computational costly process. Stiffness update strategies usually are variations of the modified Newton's method, where the tangent stiffness matrix is only updated at the beginning of each load step, for example in the Newton-Raphson method. However, a detailed description of the different methods available is beyond the scope of this thesis and can be found in references [18] and [19].

In general, the typical formulation used for nonlinear analysis depends on the nonlinear effects involved, with three different sources being identified [19]:

- **Material Nonlinearities** describe a nonlinear relation between stresses and strains, e.g. metal plasticity, where large strain can influence the material behaviour.
- **Geometric Nonlinearities** include large displacements and are caused by nonlinear relations between strains and displacements, as well as between stresses and forces.
- **Nonlinear Boundary Conditions**, where either the forces vary due to the structure's displacement, which is called follower force problem, or the boundary conditions change due to motion and contact to another structural component.

For the investigation of a highly flexible wing, as it is subject of this thesis, especially the latter two are of great interest. Regarding large deformations there are two distinct types of problems. In case of large displacements and small strains, the nonlinearities in the stress-strain law can be neglected and only the nonlinear

relations between strain and displacements are taken into account. When it comes to large displacements and large strains, the stress-strain relation is also considered nonlinear. Furthermore, in terms of geometric nonlinearities two different approaches are usually defined to describe the kinematics of deformation. Both are based on the Lagrangian method, where the finite element mesh is fixed to the material and moves with it through space. While the *total Lagrangian approach* uses the original undeformed state as a reference for the equilibrium formulation, the *updated Lagrangian approach* uses the configuration of the previous load step. The former is mainly used for nonlinear elastic problems and creep or plasticity problems with large rotations and small strains. The latter is suitable for analyses involving plasticity and large strains as well as contact problems [19].

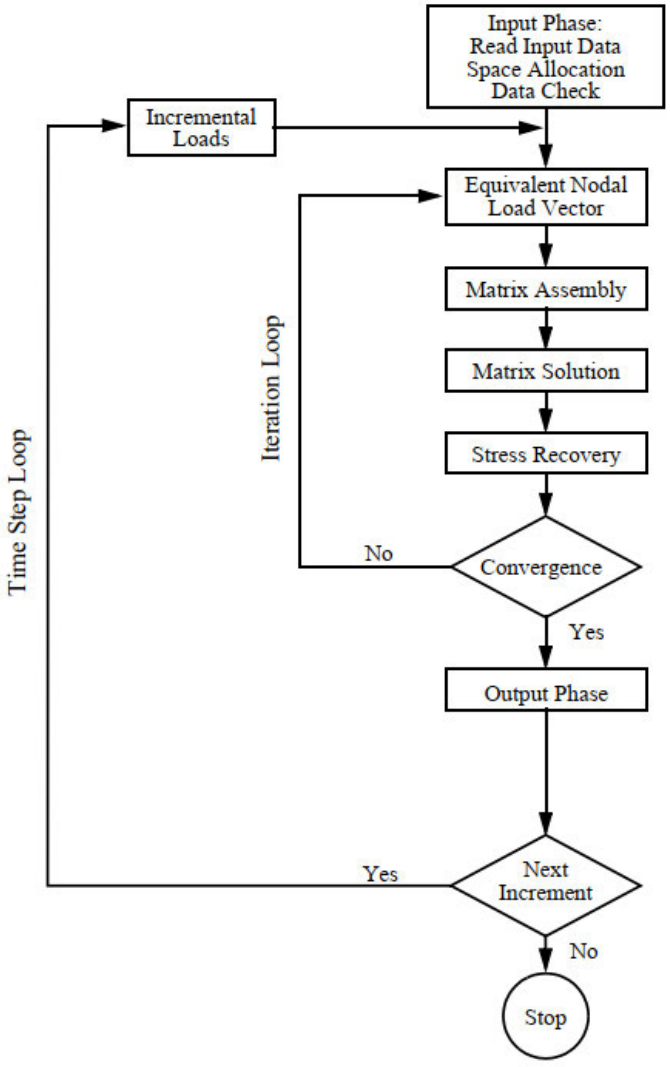

Figure 2.10: Nastran nonlinear SOL400 flow chart [19]

As it has been already mentioned, the aeroelastic solver used couples a VLM with the commercial FE solver MSC Nastran. The FE simulations are performed using the nonlinear solution sequence SOL400. Therefore the nonlinear solution parameters are set in the bulk data entry of the Nastran input file. Besides the required input of the number of load increments, it is also possible to define the method for controlling stiffness updates, the maximum number of iterations per load increment, as well as different convergence criteria or error tolerances. Additionally, the bulk data entry also contains the geometric nonlinearity formulation. In MSC Nastran both the total and updated Lagrangian method are available and can be selected by the user. If no selection is made, Nastran will choose the most sufficient method based on the finite element model and the type of analysis. Once the simulation is started, the solution sequence proceeds corresponding to the flow diagram shown in Fig. 2.10. The total load is increased in small steps and for each incremental load step the nodal load vector and tangent stiffness matrix are determined. Afterwards the element stresses due to the new displacements are calculated and the solution is checked for convergence. The iteration procedure is repeated with the updated total displacement vector as long as the convergence criterion is not satisfied. When convergence is achieved, the next load increment is applied until the model is solved for the full load. A short description of the nonlinear solution parameters used for the simulations of the Pazy wing is included in Section 4.2.1.

2.3.2 Normal Modes Analysis

The nonlinear static analysis described in the previous section is important for determining the static aeroelastic equilibrium in Section 4.2.2. Another very essential part of the FE simulations performed is the identification of the modal properties of the system, since these are needed as an input for the proposed method for stability analysis. Therefore the natural frequencies and mode shapes are extracted by using an eigenvalue analysis. In general, the natural frequencies describe the frequencies at which the structure naturally tends to vibrate. Each natural frequency is associated with a corresponding mode shape, called normal mode of vibration, which describes the deformed shape of a structure when it oscillates at the associated natural frequency. It should be noted that the natural frequencies and modes are dependent on the structural properties and boundary conditions. Considering a change in structural properties, the natural frequencies change while the mode shapes remain unaltered. In contrast, a change of the boundary conditions leads to a modification of both the frequencies and mode shapes. As it has already been pointed out, the structural

properties change when the system is undergoing large deformations. Hence, for the analysis of very flexible wings it is necessary to determine the normal modes and frequencies in respect to the deformed rather than the undeformed state. The eigenvalues to be determined are defined by the solution of the undamped linear dynamics problem [19]

$$(\boldsymbol{K} - \omega_i^2 \boldsymbol{M})\boldsymbol{\Phi}_i = 0 \; ; \quad (i = 1, \ldots, n) \; , \tag{2.30}$$

where $\boldsymbol{K}$ is the stiffness matrix, $\boldsymbol{M}$ is the mass matrix, ω_i represents the i'th natural frequency (square root of eigenvalue), $\boldsymbol{\Phi}_i$ the corresponding eigenvector and n is the number of eigenvalues. For a modal analysis of a preloaded structure, the latest updated tangent stiffness matrix is used instead of the initial stiffness matrix. In MSC Nastran this specific type of normal modes extraction is included in SOL400 and is performed after a static analysis. Here, a number of different methods is available for the solution of the eigenvalue problem, with the *Lanczos algorithm* probably being the most commonly used. The selection of the desired method, the number of modes to be determined and the frequency range of interest, as well as other settings for the modal analysis is made in the bulk data entry of the Nastran input file [19]. Similar to the static analysis, the setup of the modal analysis for the Pazy wing test case is included in Section 4.2.3.

2.3.3 Modal Approach in Generalised Coordinates

The structural analysis methods presented so far cannot be used directly for the stability analysis of a highly flexible wing. The nonlinear static analysis already implemented as part of SOL400 in the aeroelastic solver is used to compute the steady aeroelastic equilibrium points. The results of the normal modes analysis at these preloaded equilibrium states, which is not implemented in the original solver, are taken as an input for the proposed method. While the aerodynamics will later be derived from the vortex lattice method (see Section 2.2), a modal approach in generalised coordinates is used to describe the dynamic response of the system. Therefore this method is explained in the following.

In general, the calculation of dynamic response becomes very computationally intensive as the number of degrees of freedom (DOFs) increases. Furthermore, structures discretised by finite elements can easily contain more than ten-thousand DOFs and can only be solved with considerably computational effort even when using high-performance computers. These difficulties can be avoided by coordinate trans-

formation from physical into generalised coordinates. This leads to a reduction of number of DOFs and decouples the individual equations of motion of the system. Thus the dynamic response of a system with n physical DOFS can be described by a decoupled system of equations with N generalised DOFs, where $N \ll n$. The equation of motion for a multi degrees of freedom system without damping in physical coordinates yields [20]

$$\boldsymbol{M}\ddot{\boldsymbol{x}} + \boldsymbol{K}\boldsymbol{x} = \boldsymbol{f} \ , \tag{2.31}$$

where $\ddot{\boldsymbol{x}}$ and $\boldsymbol{x}$ denote the second time derivative of the displacement vector (acceleration) and the displacement vector respectively, $\boldsymbol{f}$ denotes the force vector, while $\boldsymbol{M}$ and $\boldsymbol{K}$ again represent the mass and stiffness matrix. Using the homogenous equation of motion

$$\boldsymbol{M}\hat{\ddot{\boldsymbol{x}}} + \boldsymbol{K}\hat{\boldsymbol{x}} = 0 \ , \tag{2.32}$$

and applying the approach

$$\hat{x} = \hat{y}\, e^{\lambda t} \ , \tag{2.33}$$

where $\hat{y}$ is a complex amplitude and λ is an arbitrary complex parameter, results in

$$\left[\boldsymbol{\lambda}^2\boldsymbol{M} + \boldsymbol{K}\right] \hat{\boldsymbol{y}}\, e^{\boldsymbol{\lambda} t} = 0 \ . \tag{2.34}$$

Assuming that $e^{\lambda t} \neq 0$ and by neglecting the trivial solution $\hat{y} = 0$, this can be reduced to the characteristic equation

$$|\boldsymbol{\lambda}^2\boldsymbol{M} + \boldsymbol{K}| = 0 \ . \tag{2.35}$$

By solving this relation the eigenvalues $\lambda_i = \pm i\omega_i$ and thus the natural frequencies ω_i $(i = 1, 2, \ldots, n)$ are obtained. The eigenvectors $\hat{\boldsymbol{y}}_i = \boldsymbol{\Phi}_i$ can then be determined by introducing the eigenvalues into Eq. (2.34). For the transformation into generalised coordinates it is assumed that the structural displacements of the system during external excitation can be represented by superposition of the displacements of the different natural modes. This can be expressed by the modal approach

$$\boldsymbol{x}(t) = \boldsymbol{\Phi}\, \boldsymbol{q}(t) = \sum_{i=1}^{n} \boldsymbol{\Phi}_i\, q_i(t) \ . \tag{2.36}$$

The modal matrix $\boldsymbol{\Phi}$ column-wise includes the displacements of the physical degrees of freedom corresponding to the different natural modes. In addition, $\boldsymbol{q}$ is called the generalised coordinates vector, which contains the factors of the linear combination representing the contribution of each mode to the dynamic response of the system. Unfortunately the total number of natural frequencies and modes is equal to the num-

ber of physical DOFs of the system. In the general case of external excitation, however, a sufficient description of the system's dynamic response can also be obtained by superposition of only the lowest frequent modes. As a rough estimate, for the calculation of the dynamic response in the frequency between 0 and f the natural modes in the frequency range between 0 and $2f$ should be considered in the modal approach. Using this approximation, the number of DOFs used for describing the system behaviour can be significantly reduced by using a smaller number of modes N instead of the total number of modes n, where $N \ll n$. Eq. (2.36) can also be applied to the velocity and the acceleration vector, which are found by

$$\dot{\boldsymbol{x}}(t) = \boldsymbol{\Phi}\, \dot{\boldsymbol{q}}(t) \;, \tag{2.37a}$$

$$\ddot{\boldsymbol{x}}(t) = \boldsymbol{\Phi}\, \ddot{\boldsymbol{q}}(t) \;. \tag{2.37b}$$

The introduction of those equations and Eq. (2.36) into the general equation of motion in Eq. (2.31) results in the equation of motion in generalised coordinates:

$$\bar{\boldsymbol{M}}\, \ddot{\boldsymbol{q}} + \bar{\boldsymbol{K}}\, \boldsymbol{q} = \bar{\boldsymbol{f}} \qquad \text{or} \tag{2.38a}$$

$$\sum_{s=1}^{N} \bar{\boldsymbol{M}}_{rs}\, \ddot{q}_s + \sum_{s=1}^{N} \bar{\boldsymbol{K}}_{rs}\, q_s = \bar{f}_r \;; \qquad (r = 1, 2, \ldots, N) \;. \tag{2.38b}$$

Here, $\bar{\boldsymbol{M}}$ and $\bar{\boldsymbol{K}}$ are the generalised mass and stiffness matrices respectively and $\bar{\boldsymbol{f}}$ represents the vector of generalised forces. These are defined by

$$\begin{aligned} \bar{\boldsymbol{M}} &= \boldsymbol{\Phi}^T \boldsymbol{M}\, \boldsymbol{\Phi} \;, \\ \bar{\boldsymbol{K}} &= \boldsymbol{\Phi}^T \boldsymbol{K}\, \boldsymbol{\Phi} \;, \\ \bar{\boldsymbol{f}} &= \boldsymbol{\Phi}^T \boldsymbol{f} \;. \end{aligned} \tag{2.39}$$

If the modal approach is applied using the natural modes of a system, the generalised mass and stiffness matrices exist in diagonal form. This is also the case for the generalised damping matrix $\bar{\boldsymbol{D}}$ if the physical damping matrix is assumed to be a linear combination of the mass and stiffness matrix. The damping is then referred to as *modal* or *Rayleigh* damping

$$\boldsymbol{D} = \alpha \boldsymbol{M} + \beta \boldsymbol{K} \;, \tag{2.40}$$

and the equations of motion of the dynamic system can be represented in a set of N decoupled equations

$$\bar{\boldsymbol{M}}\ddot{\boldsymbol{q}} + \bar{\boldsymbol{D}}\dot{\boldsymbol{q}} + \bar{\boldsymbol{K}}\boldsymbol{q} = \bar{\boldsymbol{f}} \qquad \text{or} \tag{2.41a}$$

$$\bar{\boldsymbol{M}}_{rr}\,\ddot{q}_r + \bar{\boldsymbol{D}}_{rr}\,\dot{q}_r + \bar{\boldsymbol{K}}_{rr}\,q_r = \bar{f}_r\ ; \qquad (r = 1, 2, \ldots, N)\ . \tag{2.41b}$$

The transformation of physical into generalised coordinates consequently leads to a substantial simplification of the system description [20].

2.4 Fluid-structure Interaction

In general, it is possible to develop aeroelastic models by simplification and continuous approximation of the aerodynamic and structural model, similar to the principles shown in Section 2.1. These approaches, however, are not sufficient for modelling complex non-uniform configurations such as real aircraft structures [13]. Thus, more advanced discrete methods for modelling aerodynamics and structural dynamics were presented separately. For the purpose of aeroelastic analyses the aerodynamic and structural models have to be combined in an efficient way to determine static and dynamic aeroelastic behaviour. Therefore a short overview of different approaches for simulating fluid-structure interaction (FSI) is given in this section. Apart from the aeroelastic analysis of flight vehicles, FSI simulations have become increasingly important in the flutter prediction of turbo machinery, in parachute dynamics and especially in medical engineering in recent years. Nowadays, two distinct methods are available for the solution of FSI problems. The *monolithic* approach directly considers the interaction between structure and fluid flow by solving the flow and structural equations simultaneously. Therefore the entire solid and fluid domain is discretised by a global system of nonlinear equations, which can be solved e.g. by Newthon-Raphson iterations. In contrast, the structural and fluid dynamic equations are solved separately in the *partitioned* approach, with the solution in the flow domain remaining unchanged while the structural solution is calculated and vice versa. The use of two distinct solvers enables the application of different and more efficient solution techniques for each domain while preserving software modularity at the same time. On the other hand, this method requires a coupling interface for the data exchange between the different solvers [21]. Furthermore, an approach for the temporal coupling of the disciplines is necessary for unsteady simulations. Although monolithic solvers outperform partitioned solutions in some cases in terms of computational cost and accuracy, the partitioned approach is

still mainly used in aerospace industry [13, 22]. In aeroelastic analyses, structural components are usually modelled using finite elements, whereas numerical panel methods, e.g. vortex or doublet lattice methods, are used for calculating aerodynamic forces. The integration of high-fidelity methods such as computational fluid dynamics (CFD) methods, however, is primarily limited to scientific research due to the high demands on computational capabilities [13].

The aeroelastic solver used for this work is based on the typical industrial (partitioned) approach, coupling a vortex lattice code with a finite element solver. Since both solution methods are applied independently, another methodology is required to transfer the data between the aerodynamic and the structural model. A detailed description of the coupling interface is therefore included in Section 3.1.2.

3 A Linearised Method for Aeroelastic Stability Analysis

Based on the theoretical principles presented in the previous sections this chapter addresses the development of a method for stability analysis for highly flexible wings. The goal is to use the existing solver for steady static coupling simulations and then to linearise the whole aeroelastic system at static equilibrium points with large deformations. Since the proposed method will be implemented into the framework of the aeroelastic solver, a description of this is presented at first. This includes both some important features of the specific vortex lattice implementation as well as aspects of the coupling interface between aerodynamic and structural model. The linearisation itself is explained in Section 3.2 and formulated using a linear state-space model. After a brief introduction to the basics of linear state-space models, the following sections will focus on the derivation of the linearised aerodynamic and structural model, and finally the whole linearised aeroelastic system.

3.1 The Aeroelastic Solver

The aeroelastic solver used was developed by Ritter [8] at the Institute of Aeroelasticity at DLR Goettingen. Its main parts are written in the *Python* programming language, with some parts using *Fortran* for the calculation of the AIC matrix applying the Biot-Savart law. In addition, the code makes use of the *NumPy* and *SciPy* libraries, which provide efficient functions for numerical calculations with large, multidimensional matrices. A number of different types of solvers is available, whereas in this thesis the unsteady aerodynamic solver, the steady aeroelastic solver and the unsteady aeroelastic modal solver are used. Besides, it is also possible to perform trim simulations or flight dynamic aeroelastic simulations of a free-flying aircraft. The simulation setup is defined in an input file, containing all aerodynamic and flight dynamic parameters as well as several settings for the structural solution. The data of

the structural model is provided in a separate file depending on the chosen structural solver.

3.1.1 Basic Aerodynamic Solver

The aerodynamic solver uses a vortex lattice implementation with vortex rings, which has already been discussed in detail in Section 2.2. The calculation of forces, however, was neglected so far and will be covered in the following instead, since this part of the implementation differs from the original vortex lattice method. In this particular case, the calculation of the aerodynamic forces $\boldsymbol{F}_i^A$ is based on the method by Mauermann [23] and yields [8]

$$\boldsymbol{F}_i^A = \boldsymbol{F}_{S,i}^A + \boldsymbol{F}_{U,i}^A \ . \tag{3.1}$$

The steady forces $\boldsymbol{F}_{S,i}^A$ can be calculated by

$$\boldsymbol{F}_{S,i}^A = \rho_\infty \, \Gamma_{eff,i} \, (\boldsymbol{V}_{RB,i} + \boldsymbol{V}_{gust,i} + \boldsymbol{V}_{elastic,i}) \times \boldsymbol{r}_i \ , \tag{3.2}$$

where ρ_∞ is the fluid density and $\boldsymbol{r}_i$ is a vector of length b equal to the quarter chord line of the corresponding aerodynamic panel i. Furthermore, $\Gamma_{eff,i}$ denotes the effective circulation, which is either the difference of the circulation of the corresponding aerodynamic panel and the adjacent panel in chordwise downstream direction. Otherwise it is the circulation of the corresponding panel itself, if the panel is located at the leading edge. The unsteady aerodynamic forces $\boldsymbol{F}_{U,i}^A$ are found as

$$\boldsymbol{F}_{U,i}^A = \rho_\infty \, A_i \frac{\partial \Gamma_i}{\partial t} \boldsymbol{n}_i \ , \tag{3.3}$$

with A_i being the area of the i-th panel, Γ_i the bound circulation and $\boldsymbol{n}_i$ the normal vector. From Eq. (3.2) and Eq. (3.3) it can be observed that the steady forces act perpendicular to the quarter chord line and the direction of the total velocity vector, while the unsteady forces act along the normal vector of the panel. However, both steady and unsteady forces act at the centre of the panel's quarter chord line or the centre of each bound vortex ring respectively. In the original implementation developed by Ritter [8] a second-order backward scheme was used to determine the time derivative of the circulation. Subsequent investigations showed that this method causes an instability of the solution sequence under certain conditions. As a result, an additional first-order backward scheme was implemented and also used for the

simulations in this thesis,

$$\frac{\partial \Gamma_i}{\partial t} \approx \frac{\Gamma_i^n - \Gamma_i^{n-1}}{\Delta t} \ , \tag{3.4}$$

where the superscript n represents the current time step and Δt the time step size.

Besides the calculation of aerodynamic forces, the treatment of the wake shall also be discussed at this point. The time stepping procedure for an unsteady aerodynamic problem has already been described in Section 2.2. Considering the RHS vector as shown in Eq. (2.16), it can be seen that the wake induced velocities are also taken into account, i.e. the bound circulation of the wing is influenced by the wake. Since a new wake row is shed every time step, this becomes computationally demanding with an increasing number of time steps and thus a long wake is part of the solution. According to the Biot-Savart law in Eq. (2.14) the influence of a vortex segment on a point *P* decreases with the square of the distance r between the vortex segment and this point. Hence, it is possible to truncate the wake when a predefined length is reached in order to save computational costs, as the influence of wake rows far behind the wing can be neglected. In addition, the wake can be relaxed which means that it moves with the local induced velocities. This is used to simulate wake roll-up, e.g. for roll-up of wingtip trailing vortices, but is not applied in this thesis to speed up calculations.

As it has been mentioned earlier in this section, the steady aerodynamic forces computed act perpendicular to the sum of all velocity contributions. By means of this, no drag components are included in these forces. Instead the induced drag $\boldsymbol{F}_{D,i}^A$ is calculated separately using the relation [8]

$$\boldsymbol{F}_{D,i}^A = \rho_\infty \, \Gamma_{eff,i} \left(\boldsymbol{V}_{bodystreamwise,i} + \boldsymbol{V}_{wake,i} \right) \times \boldsymbol{r}_i \ . \tag{3.5}$$

Nevertheless, the vortex lattice method does not account for viscous drag forces. In the aerodynamic solver used, this problem is circumvented by approximating the viscous drag forces using the drag polars of the wing's airfoil [8]. For this thesis, however, the calculation of drag forces was neither considered for the simulations of steady aeroelastic equilibrium points nor for the implementation of the method for stability analysis. Finally, the flowchart of the unsteady vortex lattice implementation is shown in Fig. 3.1. Important parameters, such as onflow velocity, angle of attack or time step size, as well as the definition and discretisation of lifting surfaces are included in the input file, called *para* file. The grid generation and the evaluation of the AIC matrix are part of the initialisation process. Afterwards, the RHS vector including all velocities induced at the collocation points is established. The system can then be solved for the circulation Γ_i of each aerodynamic panel, followed by secondary

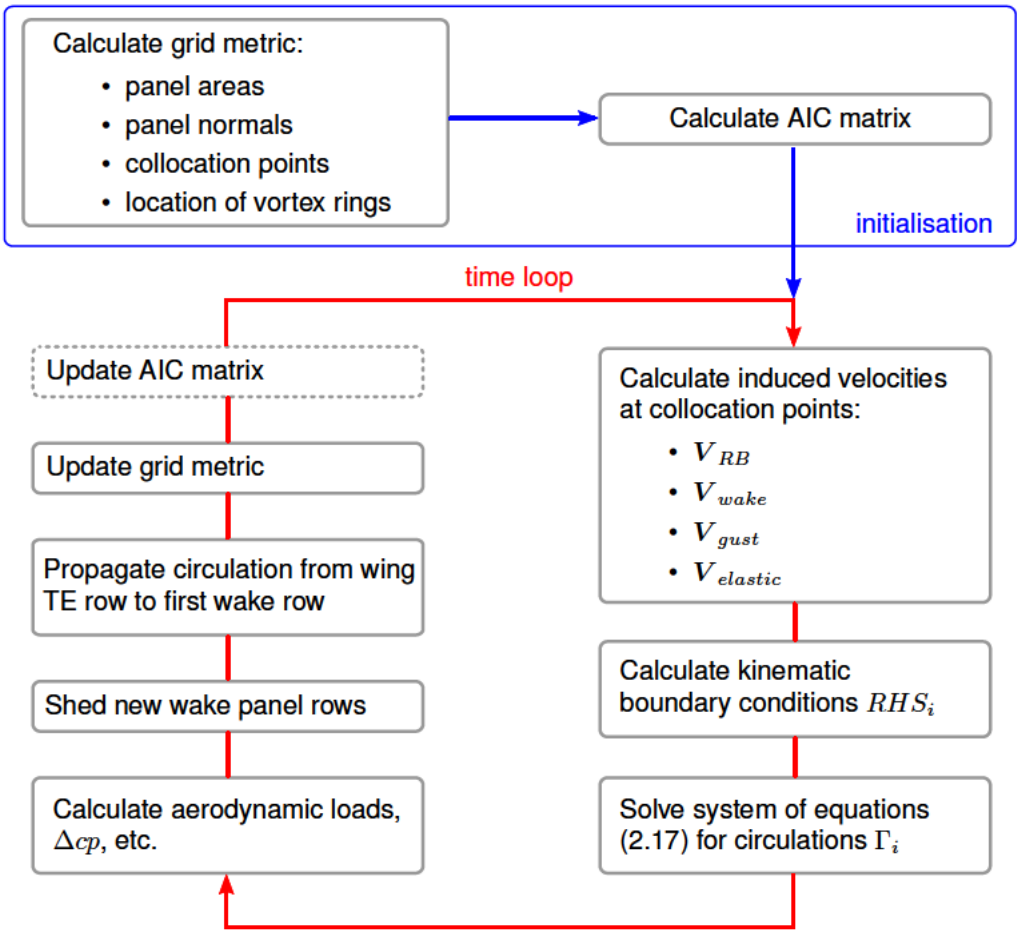

Figure 3.1: Solution sequence of the unsteady vortex lattice method [8]

calculations, e.g. aerodynamic loads or pressure distributions. In preparation for the next time step the wake shedding procedure is performed to move the existing wake panels and to shed a new row of wake panels with the circulation from the trailing edge. In case of aeroelastic coupled simulations, the aerodynamic grid is updated accounting for all translations and rotations due to structural deformation of the wing. The AIC matrix can also be updated to consider changes in geometric relations in the Biot-Savart law caused by high displacements.

3.1.2 Static Coupling Solution Sequence

The aeroelastic simulations used to determine the steady static equilibrium points are performed by applying a so-called *static coupling solver*. Here, the aerodynamic

solution is obtained by the steady vortex lattice implementation, whereas the structural solution is computed separately using the MSC Nastran FE solver. As already discussed in Section 2.4, this partitioned approach requires a coupling interface to exchange data between both solvers. The application of two different solvers also leads to the problem of two different and independent models. In this particular case, the aerodynamic forces $\boldsymbol{F}^A$ are evaluated at the centre of the quarter chord line of each panel within the vortex lattice method. However, the nodes of the structural model are not coincident with the quarter points of the VL grid, but are, in most cases, located at different positions. Thus, the forces can not be applied directly to the structural nodes and have to be transferred at first. This typical problem of fluid-structure interaction can be solved using the following relations [8]:

$$\boldsymbol{u}^A = \boldsymbol{H}\,\boldsymbol{u}^S \qquad \text{and} \tag{3.6a}$$

$$\boldsymbol{F}^S = \boldsymbol{H}^T\,\boldsymbol{F}^A\,. \tag{3.6b}$$

The former describes a linear mapping of the displacements of the structural nodes $\boldsymbol{u}^S$ to obtain the displacements of the aerodynamic grid points $\boldsymbol{u}^A$ using the *coupling matrix* $\boldsymbol{H}$. The latter equation is used to transform the aerodynamic forces $\boldsymbol{F}^A$ into equivalent forces $\boldsymbol{F}^S$ applied to the structural model. For both operations the same coupling matrix can be used either in normal or in transposed form. Nevertheless, it should be noted that, in general, the transformation of loads differs from the transformation of displacements. While displacements can be interpolated e.g. with polynomial or spline interpolation schemes, this would lead to a change in the sum of forces in the case of force interpolation. Instead, the coupling matrix has to account for the global conservation of work as well as the correct description of the structural deformations. The coupling matrix of the aeroelastic solver used is based on two- and three-dimensional *radial basis functions*, which only evaluate the positions of the structural nodes and the aerodynamic grid points. Radial basis functions have become a common tool for multivariate interpolation in fluid-structure interaction, with various functions being available for different applications [24]. In this particular solver, the *thin-plate-spline* basis function for three-dimensional structural models was implemented [8].

The general workflow of the static coupling solution sequence including the steady vortex lattice method and the static structural solution using Nastran is illustrated in Fig. 3.2. In addition to the setup of the aerodynamic model in the solver's para file, the initialisation process also includes the setup of the FE model as a pre-processing step. For the case of a FE simulation with Nastran, this is provided in a separate Nastran *bdf* input file. This file contains the model geometry defined by

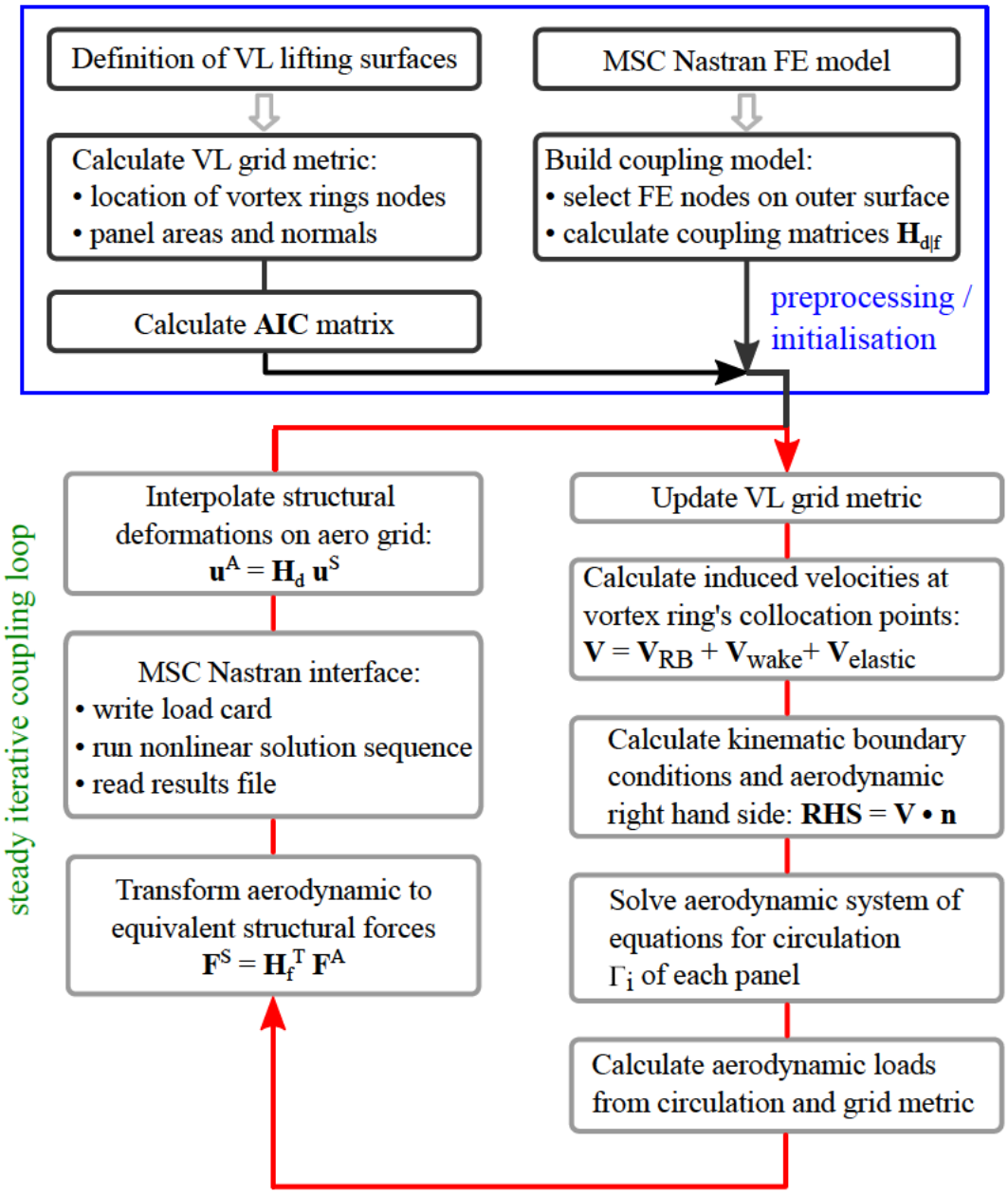

Figure 3.2: Steady iterative coupling solution sequence including Nastran nonlinear static solution [25]

nodes and elements, e.g. beam or shell elements, and the corresponding material and structural properties of those elements. Furthermore, the simulation setup is defined in the bulk data entry at the beginning of the bdf file. Here, the type of analysis to be performed is specified at first, followed by specific solution settings. For a nonlinear static analysis using SOL400, this can be, e.g. the number of load

increments, methods for controlling stiffness updates or convergence criteria. In order to use Nastran in this particular framework, the loads are defined in a separate *loadcard* file, which is referenced in the bdf file via the *include* command. Another important point in this context is the application of forces in the FE model. In most cases it is not useful to apply forces to all available nodes when a full 3D FE model is considered. A more viable approach is to select the nodes that are expected to be directly affected by aerodynamic loads. With this method a more accurate description of the load conditions in the real model can be achieved. The extraction of these so-called *coupling nodes* is done in the preprocessing step after the FE model has been set up. The coupling node IDs and coordinates are provided in a separate file, which is referenced along with the Nastran bdf file in the para file. If a coupling model is used, it is important to note that the coupling matrix $\boldsymbol{H}$ is only evaluated for the aerodynamic grid points and the coupling nodes. Although the same coupling matrix can be used for both operations in Eqs. (3.6a) and (3.6b), in this particular case two coupling matrices are employed. This is necessary as the forces transferred to the coupling nodes of the structural model are evaluated at the quarter points of the aerodynamic model. In contrast, the displacements obtained from the structural model are interpolated onto the aerodynamic grid (panel corner points). The transformation of forces to the coupling nodes is therefore performed using the coupling matrix $\boldsymbol{H}_f$. In addition, the coupling matrix $\boldsymbol{H}_d$ is applied to interpolate only the displacements from the coupling nodes to the aerodynamic grid. Thus, the displacements of the coupling nodes have to be extracted from the Nastran results file after the structural solution is completed.

When the preprocessing is completed, the simulations begins with calculating the AIC and the coupling matrix. Then the steady vortex lattice solution sequence computes the induced velocities to set up the RHS vector and solves the equations for the panels circulations. The aerodynamic forces are calculated as a function of the circulation and transformed into equivalent structural forces using the coupling matrix. At this point the forces are written into the Nastran loadcard and a subprocess executes Nastran with the bdf file. Once the Nastran solution is completed, the structural deformations of the coupling nodes are extracted from the Nastran *f06* solution file and interpolated back onto the aerodynamic grid. Since a steady vortex lattice method is used here, no wake shedding routine is required. After an update of the grid metric and an optional update of the AIC matrix, the solver checks for convergence of the structural solution. For this purpose the difference between the sum of deformations from the current and the previous solution is compared to a structural residual defined in the para file. If the solution is converged, the results are written into multiple output

files. Otherwise, a new iteration loop is started until the convergence criterion is reached.

3.2 Linearisation of the Aeroelastic System

In the following sections a method for aeroelastic stability analysis of highly flexible wings will be derived. As already mentioned in Section 2.1.2, the presented methods to predict flutter do not take into account wings undergoing large deformations. Due to the fact of flight vehicles becoming increasingly more elastic, considerable efforts have been made in the last years to extend existing and develop new methods. Notable early works include the studies by Cesnik, Hodges and Patil in 1998 [26] and 2001 [27], which developed a low-order nonlinear aeroelastic analysis tool to investigate the effect of aerodynamic and structural nonlinearities on aeroelastic stability. A more recent study on geometrically nonlinear aeroelastic stability analysis of a very flexible wing is found in reference [28]. Here, the loads for the structural nonlinear static analysis are computed using the steady vortex lattice method, similar to the static coupling solution used in this thesis. In contrast, a nonplanar doublet lattice method is applied to calculate the unsteady aerodynamic loads for the flutter equations. A different approach to determine the stability of an aeroelastic system is presented in references [16] and [29]. In these cases, the unsteady VLM is transformed into a discrete-time state-space model, which is integrated into a coupled aeroelastic framework along with a model for flexible-body dynamics. The nonlinear formulation of this framework allows for fully nonlinear aeroelastic simulations in the time domain, while a linearisation of the equations leads to a monolithic discrete-time state-space model for the aeroelastic system. This linear state-space model is used for stability analysis solving an eigenvalue problem.

In this thesis a similar approach is used for the proposed method of stability analysis. At first, the goal is to create a linear state-space model for the aerodynamic model, where equations will be derived from the unsteady VL implementation. Afterwards, the linearisation of the structural response using a modal approach in generalised coordinates is straightforward. Once both aerodynamics and structural dynamics are represented by linear state-space models, these can be combined and integrated into a monolithic linear state-space model to describe the system's aeroelastic behaviour. The basics of linear state-space models are therefore explained in the following.

3.2.1 Basics of Linear State-space Models

State-space models as part of control theory are used to model and control the dynamic behaviour of a system. In general, the states of a dynamical system are referred to as "a collection of variables that completely characterises the motion of a system for the purpose of predicting future motion" [30]. A very simple example can be a system of planets, where the systems' states are the locations and the velocities of the planets. Another example is the generic driven spring-mass system with damping, shown in Fig. 3.3, with the equation of motion defined by

$$m\ddot{z} + d\dot{z} + kz = f \ , \tag{3.7}$$

where z denotes the displacement of the mass m, $\dot{z}$ and $\ddot{z}$ represent the first (velocity) and second (acceleration) time derivative of z, while d is the damping constant, k the spring constant and f is the applied force. In this case, the states of the system are the position and the velocity of the mass. These state variables are collected in the *state vector* $\boldsymbol{x}$. Furthermore, the control or input variables, e.g. the force f in Eq. (3.7), are represented by the *input vector* $\boldsymbol{u}$ and the measured signal by the *output vector* $\boldsymbol{y}$. A general formulation of a state-space model can then be expressed by means of the differential equation [30]

$$\frac{d\boldsymbol{x}}{dt} = \dot{\boldsymbol{x}} = g\left(\boldsymbol{x}, \boldsymbol{u}\right) \ , \qquad \boldsymbol{y} = h\left(\boldsymbol{x}, \boldsymbol{u}\right) \ . \tag{3.8}$$

The *order* of the system is defined by the dimension of the state vector. Thus, the spring-mass system mentioned above is called a second-order system. In Eq. (3.8), the rate of change of the state vector $\dot{\boldsymbol{x}}$ is defined by the function g of the state vector $\boldsymbol{x}$ and the input vector $\boldsymbol{u}$. The output vector $\boldsymbol{y}$ is determined using the function h of the

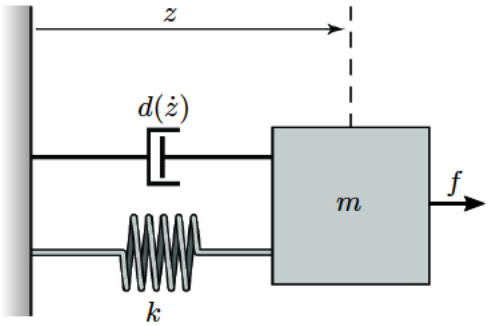

Figure 3.3: Driven mass-spring-damper model [30]

state $\boldsymbol{x}$ and the input vector $\boldsymbol{u}$. An important feature of this equation is *time invariance*, as both functions are not dependent on time. The properties of time invariant systems do not change with time, i.e. when an input $\boldsymbol{u}(t)$ results in an output $\boldsymbol{y}(t)$, a time shifted input $\boldsymbol{u}(t+\Delta t)$ results in an output $\boldsymbol{y}(t+\Delta t)$. If g and h are linear functions of $\boldsymbol{x}$ and $\boldsymbol{u}$, the system is called a linear state-space system and defined by the relations

$$\dot{\boldsymbol{x}} = \boldsymbol{A}\boldsymbol{x} + \boldsymbol{B}\boldsymbol{u} \ , \tag{3.9a}$$

$$\boldsymbol{y} = \boldsymbol{C}\boldsymbol{x} + \boldsymbol{D}\boldsymbol{u} \ . \tag{3.9b}$$

Here, matrix $\boldsymbol{A}$ is called the *dynamics matrix*, $\boldsymbol{B}$ the *control matrix*, $\boldsymbol{C}$ the *sensor matrix* and $\boldsymbol{D}$ the *direct term*, where all matrices are constant. It is important to note that, in many cases, the output vector is not directly affected by the input vector and thus there exists no direct term. Since the system described is both time invariant and linear, it is referred as a *linear time invariant* or LTI system.

So far, the state-space equations have been presented in the *continuous-time* formulation. Under certain conditions, however, it may be more effective to describe the system's behaviour at discrete time steps. In this case, the definition of the system states remains unchanged, but the change of states is now evaluated for each time step. This type of systems is called *discrete-time systems* and is defined by the difference equation

$$\boldsymbol{x}^{n+1} = g\left(\boldsymbol{x}^n, \boldsymbol{u}^n\right) \ , \qquad \boldsymbol{y}^n = h\left(\boldsymbol{x}^n, \boldsymbol{u}^n\right) \ , \tag{3.10}$$

with $n = 0, 1, 2, \ldots$ denoting the time step, $\boldsymbol{x}^n$ the state vector, $\boldsymbol{u}^n$ the input and $\boldsymbol{y}^n$ the output vector at time step n. When a linear discrete-time system is considered, Eq. (3.9a) and Eq. (3.9b) become

$$\boldsymbol{x}^{n+1} = \boldsymbol{A}\boldsymbol{x}^n + \boldsymbol{B}\boldsymbol{u}^n \ , \tag{3.11a}$$

$$\boldsymbol{y}^n = \boldsymbol{C}\boldsymbol{x}^n + \boldsymbol{D}\boldsymbol{u}^n \ , \tag{3.11b}$$

where the matrices $\boldsymbol{A}$, $\boldsymbol{B}$, $\boldsymbol{C}$ and $\boldsymbol{D}$ are constant again and named similarly to the continuous-time approach [30].

In general, the stability of linear systems is divided into *internal* and *external stability*. External stability is achieved when a limited input signal results in a limited output signal. On the other hand, a system is called internally stable if the rate of change of states $\dot{\boldsymbol{x}}(t)$ for any initial state $\boldsymbol{x}_0$ tends to zero at $t \to \infty$. For this thesis only the internal stability is of interest, since in a flutter analysis the linearised aeroelastic state-space model depends exclusively on the system's states. The internal stability

of such a system is only dependent on the dynamics matrix $\boldsymbol{A}$ and can be determined using the eigenvalues λ of this matrix. These can be found solving the equation

$$\det\left(\boldsymbol{\lambda I} - \boldsymbol{A}\right) = 0\ . \tag{3.12}$$

In this case $\det\left(\boldsymbol{\lambda I} - \boldsymbol{A}\right)$ is called the *characteristic polynomial*. A linear system is internally stable, if all eigenvalues λ_i of matrix $\boldsymbol{A}$ have a strictly negative real part:

$$\mathrm{Re}\ \lambda_i < 0\ ; \qquad (i = 1, 2, \ldots, n)\ . \tag{3.13}$$

If any eigenvalue of $\boldsymbol{A}$ has a positive real part, the system is considered internally unstable. It is notable that this stability criterion is only valid for continuous-time systems. In the case of a discrete-time LTI system, internal stability is achieved if all eigenvalues of $\boldsymbol{A}$ in the complex z-plane are located within the unit circle. Thus the magnitudes of all eigenvalues have to be smaller than one:

$$|z_i| < 1\ , \tag{3.14}$$

where z_i denotes the eigenvalues in discrete-time formulation to avoid confusion with the eigenvalues from a continuous-time system. However, the continuous-time eigenvalues and their corresponding eigenvectors can be used not only to determine the stability of the system, but also to describe the oscillation that might occur. The eigenvalue describes the change of the solution with time, which is often referred to as a *mode* of a system. Although the $\boldsymbol{A}$ matrix is real-valued, the eigenvalues can appear in the complex form

$$\lambda_i = \sigma_i \pm i\omega_i\ , \tag{3.15}$$

where their real parts σ_i indicate the decay ratios and the imaginary parts ω_i indicate the frequencies for each mode. In addition, the corresponding eigenvector of the eigenvalue or mode describes the shape of the oscillation and is therefore called a *mode shape* of the system. Similar to the eigenvalues, the eigenvectors $\boldsymbol{v}$ can also appear in complex form:

$$\boldsymbol{v}_i = \boldsymbol{u}_i \pm i\boldsymbol{\omega}_i\ . \tag{3.16}$$

If both the eigenvalues and eigenvectors of a system are known, the system's response for any initial condition can be described using a linear combination of the modes of the system [30, 31].

3.2.2 Derivation of the linearised Aerodynamic Model

Based on the previously presented theoretical fundamentals and details of the aeroelastic solver, a method for aeroelastic stability analysis of highly flexible wings will be developed in the following. The basic idea of this method is first to determine the static aeroelastic equilibrium of the wing using the aeroelastic solver described in Section 3.1.2. Afterwards the dynamic response of the wing to small flow disturbances around this equilibrium can be modelled by means of a linear state-space system. This state-space system should be able to describe the aeroelastic behaviour of the wing and thus must include an aerodynamic and a structural model. Therefore, the state-space system for the aerodynamic model will be derived first, based on the unsteady vortex lattice implementation presented in Section 3.1.1.

Building a state-space system usually begins with the identification of the state variables of the system. These should allow a complete description of the system's motion. Considering the aerodynamic model of an aeroelastic system, relevant variables might be the aerodynamic forces interacting with the structure. In case of the vortex lattice method, however, it can be seen that the aerodynamic forces are functions of the circulation Γ. The basic formulation of the vortex lattice method in Eq. (2.13) in combination with the RHS vector in Eq. (2.16) yields

$$\boldsymbol{AIC} \cdot \boldsymbol{\Gamma}_b = \boldsymbol{RHS} = -\left(\boldsymbol{V}_{rb} + \boldsymbol{V}_{wake} + \boldsymbol{V}_{gust} + \boldsymbol{V}_{el}\right) \cdot \boldsymbol{n} \; . \tag{3.17}$$

Here, $\boldsymbol{\Gamma}_b$ denotes the circulation of bound panels, $\boldsymbol{V}_{rb}$ the rigid body velocity (onflow velocity in a windtunnel test case), while $\boldsymbol{V}_{wake}$ and $\boldsymbol{V}_{el}$ are the velocities induced by the wake and an elastic deformation of the wing. Since the effect of gusts is not taken into account in the stability analysis, the gust induced velocities $\boldsymbol{V}_{gust}$ will be neglected in the following. The wake induced velocities can be calculated as

$$\boldsymbol{V}_{wake} = \boldsymbol{WIC} \cdot \boldsymbol{\Gamma}_w \; , \tag{3.18}$$

where $\boldsymbol{WIC}$ is called the *wake influence coefficients* matrix, which is determined in a similar way to the AIC matrix, but includes the influence coefficients of the wake vortices with circulation $\boldsymbol{\Gamma}_w$ on the collocation points of the bound vortices. The introduction of Eq. (3.18) into Eq. (3.17) and solving for $\boldsymbol{\Gamma}_b$ leads to

$$\boldsymbol{\Gamma}_b = -\boldsymbol{AIC}^{-1} \cdot \left(\boldsymbol{WIC} \cdot \boldsymbol{\Gamma}_w + \boldsymbol{V}_{rb} + \boldsymbol{V}_{el}\right) \cdot \boldsymbol{n} \; . \tag{3.19}$$

Using this equation, the circulation of the bound panels can be expressed by the circulation of the wake panels. Thus, the steady aerodynamic forces ${}^{A}\boldsymbol{F}_s$, as well as the unsteady aerodynamic forces ${}^{A}\boldsymbol{F}_u$, can be described as a function of the wake circulation, as will be shown later on. The wake circulations can therefore be regarded as the states that describe the motion of the system. The state vector at the current time step n is accordingly designated $\boldsymbol{\Gamma}_w^n$ in the following. At this point it has to be decided, whether the system should be formulated as a discrete-time or continuous-time state-space model. Since the unsteady VLM already uses a time-stepping procedure with discrete time steps it seems reasonable to use a discrete-time state-space model for the further derivation. In this case the system is specified to find the solution of the next time step. The evolution of the wake circulation is defined by the wake-shedding process that is described in Section 2.2 and consists of two different operations. In the first step the wake vortex rings are shifted by one panel in downstream direction and a new row of wake vortex rings is created at the trailing edge of the wing. Afterwards, the circulation from the wing trailing edge row is transferred to this new wake row. This routine can be written as

$$\boldsymbol{\Gamma}_w^{n+1} = \boldsymbol{M}_b \cdot \boldsymbol{\Gamma}_b^n + \boldsymbol{M}_w \cdot \boldsymbol{\Gamma}_w^n \,, \tag{3.20}$$

where $\boldsymbol{M}_b$ is the matrix for transferring the bound circulation from the trailing edge row and $\boldsymbol{M}_w$ is the matrix for shifting the wake rows. The result of this equation is the wake circulation at the next time step $\boldsymbol{\Gamma}_w^{n+1}$. Substitution of $\boldsymbol{\Gamma}_b$ using Eq. (3.19) results in

$$\boldsymbol{\Gamma}_w^{n+1} = -\boldsymbol{M}_b \cdot \boldsymbol{AIC}^{-1} \cdot (\boldsymbol{WIC} \cdot \boldsymbol{\Gamma}_w^n + \boldsymbol{V}_{rb} + \boldsymbol{V}_{el}) \cdot \boldsymbol{n} + \boldsymbol{M}_w \cdot \boldsymbol{\Gamma}_w^n \,, \tag{3.21}$$

with $\boldsymbol{M}_b$, $\boldsymbol{M}_w$, $\boldsymbol{AIC}^{-1}$ and $\boldsymbol{WIC}$ being constant matrices. Hence, the wake circulation $\boldsymbol{\Gamma}_w^{n+1}$ during the next time step is only a function of the current wake circulation $\boldsymbol{\Gamma}_w^n$, the velocities $\boldsymbol{V}_{rb}$ and $\boldsymbol{V}_{el}$, as well as the panel normal vectors $\boldsymbol{n}$. Referring to the basic formulation of discrete-time state-space models, which is

$$\boldsymbol{x}^{n+1} = \boldsymbol{A}\boldsymbol{x}^n + \boldsymbol{B}\boldsymbol{u}^n \,, \tag{3.22}$$

only the variables of the input vector $\boldsymbol{u}^n$ have to be defined, since the state vector $\boldsymbol{x}^n$ has already been designated as $\boldsymbol{\Gamma}_w^n$. Accordingly, only the velocities $\boldsymbol{V}_{rb}$, $\boldsymbol{V}_{el}$ and the panel normal vectors $\boldsymbol{n}$ are available as input variables. As the model will be used to describe the dynamic behaviour at a static aeroelastic equilibrium, the rigid body velocity $\boldsymbol{V}_{rb}$ can be assumed constant. For this reason, the velocity $\boldsymbol{V}_{el}$ and the panel normal vectors $\boldsymbol{n}$ are chosen to be part of the input vector due to the elastic motion

of the wing while $\boldsymbol{V}_{rb}$ will be included in the control matrix $\boldsymbol{B}$. Eq. (3.21) can then be rewritten in matrix notation:

$$\begin{aligned}\left\{\boldsymbol{\Gamma}_w\right\}^{n+1} = &\underbrace{\left[\boldsymbol{M}_w - \boldsymbol{M}_b \cdot \boldsymbol{AIC}^{-1} \cdot \boldsymbol{WIC} \cdot \boldsymbol{n}\right]}_{{}^{A}\boldsymbol{A}} \cdot \underbrace{\left\{\boldsymbol{\Gamma}_w\right\}^{n}}_{{}^{A}\boldsymbol{x}} \\ &+ \underbrace{\left[-\boldsymbol{M}_b \cdot \boldsymbol{AIC}^{-1} \cdot {}^{c}\boldsymbol{V}_{rb} \qquad -\boldsymbol{M}_b \cdot \boldsymbol{AIC}^{-1} \cdot \boldsymbol{n}\right]}_{{}^{A}\boldsymbol{B}} \cdot \underbrace{\begin{Bmatrix}\boldsymbol{n} \\ {}^{c}\boldsymbol{V}_{el}\end{Bmatrix}^{n}}_{{}^{A}\boldsymbol{u}} .\end{aligned} \tag{3.23}$$

This equation describes a state-space system in discrete-time formulation, as shown in Eq. (3.22). The index c indicates that the velocities are related to the collocation points of the aerodynamic panels. It can be seen that $\boldsymbol{n}$ appears both in the ${}^{A}\boldsymbol{A}$ and in the ${}^{A}\boldsymbol{B}$ matrix, although it is defined as an input of the system. Due to the linear character of the system the amplitudes of the described motion and thus the changes in the normal vectors are assumed to be small. In this case the assumption of constant normal vectors in matrices ${}^{A}\boldsymbol{A}$ and ${}^{A}\boldsymbol{B}$ seems appropriate. Furthermore, the effect of a change in the normal vectors is also taken into account, since $\boldsymbol{n}$ is a part of the input vector. At this point, the $\boldsymbol{WIC}^{*}$ matrix is introduced, which describes the wake induced velocities projected in the direction of the panel normal vectors:

$$\boldsymbol{WIC}^{*} = \boldsymbol{WIC} \cdot \boldsymbol{n} \tag{3.24}$$

The matrices ${}^{A}\boldsymbol{A}$ and ${}^{A}\boldsymbol{B}$ are referred to as the aerodynamic dynamics and the aerodynamic control matrix respectively in the following and are determined by

$${}^{A}\boldsymbol{A} = \left[\boldsymbol{M}_w - \boldsymbol{M}_b \cdot \boldsymbol{AIC}^{-1} \cdot \boldsymbol{WIC}^{*}\right] \in \mathbb{R}^{n_w \times n_w} , \tag{3.25}$$

$${}^{A}\boldsymbol{B} = \left[\underbrace{-\boldsymbol{M}_b \cdot \boldsymbol{AIC}^{-1} \cdot {}^{c}\boldsymbol{V}_{rb}{}^{T}}_{{}^{A}\boldsymbol{B}_1} \qquad \underbrace{-\boldsymbol{M}_b \cdot \boldsymbol{AIC}^{-1} \cdot \boldsymbol{n}^{T}}_{{}^{A,c}\boldsymbol{B}_2}\right] \in \mathbb{R}^{n_w \times 6n_b} . \tag{3.26}$$

It should be noted that the vectors $\boldsymbol{V}_{rb}$ and $\boldsymbol{n}$ appear in transposed form in the ${}^{A}\boldsymbol{B}$ matrix. This is necessary to bring the sub-matrices into the correct dimension for

matrix multiplication with the input vector. The state and the input vector are

$$
\begin{aligned}
{}^{A}\boldsymbol{x} &= \left\{ \Gamma_{w,i} \right\} \in \mathbb{R}^{n_w} \quad (i = 1, \ldots, n_w) \, , \\
{}^{A}\boldsymbol{u} &= \left\{ \begin{array}{c} {}^{x}n_j \\ {}^{y}n_j \\ {}^{z}n_j \\ {}^{x}V_{el,j} \\ {}^{y}V_{el,j} \\ {}^{z}V_{el,j} \end{array} \right\} \in \mathbb{R}^{6n_b} \quad (j = 1, \ldots, n_b) \, ,
\end{aligned}
\tag{3.27}
$$

where ${}^{A}\boldsymbol{x}$ is a vector of dimension n_w, which is the number of wake panels. The vectors $\boldsymbol{n}$ and $\boldsymbol{V}_{el}$ both have the dimension $3n_b$, which means three times the number of bound panels n_b due to the three coordinate directions x, y and z. Thus, the input vector ${}^{A}\boldsymbol{u}$ has the dimension $6n_b$. In addition, ${}^{A}\boldsymbol{A}$ is a matrix of dimension $n_w \times n_w$ and ${}^{A}\boldsymbol{B}$ a matrix of dimension $n_w \times 6n_b$. The behaviour of the system's states over time can now be determined completely using the equation

$$
\left\{ \boldsymbol{\Gamma}_w \right\}^{n+1} = \left[{}^{A}\boldsymbol{A} \right] \cdot \left\{ \boldsymbol{\Gamma}_w \right\}^{n} + \left[{}^{A}\boldsymbol{B}_1 \quad {}^{A,c}\boldsymbol{B}_2 \right] \cdot \left\{ \begin{array}{c} \boldsymbol{n} \\ {}^{c}\boldsymbol{V}_{el} \end{array} \right\}^{n} \, . \tag{3.28}
$$

It is now possible to describe the resulting aerodynamic forces as outputs of the state-space system, according to the relation

$$
\boldsymbol{y}^n = \boldsymbol{C}\boldsymbol{x}^n + \boldsymbol{D}\boldsymbol{u}^n \, . \tag{3.29}
$$

In the unsteady vortex lattice solver used the total forces are the sum of the steady and unsteady aerodynamic forces. The steady aerodynamic forces ${}^{A}\boldsymbol{F}_s$ are given by

$$
{}^{A}\boldsymbol{F}_{s,i} = \rho \cdot \boldsymbol{\Gamma}_{eff,i} \cdot (\boldsymbol{V}_{rb,i} + \boldsymbol{V}_{el,i} + \boldsymbol{V}_{gust,i}) \times \boldsymbol{r}_i \, , \tag{3.30}
$$

where again the gust induced velocities are neglected in the further derivation. At this point it should be noted that the index i, representing the number of the (bound) aerodynamic panel considered, is disregarded in the following for the sake of simplification. The effective circulation $\boldsymbol{\Gamma}_{eff}$ is defined as the difference of the circulation of the

corresponding aerodynamic panel and the adjacent panel in chordwise downstream direction, except for the panels at the leading edge. It is calculated from the bound circulation using

$$\boldsymbol{\Gamma}_{eff} = \boldsymbol{M}_{eff} \cdot \boldsymbol{\Gamma}_b \,, \tag{3.31}$$

with $\boldsymbol{M}_{eff}$ being a matrix of dimension $n_b \times n_b$. Introducing Eq. (3.31) together with Eq. (3.19) into Eq. (3.30) results in

$$\begin{aligned} {}^{A}\boldsymbol{F}_s &= -\rho \cdot \boldsymbol{M}_{eff} \cdot \boldsymbol{AIC}^{-1} \cdot (\boldsymbol{WIC} \cdot \boldsymbol{\Gamma}_w + {}^{c}\boldsymbol{V}_{rb} + {}^{c}\boldsymbol{V}_{el}) \cdot \boldsymbol{n} \cdot ({}^{q}\boldsymbol{V}_{rb} + {}^{q}\boldsymbol{V}_{el}) \times \boldsymbol{r} \\ &= -\rho \cdot \boldsymbol{M}_{eff} \cdot \boldsymbol{AIC}^{-1} \cdot (\boldsymbol{WIC}^* \cdot {}^{q}\boldsymbol{V}_{rb} \times \boldsymbol{r} \cdot \boldsymbol{\Gamma}_w \\ &\qquad + \cancel{\boldsymbol{WIC}^* \cdot {}^{q}\boldsymbol{V}_{el} \times \boldsymbol{r} \cdot \boldsymbol{\Gamma}_w} \\ &\qquad + {}^{c}\boldsymbol{V}_{rb} \cdot \boldsymbol{n} \cdot {}^{q}\boldsymbol{V}_{rb} \times \boldsymbol{r} + {}^{c}\boldsymbol{V}_{rb} \cdot \boldsymbol{n} \cdot {}^{q}\boldsymbol{V}_{el} \times \boldsymbol{r} \\ &\qquad + {}^{c}\boldsymbol{V}_{el} \cdot \boldsymbol{n} \cdot {}^{q}\boldsymbol{V}_{rb} \times \boldsymbol{r} + \cancel{{}^{c}\boldsymbol{V}_{el} \cdot \boldsymbol{n} \cdot {}^{q}\boldsymbol{V}_{el} \times \boldsymbol{r}}) \,. \end{aligned} \tag{3.32}$$

As can be seen, the steady forces depend on the state variables $\boldsymbol{\Gamma}_w$ and the input variables $\boldsymbol{V}_{el}$ and $\boldsymbol{n}$. The index q is introduced as the velocities for calculating the aerodynamic forces are evaluated at the quarter points of the aerodynamic panels. In contrast, the velocities in the RHS vector of the original VLM formulation (Eq. (3.17)) are related to the collocation points. This will become particularly important during the derivation of the linearised aeroelastic model in Section 3.2.3. Eq. (3.32) shall now be transformed into the form of Eq. (3.29) using the corresponding state vector and input vector of the presented state-space system. Unfortunately, the isolation of velocities is not straightforward in this case since they are linked to a cross-product with vector $\boldsymbol{r}$. This problem can be resolved using a so-called *skew-symmetric matrix* $\boldsymbol{R}$ to evaluate the cross-product by matrix multiplication:

$$\boldsymbol{r}_i \times \boldsymbol{V}_{rb,i} = \boldsymbol{R}_i \cdot \boldsymbol{V}_{rb,i} \,, \tag{3.33}$$

$$\text{with} \qquad \boldsymbol{r}_i = \begin{Bmatrix} r_x \\ r_y \\ r_z \end{Bmatrix}_i \,, \qquad \boldsymbol{R}_i = \begin{bmatrix} 0 & -r_z & r_y \\ r_z & 0 & -r_x \\ -r_y & r_x & 0 \end{bmatrix}_i \,.$$

In addition, the two crossed-out terms appearing in Eq. (3.32) cannot be expressed with the present linear system. One includes the product of the input $\boldsymbol{V}_{el}$ and the state $\boldsymbol{\Gamma}_w$, while the other includes a quadratic part of $\boldsymbol{V}_{el}$. These are called *higher-order terms* and are not considered in the following. The equation for the steady forces can

then be rewritten in state-space notation as

$$\left\{ {}^{A}\boldsymbol{F}_s \right\}^n = \underbrace{\left[\rho \cdot \boldsymbol{M}_{eff} \cdot \boldsymbol{AIC}^{-1} \cdot \boldsymbol{WIC}^* \cdot \boldsymbol{R} \cdot {}^{q}\boldsymbol{V}_{rb} \right]}_{{}^{A}\boldsymbol{C}_s} \cdot \left\{ \boldsymbol{\Gamma}_w \right\}^n \tag{3.34}$$

$$+ \underbrace{\rho \cdot \boldsymbol{M}_{eff} \cdot \boldsymbol{AIC}^{-1} \cdot \left[{}^{c}\boldsymbol{V}_{rb} \cdot \boldsymbol{R} \cdot {}^{q}\boldsymbol{V}_{rb} \qquad {}^{c}\boldsymbol{V}_{rb} \cdot \boldsymbol{n} \cdot \boldsymbol{R} + \boldsymbol{n} \cdot \boldsymbol{R} \cdot {}^{q}\boldsymbol{V}_{rb} \right]}_{{}^{A}\boldsymbol{D}_s} \cdot \begin{Bmatrix} \boldsymbol{n} \\ {}^{q|c}\boldsymbol{V}_{el} \end{Bmatrix}^n .$$

One problem concerning this equation are the dimensions of the velocity vectors, the panel normal vectors and the skew-symmetric matrix appearing in the constant matrices $\boldsymbol{C}$ and $\boldsymbol{D}$. These are not compatible with the dimensions of the remaining matrices even if they were in transposed form, as used in Eq. (3.26). In order to solve this issue, the vector ${}^{q|c}\boldsymbol{V}_{rb}$ and $\boldsymbol{n}$, as well as the matrix $\boldsymbol{R}$ are transformed into the equivalent matrices ${}^{q|c}\tilde{\boldsymbol{V}}_{rb}$, $\tilde{\boldsymbol{n}}$ and $\tilde{\boldsymbol{R}}$ containing the entries for each panel blockwise in diagonal form, see Appendix A.1. The steady aerodynamic sensor matrix ${}^{A}\boldsymbol{C}_s$ and the sub-matrices of the steady aerodynamic direct term ${}^{A}\boldsymbol{D}_s$ are then defined by

$${}^{A}\boldsymbol{C}_s = \left[\rho \cdot \tilde{\boldsymbol{R}} \cdot {}^{q}\tilde{\boldsymbol{V}}_{rb} \cdot \boldsymbol{M}_{eff} \cdot \boldsymbol{AIC}^{-1} \cdot \boldsymbol{WIC}^* \right] \in \mathbb{R}^{3n_b \times n_w} , \tag{3.35}$$

$${}^{A}\boldsymbol{D}_{s,1} = \left[\rho \cdot \tilde{\boldsymbol{R}} \cdot {}^{q}\tilde{\boldsymbol{V}}_{rb} \cdot \boldsymbol{M}_{eff} \cdot \boldsymbol{AIC}^{-1} \cdot {}^{c}\tilde{\boldsymbol{V}}_{rb}{}^{T} \right] \in \mathbb{R}^{3n_b \times 3n_b} , \tag{3.36}$$

$${}^{A,q}\boldsymbol{D}_{s,2} = \rho \cdot \left[{}^{c}\tilde{\boldsymbol{V}}_{rb} \cdot \boldsymbol{M}_{eff} \cdot \boldsymbol{AIC}^{-1} \cdot \left(\tilde{\boldsymbol{R}} \cdot \tilde{\boldsymbol{n}} \right)^T \right] \in \mathbb{R}^{3n_b \times 3n_b} , \tag{3.37}$$

$${}^{A,c}\boldsymbol{D}_{s,2} = \rho \cdot \left[\tilde{\boldsymbol{n}} \cdot \boldsymbol{M}_{eff} \cdot \boldsymbol{AIC}^{-1} \cdot \left(\tilde{\boldsymbol{R}} \cdot {}^{q}\tilde{\boldsymbol{V}}_{rb} \right)^T \right] \in \mathbb{R}^{3n_b \times 3n_b} . \tag{3.38}$$

Compared to Eq. (3.34), the order of the variables has been changed to obtain the $\boldsymbol{C}$ and $\boldsymbol{D}$ matrices in the correct dimension for matrix multiplication with the input vector. The steady forces can finally be determined using

$$\left\{ {}^{A}\boldsymbol{F}_s \right\}^n = \left[{}^{A}\boldsymbol{C}_s \right] \cdot \left\{ \boldsymbol{\Gamma}_w \right\}^n + \left[{}^{A}\boldsymbol{D}_{s,1} \quad {}^{A,q}\boldsymbol{D}_{s,2} + {}^{A,c}\boldsymbol{D}_{s,2} \right] \cdot \begin{Bmatrix} \boldsymbol{n} \\ {}^{q|c}\boldsymbol{V}_{el} \end{Bmatrix}^n . \tag{3.39}$$

Here, the steady force vector ${}^{A}\boldsymbol{F}_s{}^n$ is of dimension $3n_b$, the matrix ${}^{A}\boldsymbol{C}_s$ is of dimension $3n_b \times n_w$ and the matrices ${}^{A}\boldsymbol{D}_{s,1}$ and ${}^{A,q|c}\boldsymbol{D}_{s,2}$ are of dimension $3n_b \times 3n_b$.

While the steady forces depend on the bound circulation in the original vortex lattice implementation, the unsteady aerodynamic forces ${}^{A}\boldsymbol{F}_u$ depend on the time

derivative of the bound circulation rather than on the bound circulation itself. These can be determined using the relation

$$ {}^{A}\boldsymbol{F}_u = \rho \cdot \boldsymbol{A}_p \cdot \frac{\partial \boldsymbol{\Gamma}_b}{\partial t} \cdot \boldsymbol{n} \ , \tag{3.40} $$

where $\boldsymbol{A}_p$ denotes the panel areas of the corresponding bound panels. Again, Eq. (3.19) can be introduced into this equation and applying the product rule results in

$$ \begin{aligned} {}^{A}\boldsymbol{F}_u &= -\rho \cdot \boldsymbol{A}_p \cdot \frac{\partial \left(\boldsymbol{AIC}^{-1} \cdot (\boldsymbol{WIC} \cdot \boldsymbol{\Gamma}_w + {}^{c}\boldsymbol{V}_{rb} + {}^{c}\boldsymbol{V}_{el}) \cdot \boldsymbol{n} \right)}{\partial t} \cdot \boldsymbol{n} \\ &= -\rho \cdot \boldsymbol{A}_p \cdot \boldsymbol{AIC}^{-1} \cdot \Bigg(\underbrace{\frac{\partial \left(\boldsymbol{WIC} \cdot \boldsymbol{\Gamma}_w + {}^{c}\boldsymbol{V}_{rb} + {}^{c}\boldsymbol{V}_{el} \right)}{\partial t} \cdot \boldsymbol{n}}_{T_1} \\ &\qquad + \underbrace{(\boldsymbol{WIC} \cdot \boldsymbol{\Gamma}_w + {}^{c}\boldsymbol{V}_{rb} + {}^{c}\boldsymbol{V}_{el}) \cdot \frac{\partial \boldsymbol{n}}{\partial t}}_{T_2} \Bigg) \cdot \boldsymbol{n} \ . \end{aligned} \tag{3.41} $$

For simplification, the equation is divided into the terms T_1 and T_2, which will be treated separately in the following. The term T_1 includes the time derivative of the wake circulation, which will need special treatment. Recalling the first-order backward scheme in Eq. (3.4) as part of the unsteady vortex lattice implementation, its application on the wake circulation leads to

$$ \frac{\partial \boldsymbol{\Gamma}_w}{\partial t} \approx \frac{\boldsymbol{\Gamma}_w^{n+1} - \boldsymbol{\Gamma}_w^{n}}{\Delta t} \ , \tag{3.42} $$

with Δt being the time step size. In order to use this scheme in a state-space formulation, the time derivative is now calculated by the difference between the next time step $n+1$ and the current time step n. This approximation is then applied to T_1, which results in

$$ T_1 = \left(\boldsymbol{WIC} \cdot \frac{\boldsymbol{\Gamma}_w^{n+1} - \boldsymbol{\Gamma}_w^{n}}{\Delta t} + {}^{c}\dot{\boldsymbol{V}}_{rb} + {}^{c}\dot{\boldsymbol{V}}_{el} \right) \cdot \boldsymbol{n} \ , \tag{3.43} $$

where $\dot{\boldsymbol{V}}_{rb}$ and $\dot{\boldsymbol{V}}_{el}$ denote the first time derivative (acceleration) of the rigid body velocity and the elastic velocity respectively. The substitution of $\boldsymbol{\Gamma}_w^{n+1}$ using Eq. (3.8)

yields

$$
\begin{aligned}
T_1 &= \left(\boldsymbol{WIC} \cdot \frac{1}{\Delta t} \cdot \left({}^{A}\boldsymbol{A} \cdot \boldsymbol{\Gamma}_w^n + {}^{A}\boldsymbol{B}_1 \cdot \boldsymbol{n}^n + {}^{A}\boldsymbol{B}_2 \cdot {}^{c}\boldsymbol{V}_{el}^n - \boldsymbol{\Gamma}_w^n \right) + {}^{c}\dot{\boldsymbol{V}}_{rb} + {}^{c}\dot{\boldsymbol{V}}_{el} \right) \cdot \boldsymbol{n} \\
&= \underbrace{\boldsymbol{WIC}^* \cdot \frac{1}{\Delta t} \cdot \left({}^{A}\boldsymbol{A} - \boldsymbol{I} \right)}_{{}^{A}\boldsymbol{C}_{T_1}} \cdot \boldsymbol{\Gamma}_w^n + \underbrace{\boldsymbol{WIC}^* \cdot \frac{1}{\Delta t} \cdot {}^{A}\boldsymbol{B}_1}_{{}^{A}\boldsymbol{D}_{T_1,1}} \cdot \boldsymbol{n}^n + \cancelto{0}{{}^{c}\dot{\boldsymbol{V}}_{rb} \cdot \boldsymbol{n}} \text{ at equilibrium} \\
&+ \underbrace{\boldsymbol{WIC}^* \cdot \frac{1}{\Delta t} \cdot {}^{A}\boldsymbol{B}_2}_{{}^{A}\boldsymbol{D}_{T_1,2}} \cdot {}^{c}\boldsymbol{V}_{el}^n + \boldsymbol{n} \cdot {}^{c}\dot{\boldsymbol{V}}_{el} \\
&= {}^{A}\boldsymbol{C}_{T_1} \cdot \boldsymbol{\Gamma}_w^n + {}^{A}\boldsymbol{D}_{T_1,1} \cdot \boldsymbol{n}^n + {}^{A}\boldsymbol{D}_{T_1,2} \cdot {}^{c}\boldsymbol{V}_{el}^n + \boldsymbol{n} \cdot {}^{c}\dot{\boldsymbol{V}}_{el}^n \, .
\end{aligned}
\tag{3.44}
$$

In this case the terms are sorted according to the appearing state or input variables. When the system is considered at the steady aeroelastic equilibrium, $\boldsymbol{V}_{rb}$ is assumed constant and thus the acceleration term $\dot{\boldsymbol{V}}_{rb} \cdot \boldsymbol{n}$ is neglected. The elastic acceleration $\dot{\boldsymbol{V}}_{el}$, however, is directly affected by the elastic velocity $\boldsymbol{V}_{el}$ and has therefore to be taken into account. Since $\boldsymbol{V}_{el}$ already is a part of the input vector, it seems reasonable to choose $\dot{\boldsymbol{V}}_{el}$ as an additional input variable. The term T_2 of Eq. (3.41) is treated in a similar way:

$$
\begin{aligned}
T_2 &= \left(\boldsymbol{WIC} \cdot \boldsymbol{\Gamma}_w^n + {}^{c}\boldsymbol{V}_{rb} + {}^{c}\boldsymbol{V}_{el} \right) \cdot \dot{\boldsymbol{n}} \\
&= \cancel{\boldsymbol{WIC} \cdot \boldsymbol{\Gamma}_w^n \cdot \dot{\boldsymbol{n}}^n} + {}^{c}\boldsymbol{V}_{rb} \cdot \dot{\boldsymbol{n}}^n + \cancel{{}^{c}\boldsymbol{V}_{el} \cdot \dot{\boldsymbol{n}}^n} \, ,
\end{aligned}
\tag{3.45}
$$

where $\dot{\boldsymbol{n}}$ represents the first time derivative of the panel normal vectors. It is related to $\boldsymbol{n}$ in a similar way as $\dot{\boldsymbol{V}}_{el}$ is related to $\boldsymbol{V}_{el}$ and is also consequently assigned to the input vector. As a result, two higher-order terms appear in T_2, which cannot be considered in the further derivation. With both terms T_1 and T_2 being evaluated, an introduction of Eq. (3.44) and Eq. (3.45) in Eq. (3.41) gives

$$
\begin{aligned}
{}^{A}\boldsymbol{F}_u &= -\rho \cdot \boldsymbol{A}_p \cdot \boldsymbol{AIC}^{-1} \cdot (T_1 + T_2) \cdot \boldsymbol{n} \\
&= -\rho \cdot \boldsymbol{A}_p \cdot \boldsymbol{AIC}^{-1} \cdot \Big({}^{A}\boldsymbol{C}_{T_1} \cdot \boldsymbol{\Gamma}_w^n + {}^{A}\boldsymbol{D}_{T_1,1} \cdot \boldsymbol{n}^n + {}^{A}\boldsymbol{D}_{T_2,2} \cdot {}^{c}\boldsymbol{V}_{el}^n \\
&\qquad + \boldsymbol{n} \cdot {}^{c}\dot{\boldsymbol{V}}_{el}^n + {}^{c}\boldsymbol{V}_{rb} \cdot \dot{\boldsymbol{n}}^n \Big) \cdot \boldsymbol{n} \, .
\end{aligned}
\tag{3.46}
$$

Four instead of two different input variables are included in this equation. However, the state vector only contains the wake circulation $\boldsymbol{\Gamma}_w$ and the corresponding unsteady aerodynamic sensor matrix ${}^{A}\boldsymbol{C}_u$ is

$$
{}^{A}\boldsymbol{C}_u = \left[-\rho \cdot \frac{1}{\Delta t} \cdot \tilde{\boldsymbol{n}} \cdot \boldsymbol{A}_p \cdot \boldsymbol{AIC}^{-1} \cdot \boldsymbol{WIC}^* \cdot \left({}^{A}\boldsymbol{A} - \boldsymbol{I} \right) \right] \in \mathbb{R}^{3n_b \times n_w} \, , \tag{3.47}
$$

where $\boldsymbol{I}$ denotes an identity matrix. The sub-matrices of the unsteady aerodynamic direct term ${}^{A}\boldsymbol{D}_u$ can be determined by

$$ {}^{A}\boldsymbol{D}_{u,1} = \left[-\rho \cdot \frac{1}{\Delta t} \cdot \tilde{\boldsymbol{n}} \cdot \boldsymbol{AIC}^{-1} \cdot \boldsymbol{A}_p \cdot \boldsymbol{WIC}^{*} \cdot {}^{A}\boldsymbol{B}_1 \right] \in \mathbb{R}^{3n_b \times 3n_b} , \tag{3.48} $$

$$ {}^{A,c}\boldsymbol{D}_{u,2} = \left[-\rho \cdot \frac{1}{\Delta t} \cdot \tilde{\boldsymbol{n}} \cdot \boldsymbol{AIC}^{-1} \cdot \boldsymbol{A}_p \cdot \boldsymbol{WIC}^{*} \cdot {}^{A}\boldsymbol{B}_2 \right] \in \mathbb{R}^{3n_b \times 3n_b} , \tag{3.49} $$

$$ {}^{A}\boldsymbol{D}_{u,3} = \left[-\rho \cdot \tilde{\boldsymbol{n}} \cdot \boldsymbol{AIC}^{-1} \cdot \boldsymbol{A}_p \cdot {}^{c}\tilde{\boldsymbol{V}}_{rb}{}^{T} \right] \in \mathbb{R}^{3n_b \times 3n_b} , \tag{3.50} $$

$$ {}^{A,c}\boldsymbol{D}_{u,4} = \left[-\rho \cdot \tilde{\boldsymbol{n}} \cdot \boldsymbol{AIC}^{-1} \cdot \boldsymbol{A}_p \cdot \tilde{\boldsymbol{n}}^{T} \right] \in \mathbb{R}^{3n_b \times 3n_b} . \tag{3.51} $$

The unsteady aerodynamic forces ${}^{A}\boldsymbol{F}_u$ can now be expressed in state-space formulation using the equations presented above:

$$ \left\{ {}^{A}\boldsymbol{F}_u \right\}^{n} = \left[{}^{A}\boldsymbol{C}_u \right] \cdot \left\{ \boldsymbol{\Gamma}_w \right\}^{n} + \left[{}^{A}\boldsymbol{D}_{u,1} \quad {}^{A,c}\boldsymbol{D}_{u,2} \quad {}^{A}\boldsymbol{D}_{u,3} \quad {}^{A,c}\boldsymbol{D}_{u,4} \right] \cdot \begin{Bmatrix} \boldsymbol{n} \\ {}^{c}\boldsymbol{V}_{el} \\ \dot{\boldsymbol{n}} \\ {}^{c}\dot{\boldsymbol{V}}_{el} \end{Bmatrix}^{n} . \tag{3.52} $$

In addition, the total aerodynamic force vector ${}^{A}\boldsymbol{F}$ is obtained from the sum of steady and unsteady forces:

$$ \left\{ {}^{A}\boldsymbol{F} \right\}^{n} = \left[{}^{A}\boldsymbol{C}_s + {}^{A}\boldsymbol{C}_u \right] \cdot \left\{ \boldsymbol{\Gamma}_w \right\}^{n} \tag{3.53} $$

$$ + \left[{}^{A}\boldsymbol{D}_{s,1} + {}^{A}\boldsymbol{D}_{u,1} \quad {}^{A,q|c}\boldsymbol{D}_{s,2} + {}^{A,c}\boldsymbol{D}_{u,2} \quad {}^{A}\boldsymbol{D}_{u,3} \quad {}^{A,c}\boldsymbol{D}_{u,4} \right] \cdot \begin{Bmatrix} \boldsymbol{n} \\ {}^{q|c}\boldsymbol{V}_{el} \\ \dot{\boldsymbol{n}} \\ {}^{c}\dot{\boldsymbol{V}}_{el} \end{Bmatrix}^{n} . $$

This completes the derivation of the linearised aerodynamic model. Some remarks on the higher-order terms neglected in the derivation of the steady and unsteady forces shall be added at this point. In case of the steady force in Eq. (3.32) both higher-order terms include the expression $\boldsymbol{V}_{el} \times \boldsymbol{r}$. If an undeformed wing in a generic heave motion is considered, the $\boldsymbol{r}$ vector has only one component in y and the elastic velocity $\boldsymbol{V}_{el}$ has only one component in z direction. The cross-product evaluated in

both neglected terms would then result in a vector with only one component in the x direction. Thus, the resulting forces due to these terms would mainly act in the x direction. Since the contribution of viscous or induced drag forces has also not been considered in the presented state-space system, no forces are modelled in the x or flow direction respectively. This will become important for the aeroelastic stability analysis of the Pazy wing in Section 4.2.4.

3.2.3 Derivation of the linearised Aeroelastic Model

In contrast to the derivation of the aerodynamic model, the derivation of the linear structural model is much simpler and is therefore presented at the beginning of this section. The integration of both models into a monolithic linear state-space model to describe the aeroelastic system will be discussed afterwards. For the linearisation of the structural model the spring-mass system with damping is considered once again, as already shown in Fig. 3.3. The equation of motion for this system was

$$\ddot{z} + \frac{d\dot{z}}{m} + \frac{kz}{m} = \frac{f}{m} \,. \tag{3.54}$$

As already mentioned before, the state variables to completely describe the motion of this system are z and $\dot{z}$. In order to transform this equation into a state-space system, the following substitution is introduced:

$$\begin{aligned} z &= x_1 \,, \\ \dot{x}_1 &= x_2 \,, \\ \dot{x}_2 &= \ddot{x}_1 \,. \end{aligned} \tag{3.55}$$

Using the new variables x_1 and x_2, the equation of motion can be expressed by two linear equations

$$\begin{Bmatrix} \dot{x}_1 \\ \dot{x}_2 \end{Bmatrix} = \begin{bmatrix} 0 & 1 \\ -\frac{k}{m} & -\frac{d}{m} \end{bmatrix} \cdot \begin{Bmatrix} x_1 \\ x_2 \end{Bmatrix} + \begin{bmatrix} 0 \\ \frac{1}{m} \end{bmatrix} \cdot \Big\{ f \Big\} \,, \tag{3.56}$$

which is a linear continuous-time state-space system of the form $\dot{x} = Ax + Bu$. However, in the present case the structural dynamics of the wing shall be modelled using generalised coordinates rather than physical coordinates. For this purpose, the structural displacements caused by an external excitation are expressed using the

modal approach

$$\boldsymbol{x}(t) = \boldsymbol{\Phi} \cdot \boldsymbol{q}(t) = \sum_{i=1}^{n} \boldsymbol{\Phi}_i \cdot q_i(t) \ , \tag{3.57}$$

where the modal matrix $\boldsymbol{\Phi}$ contains the displacements of the system's different natural modes in physical coordinates and $\boldsymbol{q}(t)$ represents the vector of the corresponding generalised coordinates. Similar to the single degree of freedom (DOF) system in Eq. (3.54), the equations of motion for a multi DOFs system in generalised coordinates are written as

$$\begin{aligned} \ddot{\boldsymbol{q}} + \bar{\boldsymbol{M}}^{-1} \cdot \bar{\boldsymbol{D}} \cdot \dot{\boldsymbol{q}} + \bar{\boldsymbol{M}}^{-1} \cdot \bar{\boldsymbol{K}} \cdot \boldsymbol{q} &= \bar{\boldsymbol{M}}^{-1} \cdot \bar{\boldsymbol{f}} \\ &= \bar{\boldsymbol{M}}^{-1} \cdot \boldsymbol{\Phi}^T \cdot \boldsymbol{f} \ , \end{aligned} \tag{3.58}$$

with $\bar{\boldsymbol{M}}$, $\bar{\boldsymbol{D}}$ and $\bar{\boldsymbol{K}}$ being the generalised mass, damping and stiffness matrices. In this particular case the modal approach is based on the natural modes of the system and Rayleigh damping is assumed, thus these matrices exist in diagonal form. This system can be transformed into a state-space system in the same manner as shown for the spring-mass system, which results in

$$\begin{Bmatrix} \dot{\boldsymbol{q}}_1 \\ \dot{\boldsymbol{q}}_2 \end{Bmatrix} = \begin{bmatrix} \boldsymbol{0} & \boldsymbol{I} \\ -\boldsymbol{\Omega} & -\bar{\boldsymbol{M}}^{-1} \cdot \bar{\boldsymbol{D}} \end{bmatrix} \cdot \begin{Bmatrix} \boldsymbol{q}_1 \\ \boldsymbol{q}_2 \end{Bmatrix} + \begin{bmatrix} \boldsymbol{0} \\ \bar{\boldsymbol{M}}^{-1} \cdot \boldsymbol{\Phi}^T \end{bmatrix} \cdot \left\{ \boldsymbol{f} \right\} \ , \tag{3.59}$$

$$\text{with} \qquad \boldsymbol{\Omega} = \boldsymbol{\omega}^2 = \bar{\boldsymbol{M}}^{-1} \cdot \bar{\boldsymbol{K}} \ ,$$

where $\boldsymbol{\Omega}$ is a diagonal matrix containing the squares of all natural frequencies $\boldsymbol{\omega}$. Some additional comments on the workflow of the specific implementation developed for this work shall be given here, although this is explained in detail at the end of this section. The eigenvalues $\lambda = \omega^2$ and the corresponding mode shapes or eigenvectors in physical coordinates, gathered in the modal matrix $\boldsymbol{\Phi}$, will be computed by Nastran SOL400. The eigenvalue analysis in Nastran provides two different methods for normalising the eigenvectors. For this work the default option has been chosen, which normalises the eigenvectors to unit value of the generalised mass [32]. This brings the advantage of the mass matrix $\bar{\boldsymbol{M}}$ being an identity matrix and being eliminated in Eq. (3.59). For this specific case, the state-space equation can be rewritten as

$$\begin{Bmatrix} \dot{q}_{1,i} \\ \dot{q}_{2,i} \end{Bmatrix} = \underbrace{\begin{bmatrix} 0 & 1 \\ -\Omega_i & -D_i \end{bmatrix}}_{{}^{S}\boldsymbol{A}} \cdot \underbrace{\begin{Bmatrix} q_{1,i} \\ q_{2,i} \end{Bmatrix}}_{{}^{S}\boldsymbol{x}} + \underbrace{\begin{bmatrix} \boldsymbol{0} \\ {\boldsymbol{\Phi}_i}^T \end{bmatrix}}_{{}^{S}\boldsymbol{B}} \cdot \underbrace{\left\{ {}^{S}\boldsymbol{F} \right\}}_{{}^{S}\boldsymbol{u}} \ , \tag{3.60}$$

$$(i = 1, 2, \ldots, n_m) \ .$$

The number of modes considered is designated n_m, ${}^{S}\boldsymbol{A}$ denotes the structural dynamics matrix of dimension $2n_m \times 2n_m$ and ${}^{S}\boldsymbol{B}$ the structural control matrix of dimension $2n_m \times 3n_{fe}$. The state vector ${}^{S}\boldsymbol{x}$ contains the generalised coordinates $\boldsymbol{q}_1$ for the considered modes and the first time derivatives of the generalised coordinates $\boldsymbol{q}_2$ which can be seen as the generalised velocities. The structural input vector ${}^{s}\boldsymbol{F}$ includes the structural force components acting on all nodes of the finite element model and has the dimension $3n_{fe}$.

Unfortunately, the structural state-space model described with Eq. (3.60) is presented in continuous-time formulation. Due to the unsteady vortex lattice implementation used, the aerodynamic model was derived and formulated as a discrete-time system. In order to merge both models, one of them has to be transformed from one formulation to the other. Since the conversion of a continuous-time into a discrete-time state-space system is easier and than vice versa, the structural model will be converted. In addition, a discrete-time aeroelastic system is more suitable for verification using a modal solver in the time domain. The conversion of a linear continuous-time into a linear discrete-time state-space model is performed by means of the so-called *matrix exponential*. Considering the continuous-time system of the structural model in Eq. (3.60) the equivalent discrete-time system is

$$\begin{Bmatrix} \boldsymbol{q}_1 \\ \boldsymbol{q}_2 \end{Bmatrix}^{n+1} = \underbrace{\left[e^{\left(\Delta t \cdot {}^{S}\boldsymbol{A}\right)} \right]}_{{}^{S}\bar{\boldsymbol{A}}} \cdot \begin{Bmatrix} \boldsymbol{q}_1 \\ \boldsymbol{q}_2 \end{Bmatrix}^{n} + \underbrace{\left[{}^{S}\boldsymbol{A}^{-1} \cdot \left(e^{\left(\Delta t \cdot {}^{S}\boldsymbol{A}\right)} - \boldsymbol{I} \right) \cdot {}^{S}\boldsymbol{B} \right]}_{{}^{S}\bar{\boldsymbol{B}}} \cdot \left\{ {}^{S}\boldsymbol{F} \right\}^{n} \ , \quad (3.61)$$

with Δt representing the desired time step size. The resulting dynamics matrix and the control matrix are designated ${}^{S}\bar{\boldsymbol{A}}$ and ${}^{S}\bar{\boldsymbol{B}}$.

The integration of both the structural and the aerodynamic model into a monolithic aeroelastic state-space system is performed by expressing the inputs of one system with the states of the other system. Recalling Eq. (3.28) and Eq. (3.53) of the aerodynamic model, the inputs are the panel normal vectors $\boldsymbol{n}$, the elastic velocity $\boldsymbol{V}_{el}$ and their time derivatives $\dot{\boldsymbol{n}}$ and $\dot{\boldsymbol{V}}_{el}$ respectively. It is obvious that the normal vectors change depending on the deformation of the wing, where the deformation can be directly expressed using the modal approach shown in Eq. (3.57). The normal vectors, however, are determined using the relation

$$\boldsymbol{n} = \sum_{i=1}^{n_m} \frac{\partial \boldsymbol{n}}{\partial \boldsymbol{\Phi}_i} \cdot \boldsymbol{q}_{1,i} \ , \quad (3.62)$$

where $\frac{\partial \boldsymbol{n}}{\partial \boldsymbol{\Phi}_i}$ is the partial derivative of the panel normal vectors with respect to the eigenvectors of the i-th mode. This expression describes the change in $\boldsymbol{n}$ due to a small excitation of each mode around the static aeroelastic equilibrium. Since no analytical approach for the calculation of the partial derivative was found, the derivative is determined by

$$\frac{\partial \boldsymbol{n}}{\partial \boldsymbol{\Phi}_i} = \frac{\boldsymbol{n}\left(\epsilon, \boldsymbol{\Phi}_i\right) - \boldsymbol{n}_0}{\epsilon} \ . \tag{3.63}$$

In this case, $\boldsymbol{n}\left(\epsilon, \boldsymbol{\Phi}_i\right)$ represents the panel normal vectors if the eigenvector $\boldsymbol{\Phi}_i$ is deflected with a small factor ϵ around the equilibrium and $\boldsymbol{n}_0$ the normal vectors at equilibrium. The elastic velocity $\boldsymbol{V}_{el}$ is obtained using the modal approach in Eq. (3.57), but with the generalised velocity $\boldsymbol{q}_2$ instead of the generalised deflection $\boldsymbol{q}_1$. In this context, two problems are encountered due to the different models of the solution methods. The resulting physical coordinates are still related to the structural grid describing the motion of the FE nodes, while the inputs $\boldsymbol{V}_{el}$ need to be defined at the collocation points of the aerodynamic grid. Therefore, the velocities have to be interpolated onto the aerodynamic grid points using the coupling interface shown in Eq. (3.6a). Afterwards, the elastic velocities must be interpolated from the aerodynamic grid points to the collocation points. Thus, the velocities due to the elastic deformation of the wing can be expressed by

$${}^{c}\boldsymbol{V}_{el} = \boldsymbol{M}_{cp} \cdot \boldsymbol{H}_d \cdot \boldsymbol{\Phi} \cdot \boldsymbol{q}_2 \ , \tag{3.64}$$

where $\boldsymbol{H}_d$ denotes the coupling matrix for mapping displacements between structural and aerodynamic grid, and $\boldsymbol{M}_{cp}$ is a matrix for interpolation from the aerodynamic grid points to the collocation points. Using these new relations for $\boldsymbol{n}$ and $\boldsymbol{V}_{el}$, the evolution of the aerodynamic state vector can finally be written as

$$\left\{\boldsymbol{\Gamma}_w\right\}^{n+1} = \Bigg[\underbrace{{}^{A}\boldsymbol{A}}_{\boldsymbol{A}_{11}} \ \vdots \ \underbrace{{}^{A}\boldsymbol{B}_1 \cdot \frac{\partial \boldsymbol{n}}{\partial \boldsymbol{\Phi}}}_{\boldsymbol{A}_{12}} \ \vdots \ \underbrace{{}^{A,c}\boldsymbol{B}_2 \cdot \boldsymbol{M}_{cp} \cdot \boldsymbol{H}_d \cdot \boldsymbol{\Phi}}_{\boldsymbol{A}_{13}}\Bigg] \cdot \begin{Bmatrix} \boldsymbol{\Gamma}_w \\ \boldsymbol{q}_1 \\ \boldsymbol{q}_2 \end{Bmatrix}^{n} \ . \tag{3.65}$$

Thus the aerodynamic states at the next time step now only depend on the extended dynamics matrix, including the additional sub-matrices $\boldsymbol{A}_{12}$ and $\boldsymbol{A}_{13}$ of dimension $n_w \times n_m$. Furthermore, the state vector has been expanded by the two generalised coordinates of the structural state vector. However, the behaviour of the generalised coordinates over time determined from the structural model is still tied to an external input of the structural forces ${}^{S}\boldsymbol{F}$.

The integration of the structural model is therefore performed in a similar manner to the aerodynamic model. In this case, the structural forces ${}^{S}\boldsymbol{F}$ are derived from the resulting total aerodynamic forces ${}^{A}\boldsymbol{F}$ by

$$ {}^{S}\boldsymbol{F} = {\boldsymbol{H}_f}^{T} \cdot {}^{A}\boldsymbol{F} \,, \tag{3.66} $$

where $\boldsymbol{H}_f$ is the coupling matrix for transferring the forces from the aerodynamic grid to the structural grid. Recalling Eq. (3.53), the aerodynamic forces have been defined as outputs of the aerodynamic state-space model and hence are related to the corresponding state vector and input vector:

$$ \left\{ {}^{A}\boldsymbol{F} \right\}^{n} = \left[{}^{A}\boldsymbol{C} \right] \cdot \left\{ \boldsymbol{\Gamma}_w \right\}^{n} + \left[{}^{A}\boldsymbol{D}_1 \quad {}^{A}\boldsymbol{D}_2 \quad {}^{A}\boldsymbol{D}_3 \quad {}^{A}\boldsymbol{D}_4 \right] \cdot \left\{ \begin{array}{c} \boldsymbol{n} \\ {}^{q|c}\boldsymbol{V}_{el} \\ \dot{\boldsymbol{n}} \\ {}^{c}\dot{\boldsymbol{V}}_{el} \end{array} \right\}^{n} \,. \tag{3.67} $$

In this context, the panel normal vectors $\boldsymbol{n}$ and the elastic velocity $\boldsymbol{V}_{el}$ have already been presented with respect to the generalised coordinates and can be used in a similar way. While Eq. (3.62) can be directly applied to describe the panel normal vectors, the elastic velocity needs to be treated in more detail. It has already been pointed out, that the aerodynamic state-space model includes variables, which are specified exclusively at the quarter points or the collocation points of the aerodynamic panels. The reason for this is that the original vortex lattice method is based on the zero-normal-flow boundary condition enforced at the collocation points. This becomes particularly important in terms of the variables describing the dynamic response of the system. For example, considering a panel's collocation point located on the elastic axis of the wing while the wing is subject to a generic pitch motion, the velocity vectors of the collocation point and the corresponding quarter point will differ completely over time. Consequently, the interpolation matrix $\boldsymbol{M}$ in Eq. (3.64) must be chosen according to the location where the elastic velocities are evaluated. In contrast to the integration of the aerodynamic model, two additional input variables must be handled for the integration of the total aerodynamic forces into the structural model. The time derivative $\dot{\boldsymbol{n}}$ of the panel normal vectors is obtained similar to Eq. (3.62) using the modal approach with the generalised velocity $\boldsymbol{q}_2$. Accordingly, the elastic acceleration $\dot{\boldsymbol{V}}_{el}$ can be expressed in a similar way as the elastic velocity $\boldsymbol{V}_{el}$ by the generalised acceleration $\boldsymbol{q}_3$. Since this generalised coordinate is not provided by the structural

model, the acceleration $\dot{\boldsymbol{V}}_{el}$ can not be taken into account at this point. Using the given information the single sub-matrices of the direct term seen in Eq. (3.67) and the corresponding input variables can be expressed as follows:

$$ {}^{A}\boldsymbol{D}_1 \cdot \boldsymbol{n} = \left({}^{A}\boldsymbol{D}_{s,1} + {}^{A}\boldsymbol{D}_{u,1} \right) \cdot \frac{\partial \boldsymbol{n}}{\partial \boldsymbol{\Phi}} \cdot \boldsymbol{q}_1 \ , \tag{3.68a} $$

$$ {}^{A}\boldsymbol{D}_2 \cdot {}^{q|c}\boldsymbol{V}_{el} = \left({}^{A,q}\boldsymbol{D}_{s,2} \cdot \boldsymbol{M}_{qp} + \left({}^{A,c}\boldsymbol{D}_{s,2} + {}^{A,c}\boldsymbol{D}_{u,2} \right) \cdot \boldsymbol{M}_{cp} \right) \cdot \boldsymbol{H}_d \cdot \boldsymbol{\Phi} \cdot \boldsymbol{q}_2 \ , \tag{3.68b} $$

$$ {}^{A}\boldsymbol{D}_3 \cdot \dot{\boldsymbol{n}} = {}^{A}\boldsymbol{D}_{u,3} \cdot \frac{\partial \boldsymbol{n}}{\partial \boldsymbol{\Phi}} \cdot \boldsymbol{q}_2 \ , \tag{3.68c} $$

$$ {}^{A}\boldsymbol{D}_4 \cdot {}^{c}\dot{\boldsymbol{V}}_{el} = {}^{A,c}\boldsymbol{D}_{u,4} \cdot \boldsymbol{M}_{cp} \cdot \boldsymbol{H}_d \cdot \boldsymbol{\Phi} \cdot \boldsymbol{q}_3 \ . \tag{3.68d} $$

By means of these relations, the aerodynamic forces are defined as functions of the structural states and are introduced into the structural state-space system. Subsequently, Eq. (3.61) can be written as

$$ \begin{Bmatrix} \boldsymbol{q}_1 \\ \boldsymbol{q}_2 \end{Bmatrix}^{n+1} = \begin{bmatrix} \boldsymbol{A}_{21} & \boldsymbol{A}_{22} & \boldsymbol{A}_{23} \\ \boldsymbol{A}_{31} & \boldsymbol{A}_{32} & \boldsymbol{A}_{33} \end{bmatrix} \cdot \begin{Bmatrix} \boldsymbol{\Gamma}_w \\ \boldsymbol{q}_1 \\ \boldsymbol{q}_2 \end{Bmatrix}^{n} \ . \tag{3.69} $$

Again, the system's dependence is reduced to a linear combination of the aerodynamic and structural states using a dynamics matrix, whose sub-matrices are calculated by

$$ \begin{bmatrix} \boldsymbol{A}_{21} \\ \boldsymbol{A}_{31} \end{bmatrix} = \left[{}^{S}\bar{\boldsymbol{B}} \cdot {\boldsymbol{H}_f}^{T} \cdot {}^{A}\boldsymbol{C} \right] \in \mathbb{R}^{2n_m \times n_w} \ , \tag{3.70a} $$

$$ \begin{bmatrix} \boldsymbol{A}_{22} \\ \boldsymbol{A}_{32} \end{bmatrix} = \left[{}^{S}\bar{\boldsymbol{A}} + {}^{S}\bar{\boldsymbol{B}} \cdot {\boldsymbol{H}_f}^{T} \cdot \left({}^{A}\boldsymbol{D}_{s,1} + {}^{A}\boldsymbol{D}_{u,1} \right) \cdot \frac{\partial \boldsymbol{n}}{\partial \boldsymbol{\Phi}} \right] \in \mathbb{R}^{2n_m \times n_m} \ , \tag{3.70b} $$

$$ \begin{bmatrix} \boldsymbol{A}_{23} \\ \boldsymbol{A}_{33} \end{bmatrix} = \left[{}^{S}\bar{\boldsymbol{A}} + {}^{S}\bar{\boldsymbol{B}} \cdot {\boldsymbol{H}_f}^{T} \cdot \left({}^{A,q}\boldsymbol{D}_{s,2} \cdot \boldsymbol{M}_{qp} + \left({}^{A,c}\boldsymbol{D}_{s,2} + {}^{A,c}\boldsymbol{D}_{u,2} \right) \cdot \boldsymbol{M}_{cp} \right) \cdot \boldsymbol{H}_d \cdot \boldsymbol{\Phi} + {}^{A}\boldsymbol{D}_{u,3} \cdot \frac{\partial \boldsymbol{n}}{\partial \boldsymbol{\Phi}} \right] \in \mathbb{R}^{2n_m \times n_m} \ . \tag{3.70c} $$

It has to be noted that the matrices ${}^{S}\bar{\boldsymbol{A}}$ and ${}^{S}\bar{\boldsymbol{B}}$ in discrete-time formulation still have the same dimensions as the corresponding continuous-time matrices, which are $2n_m \times 2n_m$ and $2n_m \times 3n_{fe}$. To obtain two sub-matrices from each equation the resulting right-

hand side matrices are halved in the first dimension. The upper half is assigned to matrix $\boldsymbol{A}_{2x}$ and the lower half to matrix $\boldsymbol{A}_{3x}$, where both matrices have the dimension $n_m \times n_m$. As both the aerodynamic and structural model are related to the same state vector, Eqs. (3.65) and (3.69) can be finally merged to build a linear, discrete-time state-space model for the entire aeroelastic system:

$$\begin{Bmatrix} \boldsymbol{\Gamma}_w \\ \boldsymbol{q}_1 \\ \boldsymbol{q}_2 \end{Bmatrix}^{n+1} = \begin{bmatrix} \boldsymbol{A}_{11} & \boldsymbol{A}_{12} & \boldsymbol{A}_{13} \\ \boldsymbol{A}_{21} & \boldsymbol{A}_{22} & \boldsymbol{A}_{23} \\ \boldsymbol{A}_{31} & \boldsymbol{A}_{32} & \boldsymbol{A}_{33} \end{bmatrix} \cdot \begin{Bmatrix} \boldsymbol{\Gamma}_w \\ \boldsymbol{q}_1 \\ \boldsymbol{q}_2 \end{Bmatrix}^{n} . \tag{3.71}$$

Using this equation it is possible to describe the aeroelastic behaviour of a highly flexible wing at any deformed state of steady aeroelastic equilibrium. Here, the discrete-time formulation is favourable in terms of verification as it allows for time-marching and straightforward comparison with reference results from solvers in the time domain. Nevertheless, during the verification of the aeroelastic model it appeared that neglecting the elastic acceleration $\dot{\boldsymbol{V}}_{el}$ leads to a significant decrease in unsteady forces, cf. Section 4.1.2. As this is expected to affect the stability of the system, the integration of the acceleration term seems mandatory for correct aeroelastic modelling. Therefore, a method for approximating the elastic acceleration of the wing will be derived in the following. Regarding the integration of aerodynamic forces, it has been shown that $\dot{\boldsymbol{V}}_{el}$ can be expressed by the modal approach as a function of the generalised acceleration $\boldsymbol{q}_{3,}$, see Eq. (3.68d). Although this generalised coordinate is not part of the structural state vector, it can be approximated from the generalised velocity $\boldsymbol{q}_2$ using a finite difference approach. This method seems to be sufficient since it has already been used for the time derivative of the circulation in the original unsteady vortex lattice implementation. Accordingly, the first-order forward scheme in Eq. (3.42) established during the derivation of the aerodynamic state-space model is applied and leads to

$$\boldsymbol{q}_3^{n+1} \approx \frac{\boldsymbol{q}_2^{n+1} - \boldsymbol{q}_2^{n}}{\Delta t} , \tag{3.72}$$

which represents a first-order backward scheme to account for the state-space formulation of $\boldsymbol{q}_3$ at the next time step. Both components of this equation are included in the aeroelastic state-space model and can be easily expressed by the lowest line of Eq. (3.71). Thus, the generalised acceleration $\boldsymbol{q}_3$ is added to the state vector of the

system, which is then defined by

$$\begin{Bmatrix} \boldsymbol{\Gamma}_w \\ \boldsymbol{q}_1 \\ \boldsymbol{q}_2 \\ \boldsymbol{q}_3 \end{Bmatrix}^{n+1} = \begin{bmatrix} \boldsymbol{A}_{11} & \boldsymbol{A}_{12} & \boldsymbol{A}_{13} & \boldsymbol{A}_{14} \\ \boldsymbol{A}_{21} & \boldsymbol{A}_{22} & \boldsymbol{A}_{23} & \boldsymbol{A}_{24} \\ \boldsymbol{A}_{31} & \boldsymbol{A}_{32} & \boldsymbol{A}_{33} & \boldsymbol{A}_{34} \\ \boldsymbol{A}_{41} & \boldsymbol{A}_{42} & \boldsymbol{A}_{43} & \boldsymbol{A}_{44} \end{bmatrix} \cdot \begin{Bmatrix} \boldsymbol{\Gamma}_w \\ \boldsymbol{q}_1 \\ \boldsymbol{q}_2 \\ \boldsymbol{q}_3 \end{Bmatrix}^{n} . \tag{3.73}$$

The sub-matrices used to determine the new state are

$$\boldsymbol{A}_{41} = \left[\frac{\boldsymbol{A}_{31}}{\Delta t} \right] \in \mathbb{R}^{n_m \times n_w} , \tag{3.74a}$$

$$\boldsymbol{A}_{42} = \left[\frac{\boldsymbol{A}_{32}}{\Delta t} \right] \in \mathbb{R}^{n_m \times n_m} , \tag{3.74b}$$

$$\boldsymbol{A}_{43} = \left[\frac{\boldsymbol{A}_{33} - \boldsymbol{I}}{\Delta t} \right] \in \mathbb{R}^{n_m \times n_m} , \tag{3.74c}$$

$$\boldsymbol{A}_{44} = \left[\boldsymbol{0} \right] \in \mathbb{R}^{n_m \times n_m} , \tag{3.74d}$$

which means that the acceleration only depends on the original three states of the aeroelastic system. In addition, the influence of the acceleration on these original states is specified by the sub-matrices

$$\boldsymbol{A}_{14} = \left[\boldsymbol{0} \right] , \tag{3.75a}$$

$$\begin{bmatrix} \boldsymbol{A}_{24} \\ \boldsymbol{A}_{34} \end{bmatrix} = \left[{}^{S}\bar{\boldsymbol{B}} \cdot \boldsymbol{H}_f{}^{T} \cdot {}^{A,c}\boldsymbol{D}_{u,4} \cdot \boldsymbol{M}_{cp} \cdot \boldsymbol{H}_d \cdot \boldsymbol{\Phi} \right] , \tag{3.75b}$$

where $\boldsymbol{A}_{24}$ and $\boldsymbol{A}_{34}$ represent the former neglected acceleration term in Eq. (3.68d). This completes the integration of the aerodynamic and structural model and the linearisation of the aeroelastic system.

As mentioned before, the monolithic discrete-time state-space model in Eq. (3.73) can be used in a time-stepping procedure to compute the dynamic response of the system to small disturbances, e.g. by an initial deflection of one of the modes in the generalised coordinate $\boldsymbol{q}_1$. This method is used for the verification of the aerodynamic and aeroelastic state-space model. It should be noted that the steady aeroelastic equilibrium is assumed as the initial condition for the state-space model, i.e. onflow velocity and angle of attack are constant, the wing is at rest in a constant deformed or undeformed shape and all state variables are set to zero. When time-marching

is used, the state vector as well as any outputs, such as aerodynamic forces, only represent the differences due to the dynamic response around this equilibrium. The aeroelastic stability in terms of flutter can be determined by an eigenvalue analysis of the dynamics matrix of the linearised state-space model, as shown in Section 3.2.1. In this particular case, the complex eigenvalues obtained appear in the discrete-time form z and the system is only stable if the magnitudes of all eigenvalues are smaller than one (eigenvalues located inside the unit circle in the complex z-plane). As this representation is not suitable for common illustration methods, such as root-locus or V-g and V-ω plots, the eigenvalues are converted into continuous-time form by [16]

$$\lambda_i = \frac{\log z_i}{\Delta t} \,. \tag{3.76}$$

Afterwards, the real parts of the eigenvalues represent the decay ratios and the imaginary parts represent the frequencies of the system's modes. Although each eigenvalue and its corresponding eigenvector are related to a specific degree of freedom or state of the system respectively, the allocation of eigenvalues and states is difficult. A problem in this context is the number of aerodynamic states, which is the number of all wake panels. This outweighs the number of structural states, which is three times the number of modes considered. In general, the number of states of a state-space system can be reduced using different methods of model order reduction. Due to the limited scope of this thesis, this has not been realised in the current implementation, but will be considered in the future.

Finally, the method for identification of the relevant eigenvalues is preferably described using the flowchart of the linearised static coupling solution sequence in Fig. 3.4. The preprocessing is similar to the static coupling solution sequence in Fig. 3.2, except that it is now possible to define a velocity range. When preprocessing is completed, the static coupling solution is performed until convergence of the structural deformation is achieved. Here, the structural solution using Nastran SOL400 is extended by a modal analysis on the preloaded structure following the nonlinear static analysis. The eigenvalues and eigenvectors obtained are later used to establish the modal matrices $\mathbf{\Omega}$ and $\mathbf{\Phi}$ for the state-space model. Due to the fact that a static coupling solution sequence based on a steady vortex lattice solution is used in combination with the state-space model derived from the unsteady vortex lattice method, the wake needs to be treated in a special way. Since the wake of the steady solution only consists of one row of long wake vortex rings, these are divided into a number of equal-length wake rows to obtain a wake similar to that of an unsteady solution. At this point it has to be mentioned that the unsteady VLM provides the most accurate results when the length of the wake panel rows equals the length of the bound

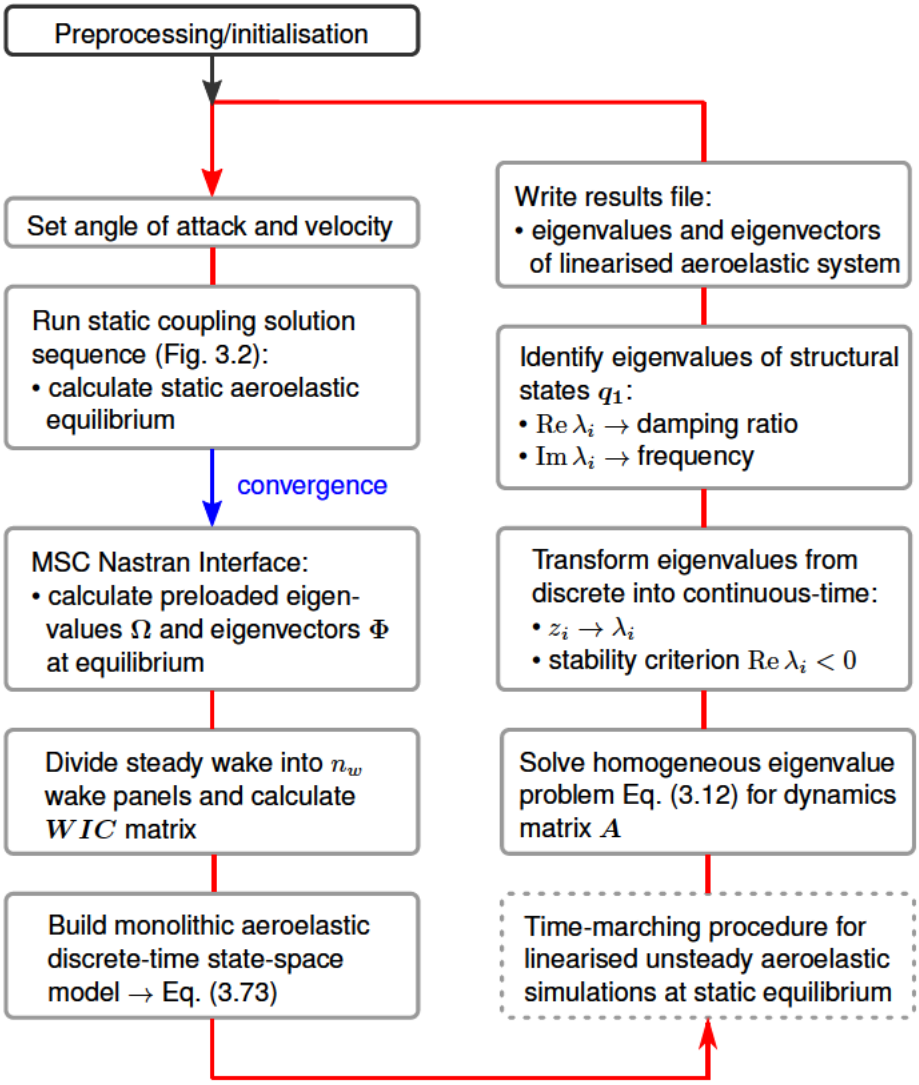

Figure 3.4: Linearised static coupling solution sequence including a time-marching procedure (optional) and the stability analysis

panel rows. Therefore, the routine automatically divides the wake into panels of length equal to the length of bound panels. After the steady wake is converted, the WIC matrix is evaluated and the state-space model is build. The time step size Δt, which needs to be defined for some matrices of the linearised model, is calculated from the onflow velocity and the bound or wake panel length respectively to ensure consistency with the unsteady VLM formulation. Following the eigenvalue analysis of the dynamics matrix, the eigenvalues are transformed into continuous-time formulation and sorted according to the lowest damping (high $\mathrm{Re}\,\lambda_i$). Finally, the sorted eigenvalues with the lowest damping are searched for frequencies ($\mathrm{Im}\,\lambda_i$) closest to a set of reference

frequencies. These reference frequencies are either the natural frequencies obtained from the structural modal analysis or the frequencies identified for the state-space system of the previous velocity. The identified eigenvalues and the corresponding eigenvectors are written into an output file and the solution sequence starts with the next velocity or angle of attack.

4 Numerical Simulations and Results

After the complete linearisation of the aeroelastic system has been presented in the preceding sections, this chapter will focus on the verification and validation of the proposed method. In the first section the verification of the linearised state-space models is presented, beginning with the linearised aerodynamic model using the already existing unsteady VL solver (see Section 3.1.1) in the time domain. Subsequently, the entire aeroelastic model is verified in a similar way using an geometrically nonlinear aeroelastic solver. The second part of this chapter will exclusively address the results of numerical simulations for the Pazy wing test case. Following a brief introduction to the key features of the wind tunnel model and the general simulation setup the results of the static coupling simulations for a number of different velocities and angles of attack are presented. These are performed with the solution sequence described in Section 3.1.2 and are compared to the results from Department of Aeronautics at Imperial College London, another member of the Large Deflection Working Group. A vital part of this thesis is the determination of the natural modes as a function of the deformation, which is discussed afterwards. For this purpose, a modal analysis of the preloaded structure at various aeroelastic equilibrium points, obtained from the static coupling simulations, is performed within Nastran SOL400. The goal here is to evaluate the influence of geometric nonlinearities due to large deformations on the structural properties, such as natural frequencies and mode shapes. This, in turn, affects the aeroelastic stability, which is computed using the proposed method for stability analysis and displayed in Section 4.2.4. The results are presented for velocity sweeps at different angles of attack and will also be compared to results from the Imperial College group. In addition, the method for stability analysis is validated for the undeformed wing (0 degrees angle of attack) using the aeroelastic flutter analysis SOL145 in Nastran.

4.1 Verification of the Linearisation

At this point, a short explanation of the difference between verification and validation will be given as these terms are often used interchangeably. According to Aerospace Recommended Practice ARP 4754 (Guidelines for Development of Civil Aircraft and Systems [33]), verification is the "evaluation of an implementation of requirements to determine that they have been met; confirms the organisation built the aircraft system/function/item correctly". On the other hand, validation is referred to as the "determination that the requirements for a product are correct and complete; confirms organisation is building the right aircraft system/function/item". Regarding the verification and validation of simulation models as developed in this thesis, a more accurate definition can be found in [34]. In this particular case, model verification describes the methods used to ensure that the implementation of a computational model works correctly. Consequently, the verification of the linear state-space models will be achieved by applying them to artificial test cases. The results are then compared to reference data obtained from validated simulation tools which, in contrast, account for the nonlinear effects. Nevertheless, the deviations should be small as long as the test cases chosen are of simple nature and do not incorporate large nonlinear effects. The purpose of model validation, instead, is to proof whether the model achieves a desired range of accuracy in its area of application [34]. To this end, the proposed method for stability analysis will be validated by comparing the results from the Pazy wing test case with results obtained from a commercial aeroelastic solver and with computational data provided by the Imperial College group.

4.1.1 Verification of the Aerodynamic Model using an Unsteady Vortex Lattice Solver in the Time Domain

Most of the linearisation of the aeroelastic system involves the derivation of a linearised aerodynamic model from the unsteady vortex lattice method. Thus, the verification of the aerodynamic state-space model presented in Section 3.2.2 is addressed first. In this thesis the general approach for verification is to use the developed discrete-time state-space models in a time-stepping procedure and to compare the results to those of existing solvers. For the particular case of the aerodynamic model, the reference results are obtained using the unsteady vortex lattice solver described in Section 3.1.1. In addition, this solver is also used to provide the inputs required for the linearised aerodynamic model, e.g. the AIC and WIC matrices or the panel normal vectors and

areas. This is favourable in terms of implementation as the time step size Δt, the (onflow) velocity $\boldsymbol{V}_{rb}$ and the grid metric of the wake gathered in the WIC matrix are automatically consistent between the unsteady vortex lattice solver and the linearised aerodynamic model. The aerodynamic grid used for the following simulations is based on the Pazy wing since it presents a very simple wing geometry with rectangular planform, no taper, no sweep and a symmetrical airfoil. The dimensions as well as several other characteristics of the wing design can be found in Section 4.2.1, but will not be relevant for the verification at first.

Regarding the aeroelastic state-space model it is important that the integrated aerodynamic model correctly models both steady and unsteady forces. The verification test case should therefore consider an unsteady flow field, where the steady and unsteady forces over time can be described by continuous functions. In this respect, an instantaneous change in angle of attack, as it has been discussed concerning the principals of unsteady aerodynamics (cf. Section 2.1.2), seems to be inappropriate due to the expected step response (jump discontinuity) of the lift forces. In case of the unsteady VL solver the step response would lead to artificially increased unsteady forces, since these are determined using a first-order backward differentiation scheme (cf. Eq. (3.4)). This effect could be observed during the verification of the linearised aeroelastic model in Section 4.1.2 and is depicted in Fig. 4.4. The linearised aerodynamic model, however, should provide correct results for this test case. A more suitable approach is represented by the oscillating airfoil, whose lift forces are illustrated in Fig. 2.4b. A modified method is chosen for the verification test case using a generic heave motion at zero degrees angle of attack instead of a pitch motion. This type of motion is usually not supported in the unsteady aerodynamic solver, but can easily be realised by adding a (harmonic) vertical velocity component ΔV_z to the onflow velocity vector $\boldsymbol{V}_{rb}$, which leads to

$$\boldsymbol{V}_{rb} = \begin{Bmatrix} V_\infty \cdot \cos\alpha \\ 0 \\ V_\infty \cdot \sin\alpha + \Delta V_z \end{Bmatrix} , \tag{4.1}$$

$$\text{with} \qquad \Delta V_z = \hat{V} \cdot \sin\left(2\pi \cdot f \cdot t\right) \ . \tag{4.2}$$

As can be seen, the additional velocity component is described as a harmonic function of time with the amplitude $\hat{V}$ and the frequency f. With respect to the linearised aerodynamic model represented by Eqs. (3.28), (3.39) and (3.52) it is necessary to define the variables of the input vector, which are the panel normal vectors and the

elastic velocity as well as their first time derivatives. Assuming a generic heave motion it is obvious that the normal vectors $\boldsymbol{n}$ do not change over time and can be taken directly from the unsteady aerodynamic solver. Accordingly, the time derivative $\dot{\boldsymbol{n}}$ is set to zero. Since the elastic motion of the wing is completely defined by Eq. (4.2), the elastic velocity $\boldsymbol{V}_{el}$ has only a z component ΔV_z. Its time derivative $\dot{\boldsymbol{V}}_{el}$ can be easily found by an analytical derivation of Eq. (4.2). The input vector of the verification test case finally includes:

$$\boldsymbol{n} = \begin{Bmatrix} 0 \\ 0 \\ 1 \end{Bmatrix} , \quad \boldsymbol{V}_{el} = \begin{Bmatrix} 0 \\ 0 \\ \Delta V_z \end{Bmatrix} , \quad \dot{\boldsymbol{n}} = \begin{Bmatrix} 0 \\ 0 \\ 0 \end{Bmatrix} , \quad \dot{\boldsymbol{V}}_{el} = \begin{Bmatrix} 0 \\ 0 \\ \Delta \dot{V}_z \end{Bmatrix} , \tag{4.3}$$

$$\text{with} \qquad \Delta \dot{V}_z = \hat{V} \cdot 2\pi \cdot f \cdot \cos\left(2\pi \cdot f \cdot t\right) , \tag{4.4}$$

with the wing being considered in its undeformed shape at zero degrees angle of attack. The WIC matrix and the wake circulations used for the state-space model are determined from unsteady simulations without the elastic motion to obtain an undeformed wake and an initial state vector $\boldsymbol{\Gamma}_w^0 = \boldsymbol{0}$.

Using the described test case, the simulations for verification of the linearised aerodynamic model are performed for a range of different onflow velocities V_∞, amplitudes $\hat{V}$ and reduced frequencies k. Furthermore, different discretisations of the aerodynamic grid are applied. The reduced frequency is used here as it is a more significant parameter in terms of unsteady aerodynamics. In this case the required frequency f can be calculated for any given k and V_∞ with Eq. (2.6). The results from the unsteady aerodynamic solver and the linearised state-space model for two different reduced frequencies are depicted in Fig. 4.1. For the sake of simplicity, the evolution of the total steady and total unsteady forces in the z direction is compared over time. As it can be seen, the steady and unsteady lift forces from both solvers are almost coincident for each reduced frequency. Small differences appear at the maximum amplitudes of the unsteady forces, which are possibly due to the terms neglected during the linearisation. Overall, the maximum deviations in the unsteady forces are in the range below 1%, while the steady forces obtained from both solvers are exactly the same. This seems comprehensible since the neglected terms of the steady forces only represent components in the flow or x direction respectively. Since simulations for velocities up to 40 m/s and amplitudes of 5 m/s lead to similar results with deviations smaller than 1% the verification of the linear aerodynamic state-space model is completed.

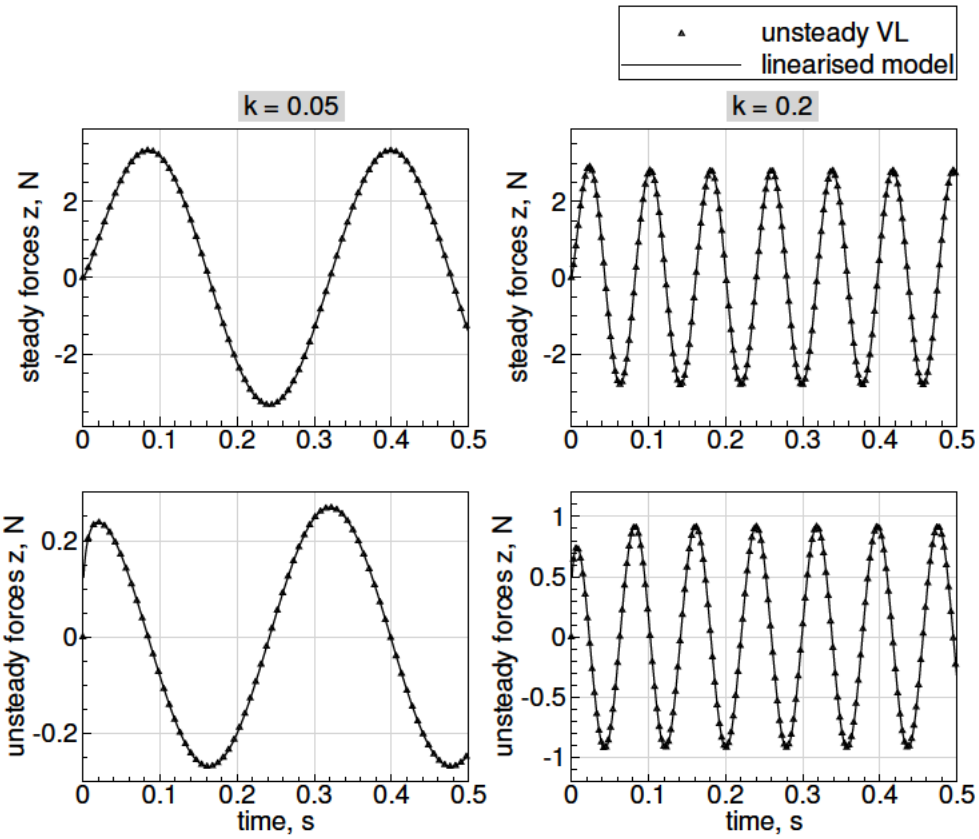

Figure 4.1: Comparison of forces obtained by unsteady aerodynamic solver and linear state-space model for a generic heave motion with V_∞ = 20 m/s and $\hat{V}$ = 1 m/s (cf. Eqs. (4.1) to (4.4))

4.1.2 Verification of the Aeroelastic Model using a Nonlinear Modal Solver

The verification of the linear aeroelastic state-space model is carried out by using an aeroelastic modal solver in the time domain. A comprehensive description of this nonlinear solver based on an extended modal approach can be found in [8]. Similar to the aerodynamic model the linearised discrete-time aeroelastic model is used for time-marching. In this particular case, the state-space model does not contain any inputs. It depends solely on the dynamics matrix and the system's states (cf. Eq. (3.73)), whereas the structural deformation affects the aerodynamic forces and vice versa. Therefore, a test case investigating the unrestricted dynamic behaviour of the wing in a constant flow field seems to be more suitable for verification than the 'forced motion' used in the previous section. This 'free vibration' due to small disturbances is realised by a small initial deformation of the wing, which can be achieved by setting an initial

value for the generalised coordinate $\boldsymbol{q}_1$. The general setup of the simulation is similar to the setup used for the aerodynamic model, i.e. constant onflow velocity and zero degrees angle of attack. Using an angle of attack $AoA \neq 0$ would lead to a greater effort when comparing the results since the linearised model only considers forces and deformations around the deformed state in static equilibrium, whereas the results of the nonlinear modal solver are always related to the undeformed state ($AoA = 0$). For the modal solver, an additional input file containing the eigenvalues and eigenvectors of the system is required. These can be obtained from the linearised static coupling solution sequence, as they are also needed in the modal matrices $\boldsymbol{\Omega}$ and $\boldsymbol{\Phi}$ to establish the structural part of the state-space model (see Eq. (3.60)). However, the verification is firstly performed for simple test cases rather than for the real structural model. To this end, three generic structural models with increasing complexity are generated. Two of these are systems with a single DOF for heave and pitch respectively, representing the wing attached to either a tension spring or a torsional spring. The third is a two DOFs system and a combination of both single DOF systems. Again, the oscillatory characteristics of the systems are to be defined using the reduced frequency. Hence, the eigenfrequencies must be recalculated from the predefined reduced frequency and onflow velocity for each system and test case. In contrast, the eigenvectors of each system have to be determined only once, whereas the eigenvectors of the pitch DOF system are related to an elastic axis at 50% chord.

The simulations are performed for each model with two different reduced frequencies $k = 0.05$ and $k = 0.1$. A comparison of the forces for the system with the DOF heave is shown in Fig. 4.2. The onflow velocity is 20 m/s, the reduced frequency is 0.1 and the initial generalised coordinate is set to 0.01 which results in an initial displacement of 0.01 m from the equilibrium position. In this case, two different solutions have been obtained from the linearised aeroelastic state-space model. One is computed using the original formulation in Eq. (3.71) while the other is computed with the enhanced model considering the acceleration term in the unsteady forces (cf. Eq. (3.73)). As can be seen, the steady forces between the nonlinear and the linear solution are completely coincident. Regarding the unsteady forces, the results of the model neglecting the acceleration term show significantly lower amplitudes with a decrease of up to 47% with respect to the results obtained from the nonlinear modal solver. On the other hand, the results of the modified model approximating the acceleration with a finite differences approach are in very good agreement with maximum deviations below 1%. It can be concluded that the chosen method is sufficient for the approximation of the elastic acceleration and the resulting unsteady forces. Furthermore, taking into account the acceleration term seems

mandatory, since it accounts for almost half of the unsteady forces. Generally, these forces are out-of-phase while the steady forces are in phase with the motion of the wing leading to a phase shift between the total aerodynamic forces and the wing vibration. The acceleration term consequently does not have a great effect on the amplitude of the total forces, but mainly on the phase shift. This is expected to have an influence on the dynamic behaviour, especially as the contribution of the unsteady forces increases with increasing reduced frequency. Thus, the neglect of the elastic acceleration might finally lead to deviations in the stability analysis of the wing, which should be investigated in the future.

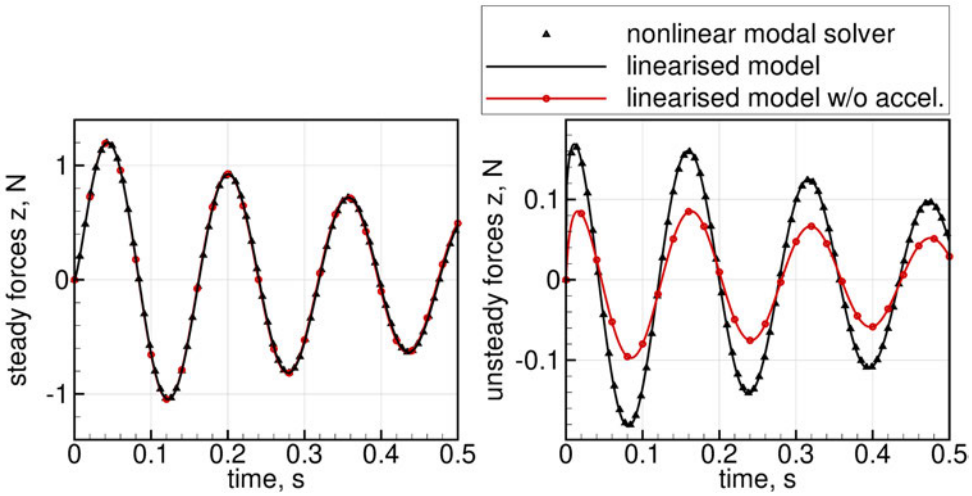

Figure 4.2: Comparison of forces obtained by nonlinear modal solver and linear aeroelastic state-space model for a single DOF (heave) system with V_∞ = 20 m/s, $q^0_{1,i}$ = 0.01 and k = 0.1

In addition to the single DOF heave model, the results of the generic two DOFs model are depicted in Fig. 4.3. The results from the linearised solution are now obtained only from the enhanced model and are also almost coincident with the nonlinear solution. Apart from the aerodynamic forces, the development of the generalised coordinates over time is also illustrated with $q_{1,1}$ representing the heave and $q_{1,2}$ the pitch DOF of the wing. For this particular case, the predefined reduced frequency is 0.1 (with respect to the heave motion) and the frequency ratio between pitch and heave is ω_p/ω_h = 2.0. While the heave motion is noticeably damped, the amplitude of the pitch motion remains constant due to the position of the elastic axis at 50% chord. Similar to the forces no deviations can be observed here between the nonlinear and linear solution. Finally, the results of the verification test case for the real structural model are presented in Fig. 4.4. For simplification, only the lowest four natural modes are taken into account which are the first ($q_{1,1}$), second ($q_{1,2}$) and third ($q_{1,4}$) out-

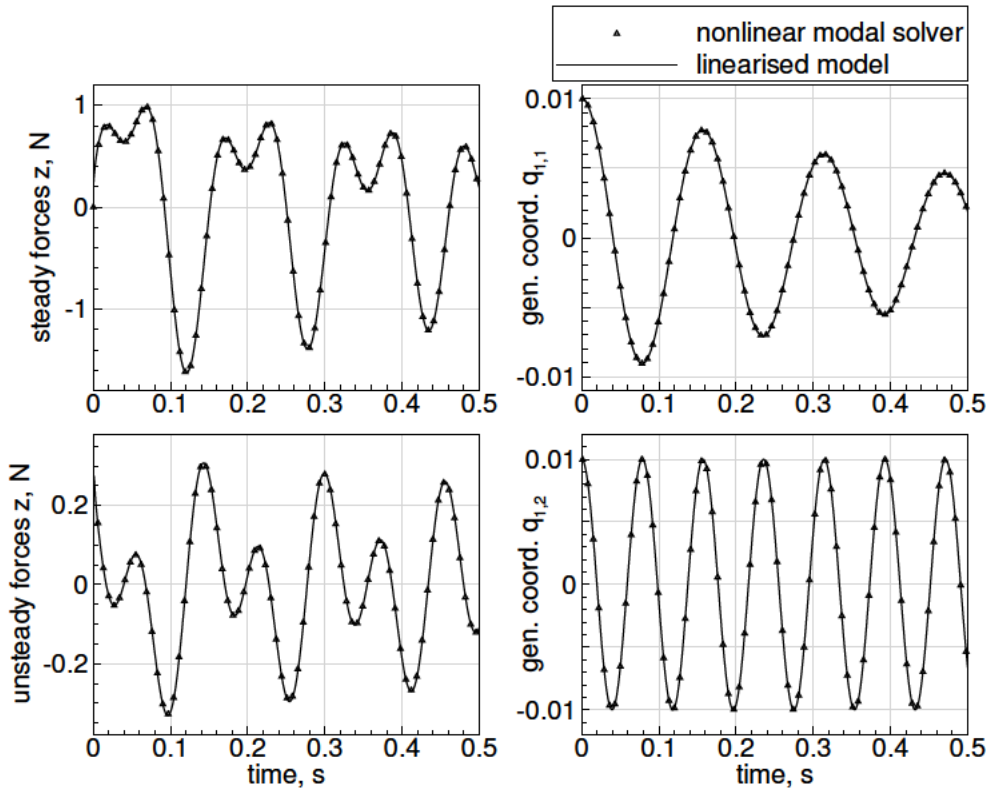

Figure 4.3: Comparison of results obtained by nonlinear modal solver and linear aeroelastic state-space model for a two DOFs system with V_∞ = 20 m/s, q_1^0 = 0.01 and k = 0.1 (w.r.t. heave)

of-plane bending mode as well as the first torsion mode ($q_{1,3}$). A more detailed overview of the mode shapes and eigenfrequencies is provided in Section 4.2.3. As the eigenvectors computed by Nastran SOL400 are normalised to unit value of the generalised mass, the initial value for the generalised coordinates is reduced to 0.001 to ensure that the initial deformation is very small and in a linear regime. For this case, the results are no longer coincident but agree very well for the three bending modes. Considerable differences appear in the evolution of the first out-of-plane bending DOF ($q_{1,1}$). However, since these differences occur mainly at the beginning of the simulation, they may be caused by an issue regarding the unsteady forces in the modal solver. These are determined using a first order backward scheme, which results in significantly larger forces for the first time step (factor 3 in this case). Other reasons might be the force terms neglected during the linearisation and, of course, the fact of comparing the solution of a linear state-space model to a fully nonlinear modal solver also accounting for geometric nonlinearities. Overall, the deviations in the generalised coordinates representing the structural behaviour and in the forces

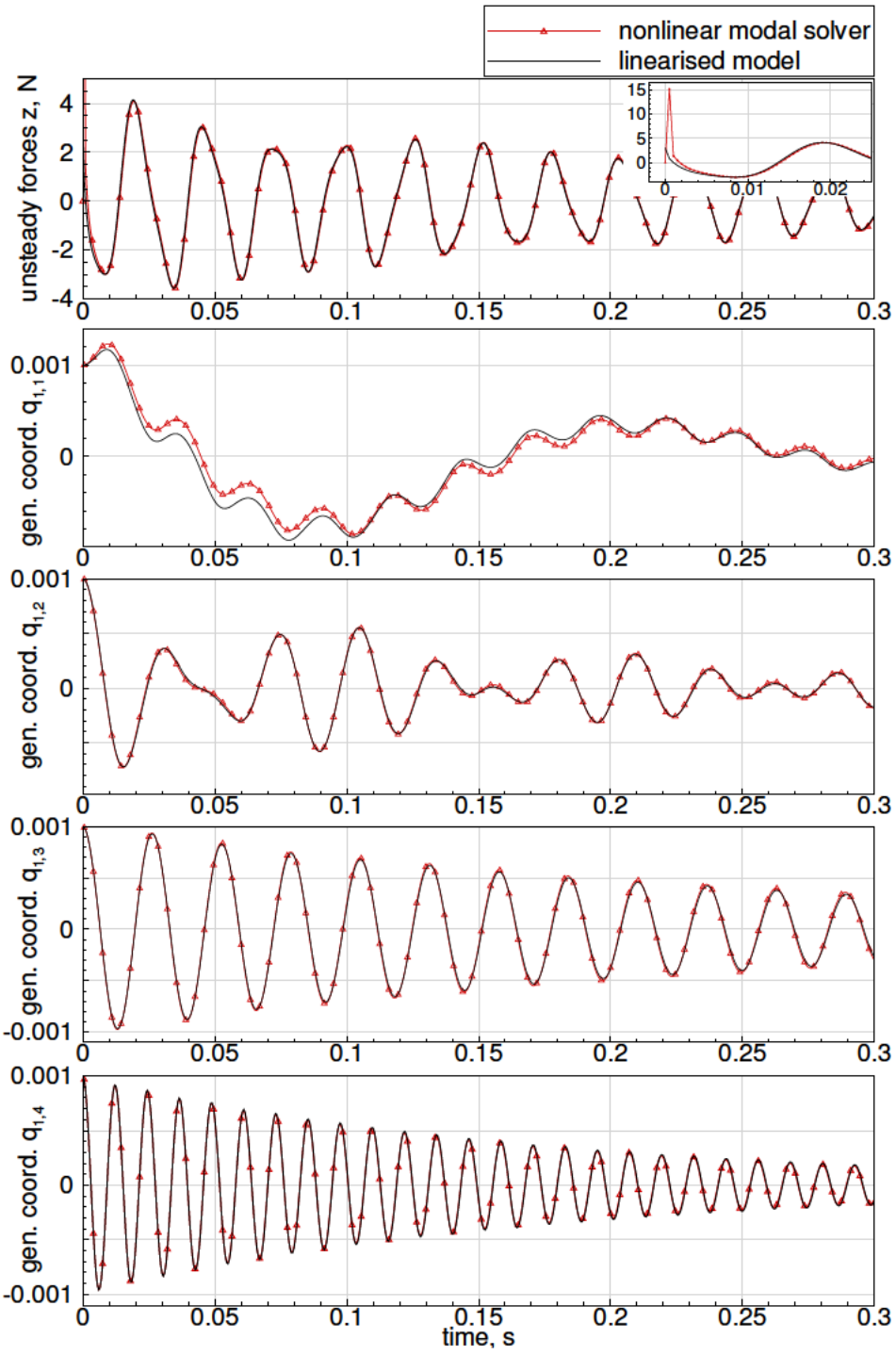

Figure 4.4: Comparison of results obtained by nonlinear modal solver and linear aeroelastic state-space model for Pazy wing full model with V_∞ = 40 m/s, $q^0_{1,i}$ = 0.001

representing the aerodynamic behaviour are regarded as small. Thus, the verification of the linear aeroelastic state-space model is accomplished and the proposed method can now be applied to the Pazy wing test case.

4.2 Pazy Wing Test Case

In this section, the existing solver, which has been extended with a method for stability analysis during this thesis, is used to perform an aeroelastic analysis of the highly flexible Pazy wing. Therefore, several aspects of the design of the Pazy wing wind tunnel model and the corresponding FE model will be discussed in the following section. The results of the static coupling simulations are presented afterwards in Section 4.2.2. This is followed by a presentation of the eigenfrequencies of the wing with respect to the deformation, which will be used to determine the influence of structural nonlinearities on the aeroelastic stability. This is investigated in Section 4.2.4 in terms of flutter by applying the method previously developed in Section 3.2. The validation of the results and the implemented methods are described in Sections 4.2.5 and 4.2.6.

4.2.1 Key Features of the Pazy Wing Aeroelastic Benchmark

The Pazy wing aeroelastic benchmark was developed at Technion in Israel in 2019. It was primarily designed to undergo very large deformations of up to 50% with respect to the wing span in wind-tunnel tests since measured data for comparable experimental studies are still very limited. The experimental results are intended to be used for validation of nonlinear structural models and different aeroelastic simulation tools. Two different models were build, whereas two ribs were added at the wing root of the second model. While the design has not been changed for the most part, both models slightly differ in terms of their natural frequencies. Unfortunately, the first model, called Pre-Pazy wing, was destroyed early during a wind-tunnel test campaign, so experimental data are only available for the second model. The simulations in this thesis, however, are performed exclusively for the Pre-Pazy wing, as the FE model for the second wing was not yet available at the beginning of these studies.

The wing, shown in Fig. 4.5, has a span of 550 mm and a chord length of 100 mm with a symmetric NACA 0018 airfoil. To simplify the modelling for computational methods and comparison of the results the geometry is very generic and consists of

Figure 4.5: The Pazy wing wind tunnel model [6]

Table 4.1: Properties of the Pazy wing [6]

Property	Measurement
Span	550 mm
Chord	100 mm
Area	0.055 m^2
Main spar	550×60×2.5 mm
Aspect Ratio	5.5
Airfoil	NACA 0018
Mass	0.321 kg

a rectangular planform without sweep, taper and dihedral. It is assembled from an Aluminum 7075 spar of 550 mm length, 60 mm width and 2.5 mm thickness, and a PA2200, 3D printed rib structure. This is covered by an Oralight polyester film mainly used for radio-controlled aircraft. It is applied by ironing and shrinks once the heat source is removed which results in a prestressing of the foil. This approach is chosen to ensure a smooth surface of the closed profile around the wing and to prevent

buckling even at states of large deformations. The wing-tip rod is part of the 3D printed chassis and can be used for attaching weights to modify the structural characteristics and thus the dynamic behaviour and the flutter speed. Important aerodynamic and geometrical properties of the Pazy wing are listed in Table 4.1 [6, 35].

The Nastran FE model, as illustrated in Fig. 4.6, was converted from an Ansys Workbench FE model and provided by Technion. The leading edge, trailing edge and the tip rod are exclusively modelled by beam elements (CBEAM), while the ribs are composed of a combination of beam and shell elements (CQUAD4, CTRIA3). On the other hand, the main spar and the skin consist of only shell elements. However, the shell elements do not account for the prestressing of the skin, which causes buckling and convergence issues in nonlinear structural analyses even at very low loadings. Therefore, the simulations in this thesis are performed for a modified model, where the shell elements representing the skin have been removed. There are different possibilities to include or model the influence of the skin, which have not yet been

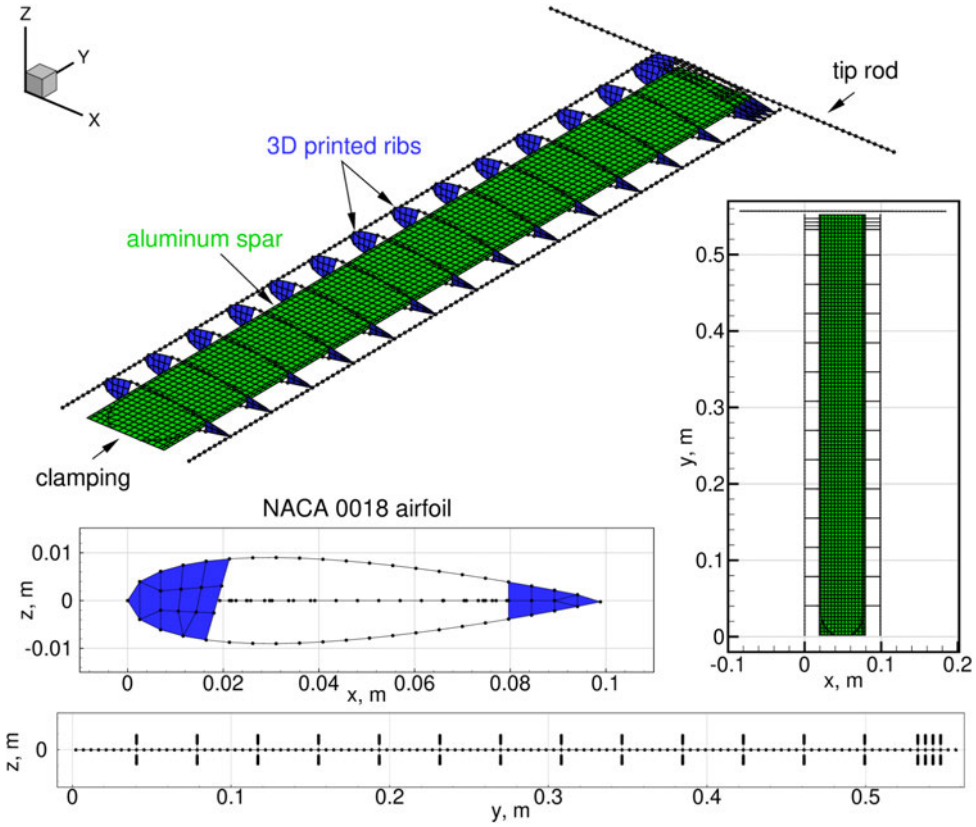

Figure 4.6: Nastran FE model of the Pazy wing composed by beam and shell elements representing the main aluminum spar and the 3D printed chassis; model without Oralight skin

implemented but will be pursued in the future. The clamping at the wing root is modelled perfectly rigid by using single point constraints (SPC1) for all translational and rotational DOFs. Regarding the coupling interface between the FE and the VL grid described in Section 3.1.2, a set of structural nodes must be defined for the transfer of forces and the interpolation of deformations. In this particular case, the 952 nodes selected include the nodes of the outer ribs, the leading and the trailing edge. These coupling nodes and the VL grid are depicted in Fig. 4.7 and show a good match, which is important for a correct data exchange between both models.

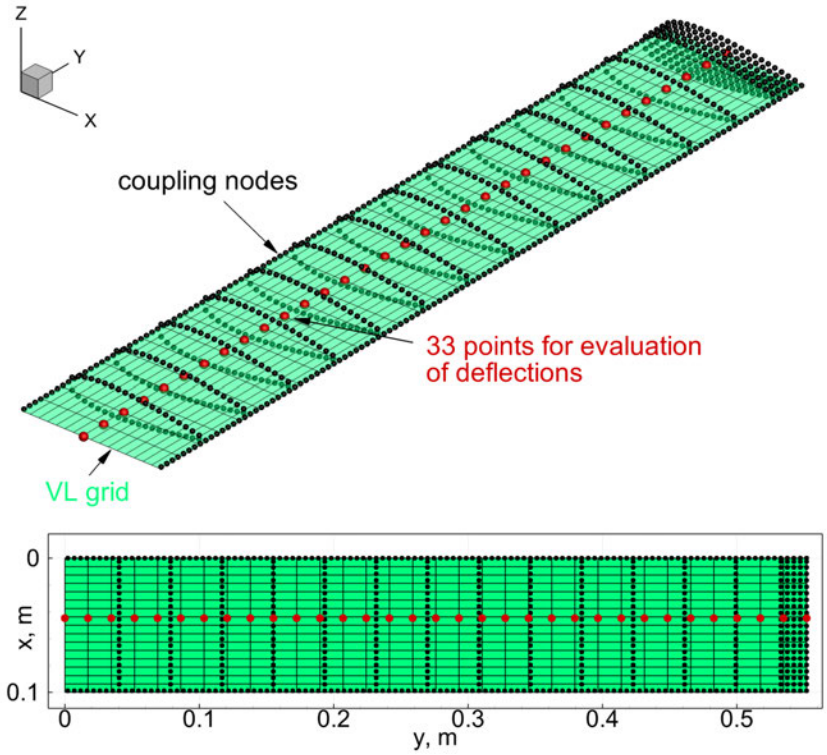

Figure 4.7: VL grid, coupling nodes of the FE model selected for the transfer of forces/displacements and 33 equidistant points used for the evaluation of deflections

4.2.2 Static Coupling Simulations

The results presented in this section were computed using the static coupling solution sequence described in Section 3.1.2. Since the results are to be compared to simulation results from the Imperial College group, the setup of the aerodynamic solver is based mainly on the setup of this group to achieve the best possible comparability.

The density is set to 1.225 kg/m^3 at mean sea level. For the steady VL solution the wing is discretised with 16 chordwise and 32 spanwise equidistant panels. As already mentioned, the wake only consists of a single row of lengthy vortex rings whose length is set to 2000 m in order to minimise the influence of the starting vortex. Although the wing is fixed vertically in the wind tunnel test, the direction of gravity is assumed along the negative z direction. Regarding the nonlinear static analysis using Nastran SOL400, the number of load increments is set to 40, while the *AUTO* option was chosen for the stiffness update strategy. In this case, the most efficient strategy is automatically selected by the programme, based on convergences rates [32]. Furthermore, the maximum number of iterations for each load increment is limited to 50. The structural residual required as a convergence criterion for the static coupling solver is defined to be $5 \cdot 10^{-4}$. The reason for this is that lower values lead to convergence issues especially at large structural deformations. A summary of important parameters of the static coupling simulation setup is shown in Table 4.2.

Table 4.2: Parameters of the static coupling simulation setup [6]

Angle of attack	1° - 10°
Free stream velocity	30,40,50 m/s
Density	1.225 kg/m^3
Chordwise panels	16
Spanwise panels	32
Wake length	2000 m
Gravity	on (z direction)
Structural residual	$5 \cdot 10^{-4}$

The simulations are performed for velocities of 30, 40 and 50 m/s and angles of attack ranging from 1 to 10 degrees. Although the wind tunnel tests are also performed with lower flow velocities, these conditions have been chosen to consider the effects of geometric nonlinearities. The results of the structural deformations at 30 m/s onflow velocity are shown in Fig. 4.8, where the normalised out-of-plane deflection Δz with respect to the wing span is plotted over the normalised spanwise coordinate y/b. For simplification of further comparisons, the deformations are evaluated at 33 equidistant points in spanwise direction, which are located at 44.75% chord (see Fig. 4.7). This is the case since the aeroelastic solver used by the Imperial College

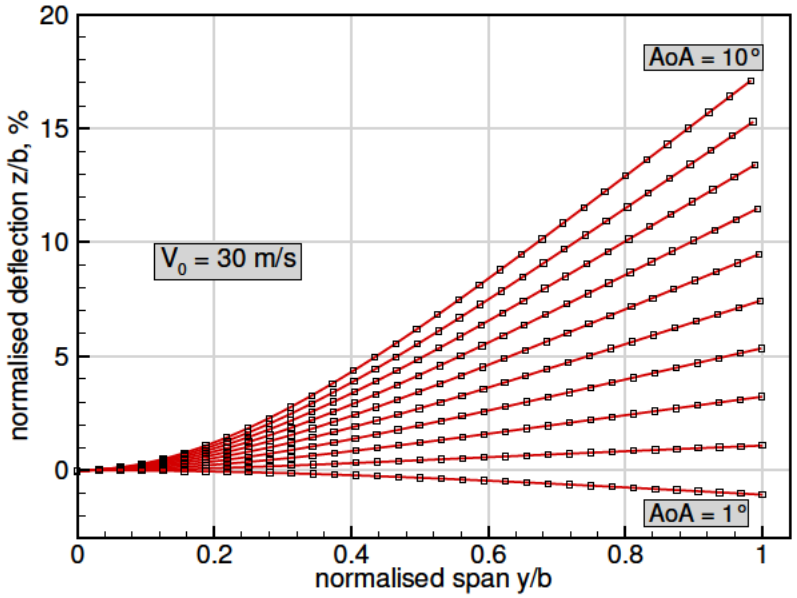

Figure 4.8: Results of static coupling simulations for 30 m/s onflow velocity evaluated at 44.75% chord

group is based on geometrically exact beam theories. The beam is placed at the elastic axis that was determined at this exact chordwise position. For an angle of attack of 1 degree the wing exhibits negative deformation due to the gravity forces outweighing the aerodynamic lifting loads. From 2 degrees of angle of attack on, the deformations become positive and - as expected - increase with each increment in angle of attack. The maximum wing tip displacement in the z direction of approximately 17% is obviously achieved at 10 degrees angle of attack. The influence of geometric nonlinearities can be roughly estimated from the tip displacement in the spanwise (y) direction. In this case, the influences seem to be rather small, as the maximum spanwise displacement is approximately 2% with respect to the span of the wing. It can also be seen that the curvature due to bending mainly occurs between the clamping and about 40% span, while the remaining part of the outer wing shows only minor local out-of-plane bending deformations.

The results for the medium onflow velocity of 40 m/s are depicted in Fig. 4.9. Here the lift forces are already greater than the gravity forces at 1 degree angle of attack (AoA), as indicated by the positive deformations. The maximum tip displacement of 17% for the 30 m/s case is now reached at 5 degrees AoA, while the values exhibit approximately 32% at the highest AoA. Thus, the deformations apparently are in a nonlinear regime, which is also indicated by a displacement of 6% in the y direction. While a linear solution at velocities below 30 m/s may only lead to small deviations, it

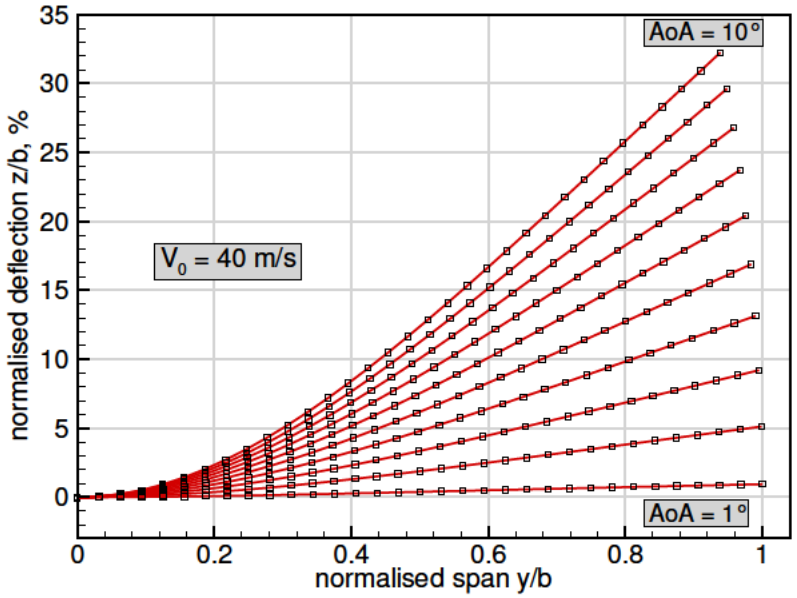

Figure 4.9: Results of static coupling simulations for 40 m/s onflow velocity evaluated at 44.75% chord

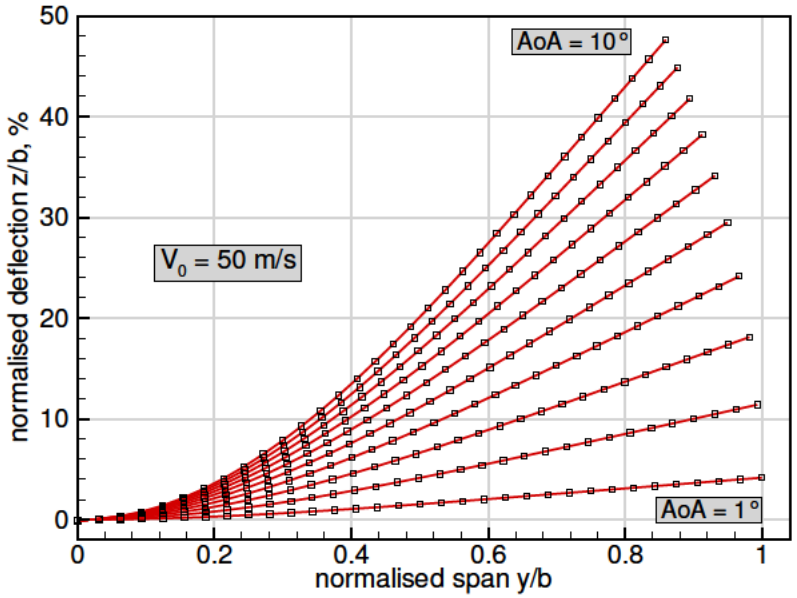

Figure 4.10: Results of static coupling simulations for 50 m/s onflow velocity evaluated at 44.75% chord

becomes apparent that the application of a geometrically nonlinear solution method is indispensable in this case. This is further emphasised by the results for the highest onflow velocity of 50 m/s presented in Fig. 4.10. The maximum tip displacement

reaches approximately 47% in the z direction and 14% in the y direction. Recalling the comparison of linear and nonlinear FE simulations (cf. Fig. 2.9), a geometrically linear solution in this case would lead to an arbitrary extension of the wing's span and in turn to an increase of the wing area by more than 14%. This would finally result in a significantly different lift distribution and deformation of the wing.

In addition to the translational displacements a method to determine the rotational displacements at the 33 evaluation points was implemented. It is based on the so-called *Euler angles*, which represent a set of three angles used to describe the orientation of a rigid body in 3-dimensional Euclidean space [36]. For this particular case, the *X'Y'Z'* convention is used to describe a rotation with ϕ about the x axis, then a rotation with θ about the y axis and finally a rotation with ψ about the z axis. The mathematical definition of this convention is provided in Appendix A.2, a detailed description can be found in reference [37]. It is important that the rotations are performed in this exact order with respect to the local, body fixed coordinate system. The roll angle ϕ then represents the global out-of-plane bending angle, which is illustrated for the 50 m/s case in Fig. 4.11 with respect to the normalised spanwise coordinate in the body fixed coordinate system. For an AoA of 10 degrees a maximum out-of-plane bending angle of 38 degrees is obtained at the wing tip. However, it can be seen that the increase in bending angle mostly appears between the clamping and approximately 50% span, which has already been observed in the illustrations of the deflections. This leads to the assumption that high stresses relevant to structural strength primarily occur in this area. In addition, this is also critical in terms of static structural stability when the prestressed skin is taken into account as the compressive stresses on the upper side of the wing can lead to buckling.

The global pitch angle θ for all AoAs at 50 m/s onflow velocity is depicted in Fig. 4.12. According to the convention selected, the roll rotation (bending for this particular case) about the x axis is performed first, followed by the pitch rotation. Consequently, the angle θ can be seen as the twist angle due to the torsional deformation. The reason for this are the aerodynamic forces acting at the quarter chord line of the wing, while the elastic axis is located at approximately 45% chord resulting in a torsional moment. In contrast to the bending angle, a high increase of the twist angle is detected over a range of 70 to 80% of the span. The maximum value of 2.6 degrees is reached at the wing tip for the highest AoA of 10 degrees. It is obvious that this twist also means an increase in local angle of attack, although the two angles are not identical. Nevertheless, an initial guess of the increase in AoA can be obtained by averaging the twist angles of all 33 evaluation points. This leads to a mean twist angle of 1.7 degrees suggesting an increase of 16% in global AoA with respect to

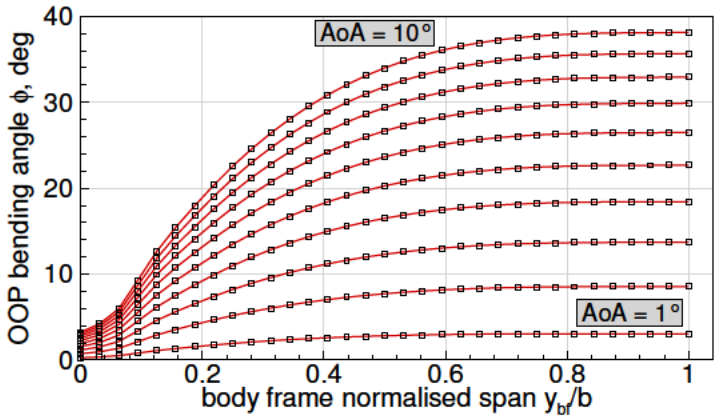

Figure 4.11: Out-of-plane bending angle for 50 m/s onflow velocity evaluated at 44.75% chord

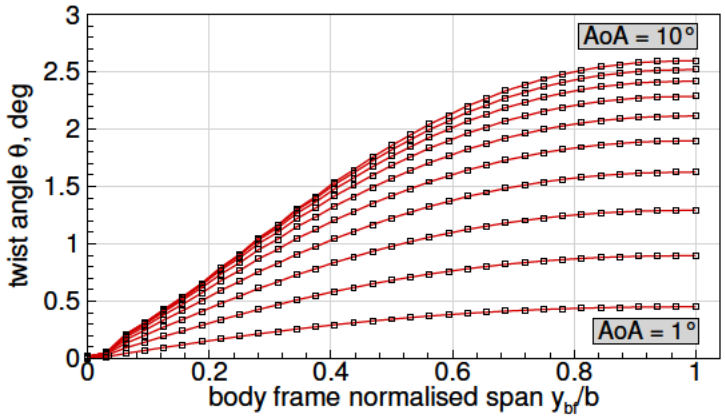

Figure 4.12: Twist angle for 50 m/s onflow velocity evaluated at 44.75% chord

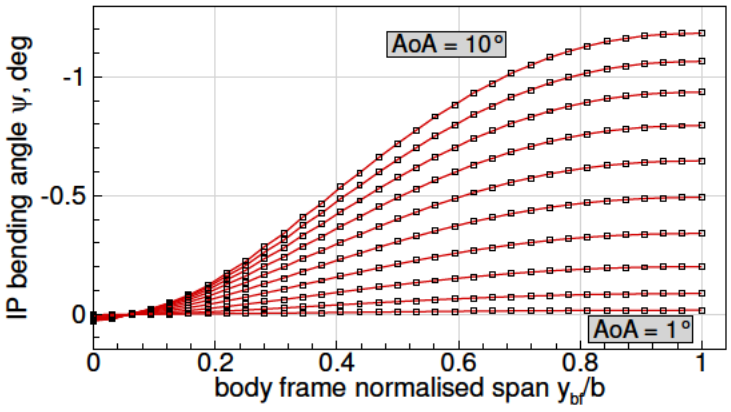

Figure 4.13: In-plane bending angle for 50 m/s onflow velocity evaluated at 44.75% chord

the wing root AoA of 10 degrees. The comparatively high magnitude of the twist angle is a further indication that common aeroelastic computation methods are not suitable for very flexible aircraft structures, as these are usually tied to the assumption of displacements in a linear regime. Finally, the Euler angles are completed by the yaw angle ψ, which represents an in-plane bending angle and is shown in Fig. 4.13. In this case, a negative angle means a deflection in the positive x direction. As can be seen, the influence of in-plane bending is rather small, with a maximum value of -1.2 degrees reached again at 10 degrees AoA. Overall, a nonlinear behaviour with respect to the (local) y coordinate is observed for all three Euler angles.

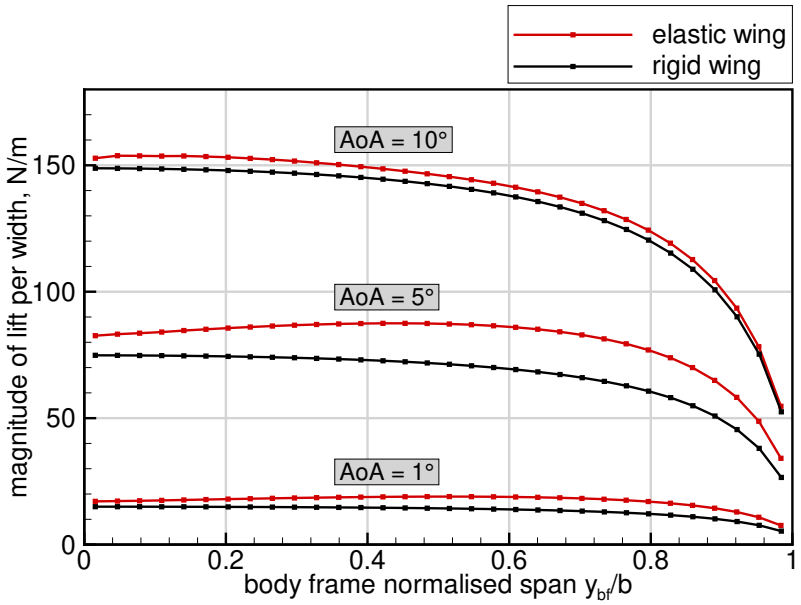

Figure 4.14: Comparison of lift distribution for rigid aerodynamic and nonlinear aeroelastic solution for 50 m/s onflow velocity

In conclusion, the lift distribution at the quarter line of the wing is depicted in Fig. 4.14. Again, the normalised spanwise coordinate is related to the body fixed frame of reference. The results are shown for both the elastic (deformed) wing computed using the static coupling solver and the wing assumed to be perfectly rigid (undeformed) computed using the steady VL implementation only. As can already be seen at 1 degree AoA, the consideration of elasticity leads to a significant increase in lifting loads per width and, in addition, to a redistribution towards the outer wing. This is in good agreement with the theoretical fundamentals of flexible wings discussed in Section 2.1. The total lift is increased by almost 30%, while the maximum lift is reached at approximately 52% wing span. With increasing AoA, the maximum load per width is slowly shifted in negative spanwise direction, reaching 45% span at 5 degrees AoA

with the increase in total lift reduced to approximately 20%. This trend continues until the maximum load is finally located at the wing root at 10 degrees AoA, where the lift distribution of the elastic and the rigid solution are in qualitatively good agreement. The deviations are mainly caused by the increase of lift due to the deformation, the twist angle that occurs and the resulting additional local AoA, which has already been discussed above. In this case, the total lift is only increased by approximately 1%.

4.2.3 Influence of Nonlinear Deformations on Modal Properties

In general, most computational methods for aeroelastic stability analysis (i.e. flutter prediction) only consider the undeformed shape of the structure, as discussed in Section 2.1.2. However, in the previous section it has been shown that structural deformation is a key parameter for the Pazy wing test case, causing significant changes in the lift distribution and the total lift achieved. This also applies to the location of critical strains and stresses relevant for the wing design. As has been described in Section 2.3.2, the consideration of large structural deformations leads to a change in structural properties, i.e. the stiffness expressed by the updated (tangent) stiffness matrix. With regard to the large static deflections at high angles of attack and high onflow velocities, it can be expected that the modal properties (eigenvalues, eigenvectors) will change significantly. In order to evaluate these changes, the eigenvalues

Table 4.3: Eigenfrequencies of the seven lowest modes of the undeformed Pazy wing

Mode	Type of mode shape	Nastran w/o skin [Hz]	Nastran skin [Hz]
1	1st OOP bending	4.42	4.67
2	2nd OOP bending	28.98	30.63
3	1st Torsion	40.33	42.22
4	3rd OOP bending	82.41	86.87
5	1st IP bending	112.27	112.60
6	2nd Torsion + 3rd OOP bending	133.09	137.14
7	3rd OOP bending + 2nd Torsion	145.1	149.44

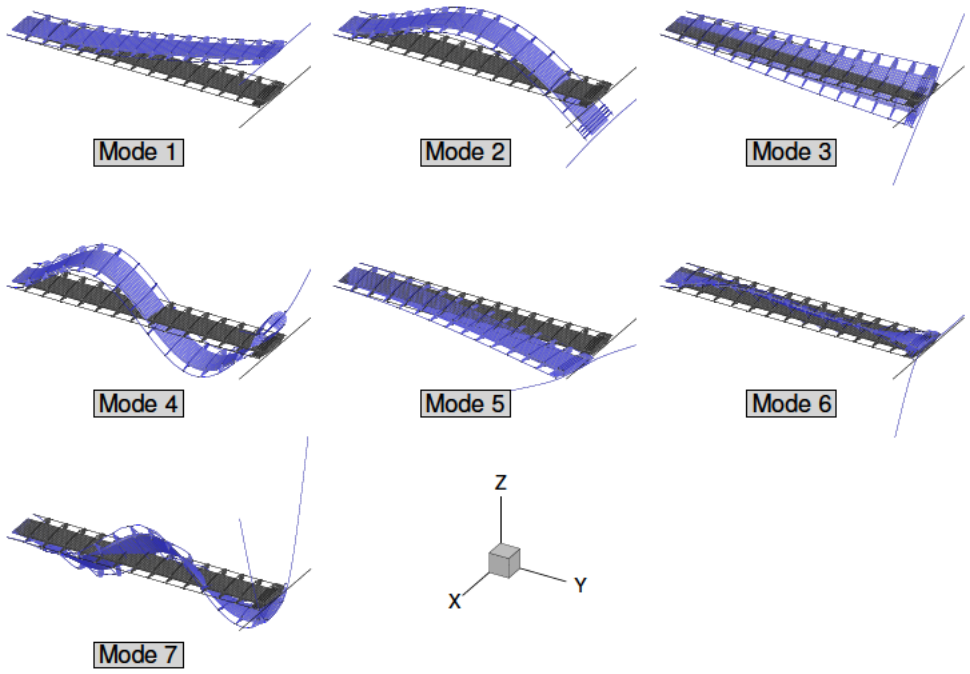

Figure 4.15: The lowest seven mode shapes of the undeformed Pazy wing structural model

or eigenfrequencies respectively are analysed as a function of the deformation. For this purpose, the extended static coupling solver as implemented for the stability analysis (see Section 3.2.3) is used, with data being obtained from a Nastran SOL400 modal analysis performed after convergence of the static coupling solution. The eigenfrequencies determined from the Nastran FE model of the undeformed wing are listed in Table 4.3. For this case and in the following, only modes in a frequency range of up to 150 Hz are taken into account. According to Section 2.3.3, the modal approach then provides reasonable results for dynamic response calculations with maximum frequencies of 75 Hz. This corresponds to a reduced frequency of approximately 0.23 at 100 m/s onflow velocity. Thus, the chosen frequency range seems to be sufficient and the first out-of-plane bending (1st OOP), the second out-of-plane bending (2nd OOP), the first torsion (1st Torsion), the third out-of-plane bending (3rd OOP), the first in-plane bending mode (1st IP) and two other modes are considered. The latter are the second torsion (2nd Torsion) with contributions from the 3rd OOP bending mode and vice versa. In addition, the eigenfrequencies are shown for the model with and without skin to give an idea of its influence. It can be seen that the frequencies are

reduced by approximately 5% when the skin is removed, which is an indication of the skin's contribution to the overall stiffness of the whole model. Solely the frequency of the first in-plane bending mode is not affected by the skin. The corresponding mode shapes of the modes presented are depicted in Fig. 4.15.

The development of the eigenfrequencies as a function of the normalised tip displacement is plotted in Fig. 4.16 for a constant angle of attack of 5 degrees and velocities ranging from 10 to 90 m/s. Here, the frequencies of the 1st OOP and the 2nd OOP bending mode remain almost constant, indicating that these modes are comparatively insensitive to the elastic structural deflection. On the other hand, significant changes are observed in the frequency of the 1st Torsion which begins to decrease considerably at 10% tip displacement and reaches the same value as the 2nd OOP bending mode at approximately 32% tip displacement and 50 m/s onflow velocity. At higher velocities, the frequency keeps decreasing and approaches the

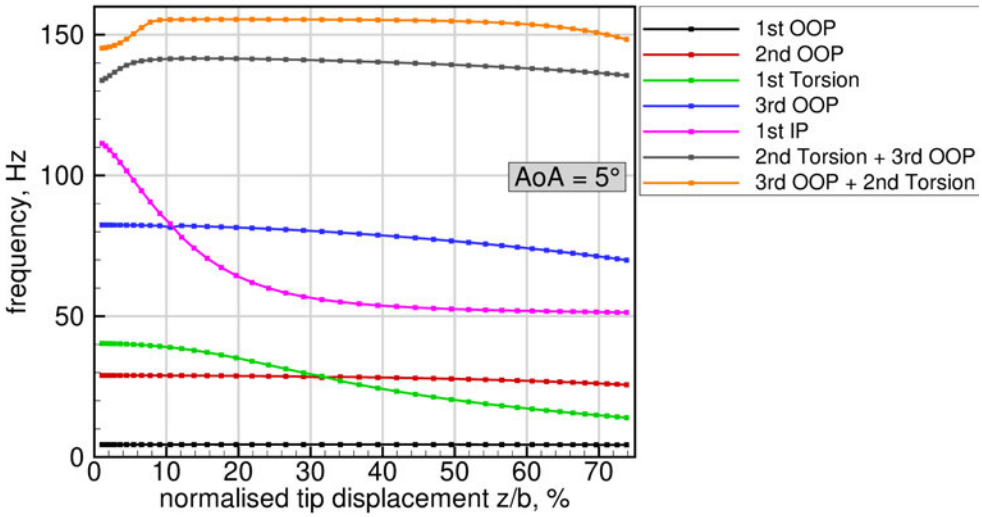

Figure 4.16: Evolution of the eigenfrequencies of the Pazy wing as function of the deformation

frequency of the 1st OOP bending mode. A similar behaviour is shown for the 1st IP bending mode, where a major frequency drop is already observed at small tip displacements, but stabilises above 30% deformation. Coincidence with the 3rd OOP bending frequency, which itself exhibits only a small decrease, is achieved at approximately 11% displacement. The frequencies of the two highest modes are increasing at small deformations, while they seem to be minorly affected at larger displacements. Concerning the mode shapes, it has to be noted that the 1st IP bending mode shows contributions of the 1st Torsion and vice versa as soon as small elastic deformations occur. This might be a reason for the frequency drop of the 1st IP mode even at

small displacements. However, the behaviour of the 1st Torsion frequency seems to be primarily affected by geometric nonlinearities, since changes occur mainly in a nonlinear regime above 10% tip displacement. Although no unsteady aerodynamic forces have been considered yet, it can be assumed that coupling of the 1st Torsion and the 2nd OOP bending mode will lead to aeroelastic instabilities.

4.2.4 Stability Analysis

Following the investigation of the modal properties as a function of the elastic deformation, the aeroelastic stability of the Pazy wing is analysed by means of the proposed method. For this purpose the linearised static coupling solution sequence, as shown in Fig. 3.4, is used to build the monolithic discrete-time state-space model and solve the homogeneous eigenvalue problem for the dynamics matrix. For the following results, the discretisation of the wing presented in Table 4.2 was adopted for the static coupling solution. Structural damping as well as gravity were not taken into account in order to ensure comparability with the results from another member of the Large Deflection Group (see Section 4.2.6). With regard to the state-space model, the wake length is set to four times the wing span. This should be sufficient as the influence of the wake is reduced quadratically with increasing distance according to the Biot-Savart law (cf. Eq. (2.14)). Additional parameters relevant for the stability analysis can be found in Table 4.4. The resulting complex eigenvalues are transformed into continuous-time formulation and filtered to extract the relevant eigenvalues of the structural states, i.e. the generalised coordinates $q_{1,i}$ (see end of Section 3.2.3). In general, the entire solution sequence, including the static coupling solution, is performed for increasing

Table 4.4: Parameters of the stability analysis setup

Angle of attack	0° - 5°
Free stream velocity	10 -120/90 m/s
Wake length	4b = 2.2 m
Wake panel rows	352
Aerodynamic states/wake panels	11,264
Structural states	21

velocities at constant angles of attack. Once the simulations for the velocity sweep of an specific angle of attack have been completed, there are various ways to illustrate the eigenvalues and the aeroelastic stability of the wing. A common method are so-called *root locus plots*, where eigenvalues for different flight conditions (onflow velocity and AoA in this case) are represented in the complex plane. According to Section 3.2.1, the real parts (x axis) then represent the damping ratios, where the mode is considered stable as long as the damping value is negative. In addition, the imaginary parts (y axis) represent the frequencies of each mode.

The root loci of the Pazy wing for angles of attack ranging from 0 to 5 degrees are depicted in Fig. 4.17. In this case, the evolution of the 1st OOP and 2nd OOP bending mode and the 1st Torsion mode are presented as only these modes show changes relevant for the stability. The velocity was varied from 10 to 120 m/s for the 0 degree AoA case and from 10 to 90 m/s for all other cases, due to partial convergence issues of the static coupling solver at very large deflections of the wing. An increasing flow velocity corresponds to a higher contrast of the dots, where the step size is set to 2 m/s. It can be seen, that the frequency and damping of all three modes considered change significantly when the velocity is increased. Regarding an angle of attack of 0 degrees, the frequencies of all three modes decrease, while the damping is at first increased. However, the damping of the 1st Torsion mode is already reduced for low velocities, then turns positive and thus the mode becomes unstable. While the mode turns stable again at higher velocities, the 2nd followed by the 1st OOP bending also becomes unstable at further increased velocities. Comparing the root loci for increasing angles of attack, significant changes in the evolution of the eigenvalues are observed. The instabilities in the 1st Torsion and the 2nd OOP bending mode seem to occur at lower velocities. In contrast, no instabilities are detected in the 1st OOP bending mode, which is mainly due to the smaller velocity range considered. From 3 degrees angle of attack onwards, this mode also shows an interesting behaviour in the frequency, which increases instead of decreasing. Nevertheless, considerably differences between the plots appear mostly between 0 and 2 degrees angle of attack, while the eigenvalues seem to be rather insensitive at higher angles of attack.

A more detailed insight into the flutter mechanisms involved is provided by the V-g and V-ω plots. Here, the damping ratio and the frequency of each mode considered are presented with respect to the onflow velocity. For simplification, in the following the trends of the different modes are identified by the dominant structural mode at low velocities. Due to the unsteady aerodynamic forces, these are now complex modes that may include considerable contributions of other structural modes. The plots for the undeformed wing at 0 degree angle of attack and 10 to 120 m/s onflow velocity are

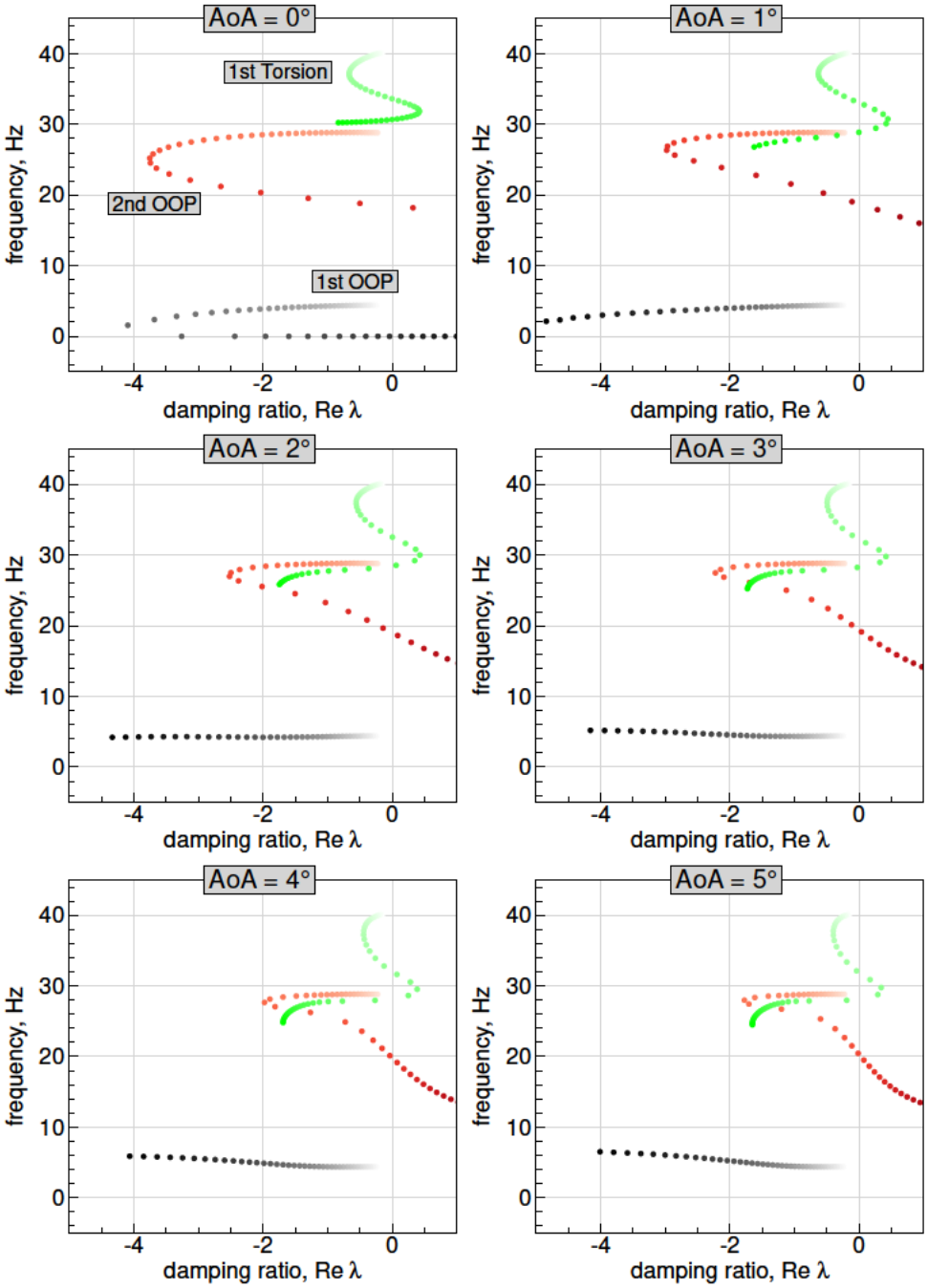

Figure 4.17: Root loci of the Pazy wing for AoAs ranging from 0 to 5 degrees and velocities from 10 to 120/90 m/s; increased contrast corresponds to higher flow velocity

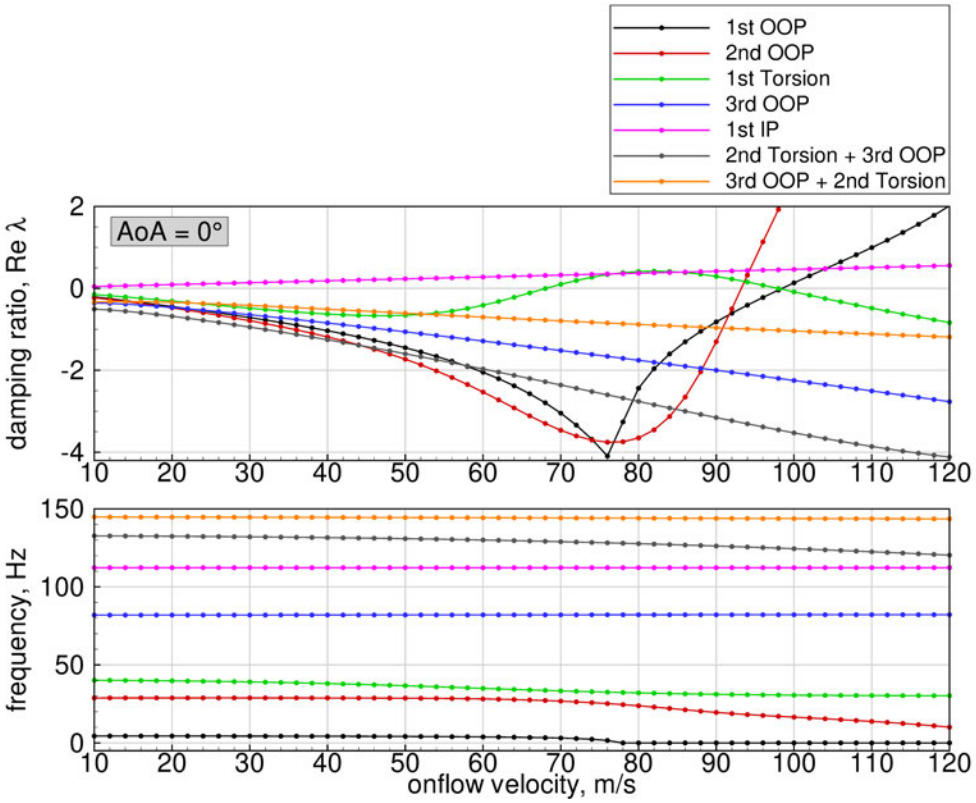

Figure 4.18: Damping and frequency trends of the Pazy wing for 0 degrees angle of attack and velocities ranging from 10 to 120 m/s

shown in Fig. 4.18. In this case, the critical flutter mode is obviously the 1st Torsion mode, which shows a zero crossing in the damping plot at approximately 68 m/s and becomes unstable. Since the frequency of this mode is decreasing and approaches the frequency of the 2nd OOP bending mode, this instability is caused by coupling of the 1st Torsion and the 2nd OOP bending mode. Consequently, the flutter mechanism incorporates contributions from both modes. As the 1st Torsion mode becomes stable again at 98 m/s, it is referred to as a so-called hump mode [38]. The 2nd OOP bending mode, however, shows instability already at 94 m/s, although its frequency diverges from the frequency of the 1st Torsion mode. An important difference in this context is the 'type' of flutter that occurs. The damping gradient of the 1st Torsion mode at flutter onset is comparatively small, which is also called *soft* flutter. In contrast, the 2nd OOP mode shows a large gradient at the zero crossing. This is referred to as *hard* flutter [13]. Due to the soft flutter of the 1st Torsion mode with small positive damping values, this instability might result in a limit cycle oscillation (LCO). This can be considered as bounded flutter, where the amplitude of the unstable motion

is limited by aerodynamic or structural nonlinearities, e.g. a change of stiffness due to deflection [13]. An investigation of LCOs by extension of the developed state-space model should therefore be considered for future research. The flutter onset of the 2nd OOP mode is followed by the 1st OOP bending mode, which becomes unstable at 98 m/s. Interestingly, the frequency of this mode reaches a value of 0 Hz at 78 m/s and remains constant, representing a non-oscillatory eigenvalue. Thus, this instability can be be seen as a steady divergent mode. The calculation of wing divergence by means of the proposed method will be pursued in the future since interpretation of non-oscillatory eigenvalues is not straightforward and needs to be treated carefully [13]. At this point, it has to be noted that the 1st IP bending mode exhibits increasing positive damping values along the entire velocity range. As mentioned in Section 3.2.2, viscous or induced drag forces have not yet been integrated into the linearised aeroelastic model. Furthermore, several higher-order terms accounting for components in the flow direction had to be neglected during the derivation of the aerodynamic model. The linearised aeroelastic model, hence, does not consider any forces in the flow direction, which means that the 1st IP bending mode is undamped for all flow velocities in the undeformed case.

The contributions of the different structural modes to the complex 1st and 2nd OOP bending and the 1st Torsion mode are depicted in Fig. 4.19. These are obtained from the complex eigenvectors, which can be considered as complex state vectors with each entry being related to the state variable at the same position in the state vector. As the eigenvectors include the contributions of all state variables, the magnitudes of the complex entries of the generalised coordinates $q_{1,i}$ are normalised and plotted as a function of the velocity. The complex aeroelastic 1st OOP bending mode is obviously dominated by the structural 1st OOP bending mode (represented by $q_{1,1}$ in the state-space model), where a small discontinuity is shown when the frequency of this mode reaches 0 Hz (78 m/s). An increasing contribution from the structural 1st OOP mode is observed in the plot of the aeroelastic 2nd OOP bending mode. This leads to the interesting fact, that the mode shape comprises approximately 57% from 1st OOP bending and only 32% from the original dominating 2nd OOP bending mode when it becomes unstable at 94 m/s. In contrast, the 1st Torsion mode contributes only 9% to this instability. An explanation of the dominating 1st OOP bending mode could possibly be the decreasing frequency of the 2nd OOP mode approaching the 1st OOP mode. Regarding the complex 1st Torsion mode, the increasing magnitude of the structural 2nd OOP bending was expected due to the proximity of the frequencies of these two modes. At flutter onset (68 m/s) the 2nd OOP bending contributes approximately 57%, the 1st Torsion 24% and the 1st OOP bending 18% to the complex mode shape.

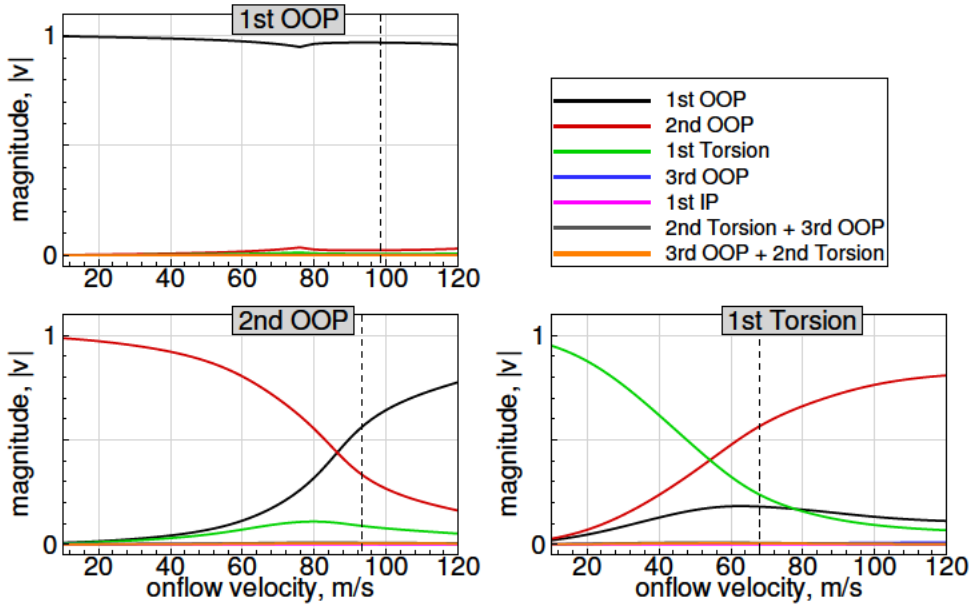

Figure 4.19: Contributions of the structural DOFs to the lowest three complex mode shapes of the Pazy wing for 0 degrees angle of attack and velocities ranging from 10 to 120 m/s; vertical line marks flutter onset

The V-g and V-ω plots for the deformed wing at 1 degree angle of attack are shown in Fig. 4.20. As mentioned before, the pure structural 1st IP bending and the 1st Torsion mode now include contributions from each other, caused by the structural deflection. Thus, the aeroelastic 1st IP mode is damped and becomes stable at higher flow velocities. The flutter onset of the 1st Torsion mode is reduced to approximately 61 m/s and the mode becomes stable again at 74 m/s. A decrease in flutter velocity is also observed for the 2nd OOP bending mode, which shows instability above 82 m/s. An interesting behaviour is shown by the seventh mode, that incorporates 3rd OOP bending and 2nd Torsion. This mode is only minimally damped at velocities above 58 m/s, which might be caused by the torsional motion included in the pure structural mode shape. In general, the decrease of the flutter velocities can be clearly related to the change of the structural eigenvalues due to the deflection of the wing (cf. Section 4.2.3). The particular contributions of the structural modes to the 2nd OOP bending, the 1st Torsion and the 1st IP bending mode are presented in Fig. 4.21. Regarding the magnitudes for the 2nd OOP bending, it can be seen that the instability at 82 m/s is mainly caused by coupling of 1st OOP bending and 1st Torsion. High contributions (more than 50%) of the 2nd OOP mode appear during the instability of the 1st Torsion mode between 61 and 74 m/s. However, a rapid decrease of these is observed at approximately 75 m/s, since the frequency of the 2nd OOP diverges from

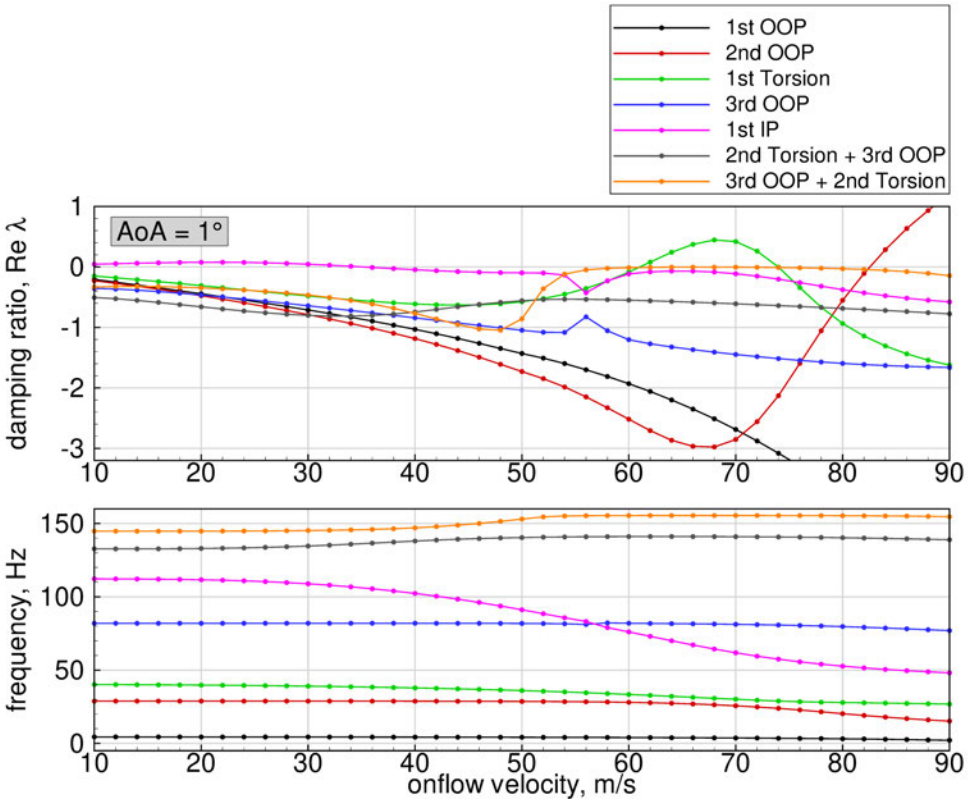

Figure 4.20: Damping and frequency trends of the Pazy wing for 1 degree angle of attack and velocities ranging from 10 to 90 m/s

the 1st Torsion mode, causing the mode to become stable again. Interestingly, the plot of the seventh mode (3rd OOP + 2nd Torsion) initially shows an increasing contribution from the sixth mode (2nd Torsion + 3rd OOP) which decreases at above 50 m/s as the frequencies of these two modes move apart. The low damping values of the seventh mode thus seem to be related to the decoupling from the sixth mode. One reason for the low stability may be the already existing contributions of bending and torsion in the pure structural mode. However, flutter does not occur as unsteady forces cannot impose a phase shift between different mode contributions in one structural mode shape. Another reason could be a change of the mode shape due to the deflection of the wing, as observed for the 1st Torsion and 1st IP bending mode. This is also indicated by the increase in the natural frequency of the seventh structural mode between 0 and 10% tip displacement (see Fig. 4.16).

Finally, the frequency and damping trends for 5 degrees angle of attack are depicted in Fig. 4.22. The flutter velocity for the 1st Torsion mode is further reduced to 42 m/s while the mode turns stable again at approximately 49 m/s. In comparison

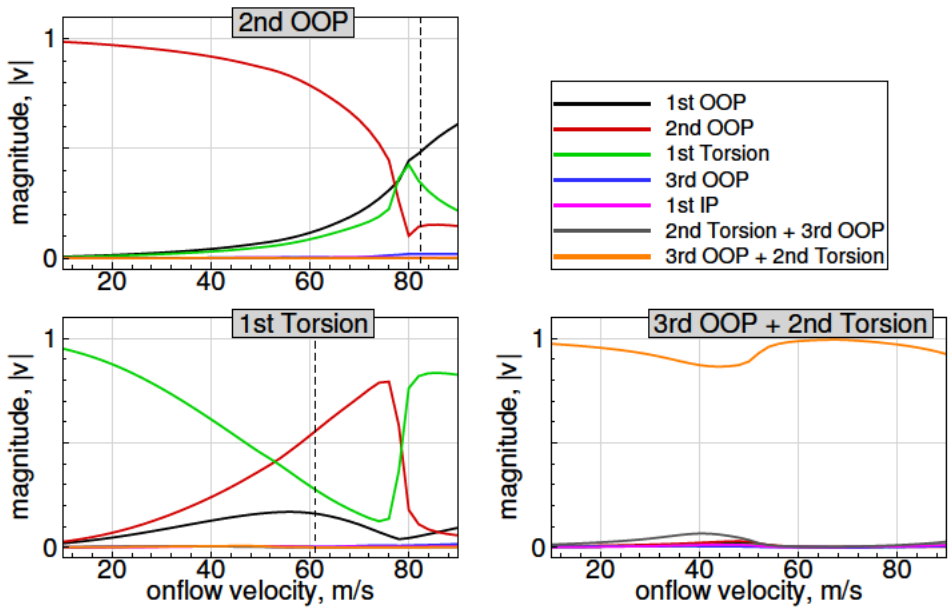

Figure 4.21: Contributions of the structural DOFs to the second, third and seventh complex mode shape of the Pazy wing for 1 degree angle of attack and velocities ranging from 10 to 90 m/s; vertical line marks flutter onset

to the undeformed case, the velocity range for the instability of this hump mode is also reduced from 30 m/s (0 degree AoA) to 7 m/s. Furthermore, the velocity for the instability of the 2nd OOP bending mode is reached at approximately 60 m/s, with the mode shape including almost equal contributions from 1st and 2nd OOP bending and 1st Torsion. An overview of the flutter velocities, the corresponding tip displacement and the structural modes incorporated for angles of attack ranging from 0 to 5 degrees is given in Table 4.5. As already expected and observed in the damping trends, an increase in angle of attack results in a significant reduction in the flutter velocity of both critical flutter modes. In both cases, this decrease can be quantified with approximately 10% between 0 and 1 degree angle of attack and more than 35% between 0 and 5 degrees angle of attack. For the second flutter mode, which is caused by coupling of 1st and 2nd OOP bending and 1st Torsion, the flutter velocity seems to be restricted by a maximum normalised tip displacement of 45%. This is clearly a consequence of the change of modal properties discussed in the previous section as the frequency of the structural 1st Torsion mode is between the frequencies of the 1st and 2nd OOP bending mode at this point (see Fig. 4.16). A similar behaviour can be observed for the first flutter point (2nd OOP bending and 1st Torsion), where the restricting tip displacement might be reached at approximately 24%. The reason for this again is the decreasing frequency of the structural 1st Torsion mode caused only by the deflection

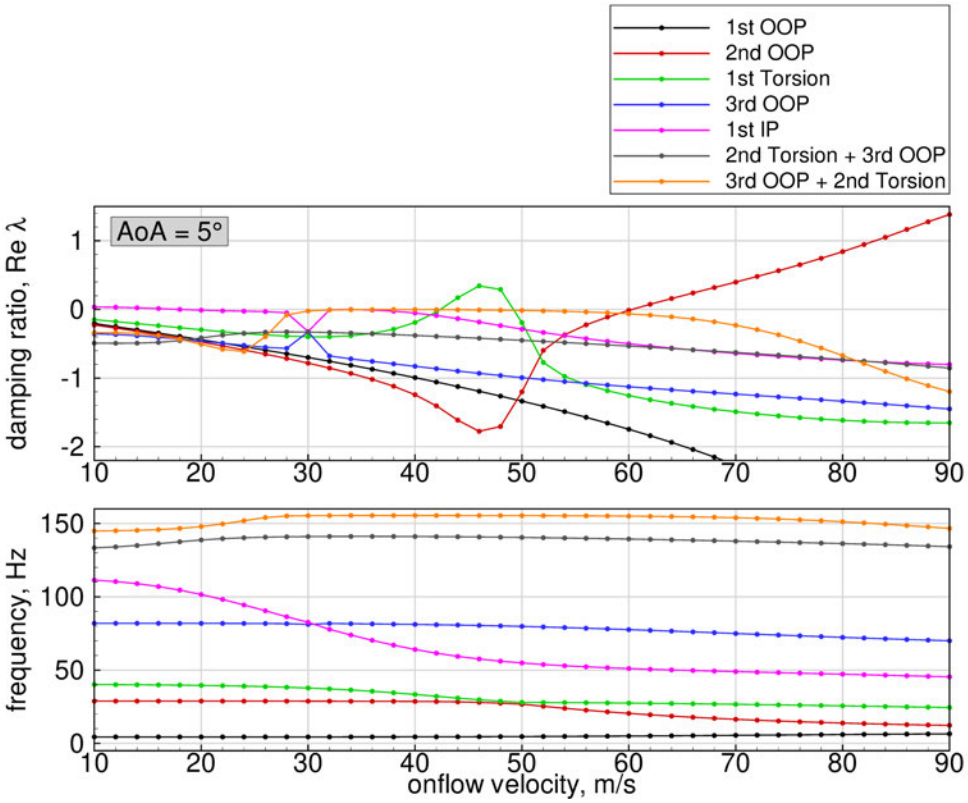

Figure 4.22: Damping and frequency trends of the Pazy wing for 5 degrees angle of attack and velocities ranging from 10 to 90 m/s

Table 4.5: Flutter velocities and corresponding tip displacements for angles of attack ranging from 0 to 5 degrees

AoA [deg]	1st Flutter velocity [m/s]	Tip displ. [%]	2nd Flutter velocity [m/s]	Tip displ. [%]
0	68.1	0	93.2	0
1	61.0	13.3	82.5	37.1
2	54.0	17.7	75.2	42.1
3	49.0	19.9	69.5	44.2
4	45.3	21.3	64.6	45.0
5	42.3	22.3	60.3	45.0

of the wing, which approaches the frequency of the 2nd OOP bending mode.

To conclude this section, the regions of instability for six different angles of attack are depicted in Fig. 4.23. Here, the flutter velocity is plotted as a function of the normalised tip displacement. This diagram illustrates that the region of instability of the hump mode becomes smaller with increasing angle of attack. In addition, the velocity range between the first and the second flutter mode is considerably increasing. The phenomenon of a restricting maximum tip deflection at high angles of attack also appears in the 'stabilisation' velocity of the hump mode, which is limited to approximately 31%. Overall, it is shown that structural nonlinearities due to large deformations have a great impact on the aeroelastic stability of highly flexible wings in terms of flutter. This

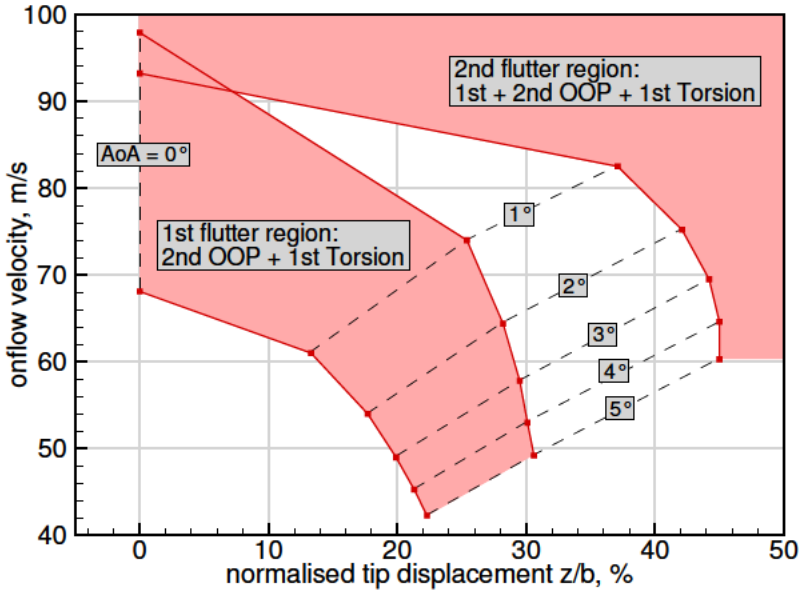

Figure 4.23: Regions and boundaries of flutter instabilities of the Pazy wing for AoAs ranging from 0 to 5 degrees

is mainly caused by the changes in modal properties, where even small deformations in a linear regime (<10% tip displacement) can already lead to considerable changes in the natural frequencies and the mode shapes. As a result, the flutter velocities are reduced as the frequencies can now be in a favourable range for the coupling of two modes even when unsteady aerodynamic forces are not considered. Furthermore, large deformations also lead to a change of the complex aeroelastic mode shapes, e.g. in the second flutter mode (2nd OOP bending). In this case the decreasing contribution of the 1st OOP bending mode and the increasing contribution of the 1st Torsion mode between 0 and 5 degrees angle of attack lead to a change from hard to comparatively soft flutter. This can also bring up new critical damped modes, as can be seen in Fig. 4.21 for the seventh mode. However, further investigations to quantify

the influences of structural nonlinearities, e.g. by comparing the results presented with simulations using the deformed structure but the modal properties of the undeformed wing, are necessary but beyond the scope of this thesis.

4.2.5 Validation of Stability Analysis using Nastran SOL145

After the results of the Pazy wing test case have been presented, the methods used will be validated by the means of computational data obtained from other solvers. At first, the proposed method for stability analysis will be validated using the aeroelastic flutter analysis SOL145 in Nastran. This is necessary as the state-space model has so far only been *verified* in the time domain (see Section 4.1.2), but the results of the stability analysis are obtained in the frequency domain. For this purpose, using Nastran SOL145 seems convenient as the FE model is already available in Nastran format (.bdf) and can be used directly as an input for the solver. However, since the solution of subsonic aerodynamic problems in Nastran is based on the doublet lattice method (DLM), which is only valid for small out-of-plane deflections, the computations are only performed for the undeformed case. The theory of the DLM is not reproduced here, but can be found in reference [39]. In general, the DLM is based on linearised aerodynamic potential theory, extending the steady VLM to unsteady flow [19]. Similar to the VLM, aerodynamic influence coefficients are calculated which are then transformed into generalised aerodynamic force matrices. Afterwards, these matrices are used to solve the flutter equations. In Nastran there are three different methods available.

For this particular case, the *p-k* has been chosen, which is shortly described in Section 2.1.2. The desired method, among other parameters required for the flutter solution, is again specified in the bulk data entry of the Nastran input file. A detailed description of the Nastran SOL145 solver will be dispensed at this point, but is presented in reference [40]. The aerodynamic setup regarding the density and the discretisation of the aerodynamic grid is based on the setup shown in Table 4.2, used for the static coupling simulations. In addition, the same number of modes (7) is considered as it also was for the stability analysis. Finally, the range of reduced frequencies is specified from 0.01 to 30 and the velocity range from 2 to 120 m/s using a step size of 2 m/s.

Since the damping values obtained from the eigenvalues of the state-space model and the Nastran flutter analysis cannot be directly compared, the flutter velocities and corresponding frequencies from both methods are listed in Table 4.6. The results are in good agreement with small deviations of approximately 2% for the 1st

Table 4.6: Flutter velocities and corresponding frequencies from linearised state-space model and Nastran SOL145 flutter analysis

	Lin. state-space model	Nastran SOL145
1st Flutter velocity [m/s]	68.1	66.6
Frequency [Hz]	33.6	34.0
2nd Flutter velocity [m/s]	93.2	93.3
Frequency [Hz]	18.4	18.4
3rd Flutter velocity [m/s]	98.5	98.8
Frequency [Hz]	0	0

flutter velocity. Obviously, the 1st flutter point is detected at a higher velocity and a smaller frequency in the state-space model, which could be caused by the forces neglected during the linearisation. An indication for this is the behaviour of the 1st IP bending mode, which shows zero damping in the Nastran solution over the entire velocity range, although no drag forces are considered in the DLM. Besides, the velocities for the second and third flutter point show deviations below 1% and the frequencies show no deviations at all. The V-ω plot for the first three modes comparing both solutions is presented in Fig. 4.24. Again, the frequencies show a very good match and only small differences are to be observed. Thus, the proposed method for

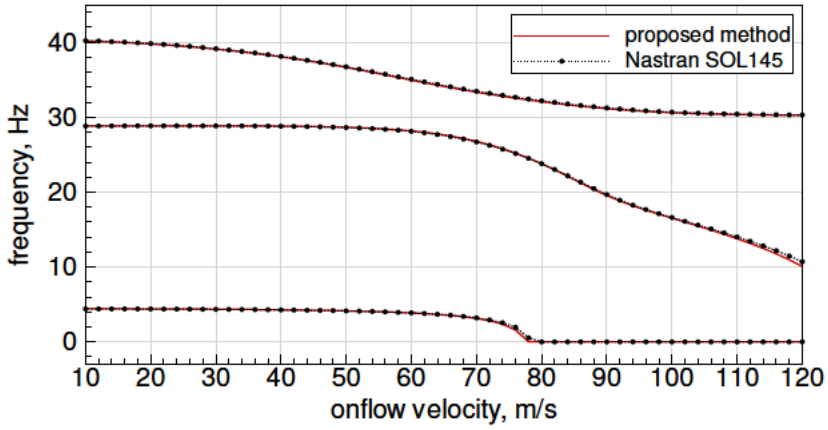

Figure 4.24: Comparison of frequency trends obtained by the proposed method and Nastran SOL145 for the undeformed case (0 degrees AoA)

stability analysis using the linearised aeroelastic state-space model developed can be considered valid for the undeformed case.

4.2.6 Validation of Stability Analysis using Data from Imperial College Group

In the following, the results of the stability analysis for the deformed case are validated with data provided by Imperial College London, another member of the Large Deflection Working Group. The simulations of this group were performed using *SHARPy* (Simulation of High-Aspect Ratio aeroplanes in Python), a dynamic aeroelastic simulation toolbox for very flexible aircraft and wind turbines developed at the Department of Aeronautics of Imperial College London. In general, SHARPy offers several different solutions to the user, whereas in this case only the static aeroelastic solution and the stability analysis are relevant. The aerodynamic solver is based on the unsteady vortex lattice method, similar to the aerodynamic solver used in this thesis (see Sections 2.2 and 3.1.1). In contrast, the structural solution is obtained using a displacement-based, geometrically exact, nonlinear beam solver, where rigid body motion can be prescribed or simulated. The stability analysis is carried out in a similar manner to the proposed method by linearisation around a nonlinear equilibrium and building a linear state-space model. Unlike the linearised aeroelastic model presented here, the linearisation in SHARPy also takes the aerodynamic drag forces into account. A detailed description of SHARPy and its capabilities is presented in references [41] and [42]. The software is open source and can be obtained from github [43].

The results of the stability analysis for the deformed case are heavily dependent on the results of the static coupling simulations. Thus, the static aeroelastic equilibrium points from both solvers must be compared at first, in order to determine the influences of the different structural solution methods (nonlinear beam model vs. nonlinear full FE model). The normalised out-of-plane displacements for the highest onflow velocity of 50 m/s and five different angles of attack are therefore presented in Fig. 4.25. As can be seen, the deflections obtained from SHARPy at Imperial College appear to be smaller than the deflections presented in this thesis. The relative maximum deviation is approximately 6% at 2 degrees angle of attack and decreases to 2% for the highest angle of attack. Interestingly, an almost constant deviation of 1.2 % normalised deflection in the z direction is observed between 4 and 8 degrees angle of attack. One reason for these differences can be the different positions of the elastic axis in both models, shown in Fig. 4.26. As has been mentioned before, the beam and obviously its elastic axis are located at a constant chordwise position of 44.75%.

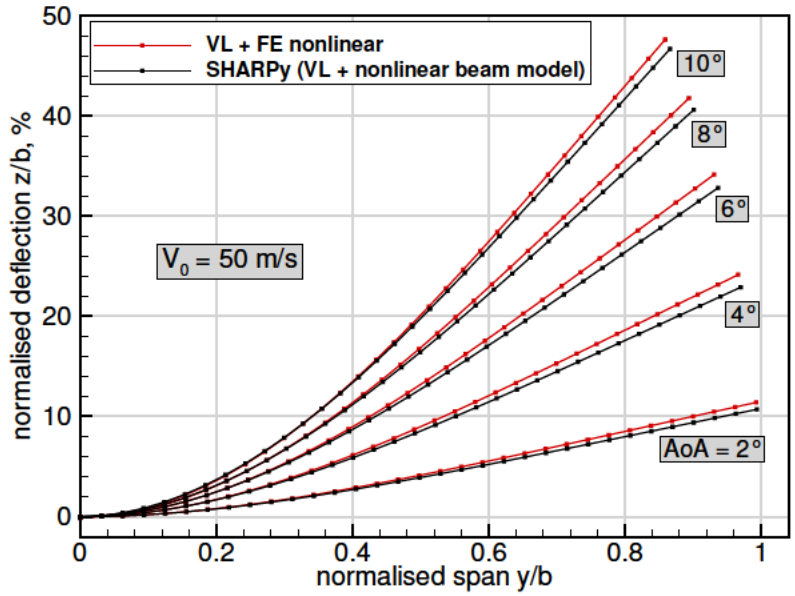

Figure 4.25: Comparison of static coupling results with data provided by Imperial College (SHARPy) for 50 m/s onflow velocity evaluated at 44.75% chord

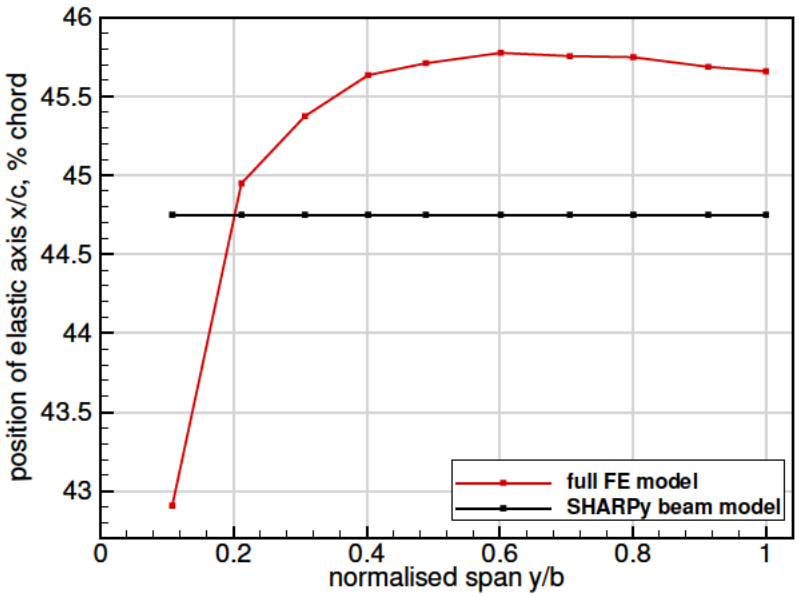

Figure 4.26: Position of elastic axis in the full FE model and in the equivalent SHARPy beam model evaluated at 10 equidistant points

However, it can be seen that the position of the elastic axis in the Nastran FE model is not constant, but changes with respect to the spanwise coordinate. Since it is mainly located behind the elastic axis of the beam model, the higher displacements might

be explained by a larger twist due to an increased distance between elastic axis and aerodynamic centre. In addition, the varying position of the elastic axis also contributes to the nonlinearities occuring in the twist angle (cf. Fig. 4.12). A major reason for the deviations in the deflections are, of course, the different methods for the structural solution. For the simulations in SHARPy the FE model has to be transformed into an equivalent beam model, which can lead to a model mismatch. Besides, out-of-plane bending always occurs coupled with chordwise bending deformations in a 3D wing box, also changing the camber of the wing. This effect is not considered when a beam type model is used [8]. Previous validations of the static coupling solver with results from a nonlinear, strain-based beam solver for a similar test case (up to 35% displacement with respect to semi-span) have shown comparable deviations in terms of out-of-plane displacements (see [8]).

Table 4.7: Comparison of eigenfrequencies (undeformed wing) obtained by Nastran full FE model and SHARPy equivalent beam model [44]

Mode shape	Nastran w/o skin [Hz]	SHARPy w/o skin [Hz]
1st OOP	4.42	4.43
2nd OOP	28.98	29.15
1st Torsion	40.33	41.63
3rd OOP	82.41	83.34
1st IP	112.27	113.11

As the modal properties of the structure are of significant meaning for the stability of the aeroelastic system, the eigenfrequencies of the Nastran FE model and the SHARPy beam model are compared in Table 4.7 for the undeformed case. The highest deviation of approximately 3% is observed in the frequency of the 1st Torsion mode, which could also lead to differences in the results of the stability analysis. A comparison of the eigenvectors, however, is not straightforward due to the different grids of both models and would be beyond the scope of this thesis. This should be considered in future investigations along with a comparison of the evolution of eigenfrequencies as a function of the structural deformation (see Section 4.2.3). The comparison of the flutter velocities as a function of the normalised tip displacement for five different angles of attack is presented in Fig. 4.27. Considering the undeformed case, high deviations in the velocity of the first flutter onset are observed. The velocity

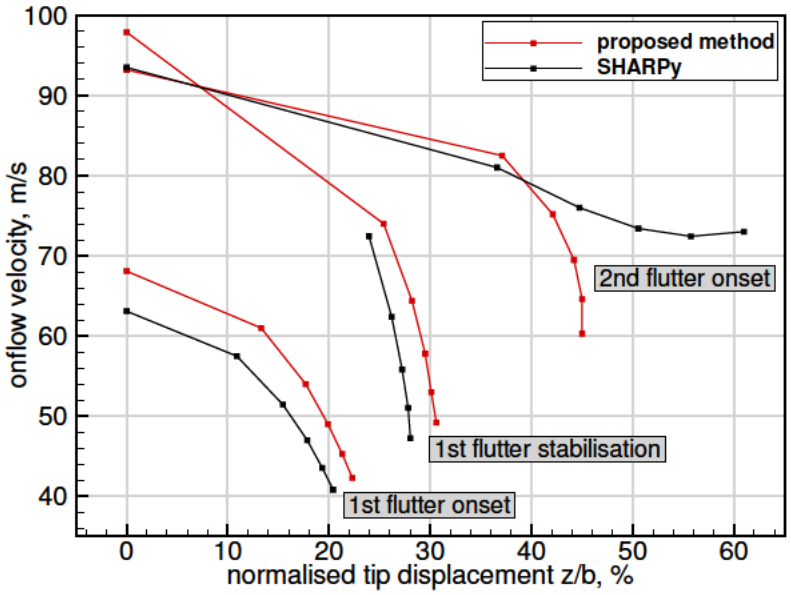

Figure 4.27: Comparison of flutter velocities with data provided by Imperial College for AoAs ranging from 0 to 5 degrees

determined by the proposed method is approximately 8% higher than the velocity computed by SHARPy. In contrast, the point of second flutter onset shows a good match with differences below 1% between both solutions. For the stabilisation of the first flutter instability, no data was available from SHARPy regarding the undeformed wing. A reason for the differences in the first flutter velocity is not apparent at this point and must therefore be investigated further in the future. As the results of the stability analysis for the undeformed wing were already validated with results obtained by Nastran SOL145 (see Section 4.2.5) using the same full FE model, a possible explanation could again be the different solution approaches (beam vs. full FE model). With increasing angle of attack, the results become additionally influenced by the differences in the static coupling results, as indicated by the deviations of the flutter points in the x axis (normalised tip displacement). Regarding the first flutter onset, SHARPy provides smaller velocities and tip displacements for all angles of attack. At 5 degrees angle of attack, the differences in velocities are approximately 4%, with 9% deviation in tip displacements. A similar behaviour can be observed for the first flutter stabilisation boundary, although the results from both solutions seem to diverge with increasing angle of attack. The second flutter onset, however, shows completely different trends when comparing the two solvers. While both velocity and tip displacement are in good agreement for small angles of attack, the second flutter boundary seems to be limited to 45% tip displacement in the proposed method. The

results obtained from SHARPy show the opposite effect, with the tip displacement further increasing to a maximum of 60.9% span, while the velocity reaches a minimum at 4 degrees angle of attack and then increases slightly. Since the reason is yet unknown to the author, an investigation of this behaviour will have to be pursued in the future. Overall, the development of the flutter velocities as a function of the tip displacement shows qualitatively similar behaviour for both solutions. On one hand, variations are partly due to the different modelling approaches, which already have an impact on the static coupling results, as discussed above. Another aspect are differences in the formulation of the linearised model used for the stability analysis, e.g. drag forces. These are considered in SHARPy but have been neglected in the current implementation of the proposed method. These issues should therefore be taken into account in future research. In addition, further investigations of aeroelastic stability at very large deformations appear necessary, as the results at displacements above approximately 40% show significant differences compared to the SHARPy results. Nevertheless, as the results presented in this chapter confirm, the method proposed in this thesis is generally capable of determining the aeroelastic stability of a highly flexible wing.

5 Conclusion and Outlook

5.1 Summary and Conclusions

The goal of this thesis was the aeroelastic modelling and validation of the highly flexible Pazy wing wind tunnel model. As large deformations were expected due to the wing's special design, the simulations should in particular account for the nonlinear behaviour of force-structure interaction (follower force problem) and geometric nonlinearities. The low operating speeds of the wing allowed the application of aerodynamic potential-based methods. Therefore, an aeroelastic solver developed at DLR was used, coupling a geometrically nonlinear vortex lattice method with the finite element solver Nastran. Follower forces as well as geometric nonlinearities were considered by a fully nonlinear formulation of the aerodynamic solution (deformed aerodynamic grid, update of panel normals, etc.) and by using the nonlinear solution sequence SOL400 in Nastran for the structural solution. Besides determining steady aeroelastic equilibrium points by the means of this solver, the aeroelastic stability of the wing in terms of flutter was also to be investigated. Since common flutter speed prediction methods are only applicable to rigid structures undergoing small deformations, an important part of this thesis was the development of a method for the stability analysis of highly flexible wings. Therefore, a linearisation of the whole aeroelastic system at static equilibrium points with large deformations was necessary.

A linear aerodynamic model was derived at first by transforming the existing unsteady vortex lattice implementation into a linear discrete-time state-space system. In this particular case, the system states were decided to be the circulation of the wake panels. The panel normal vectors, the velocity induced by the elastic deformation of the wing and their corresponding first time derivatives were defined as inputs of the system. The calculation of drag forces was not included, furthermore several higher-order terms accounting for force components in the flow direction had to be neglected as well in the linearisation. Hence, no forces in the flow direction were considered in the linearised aerodynamic model. From a structural point of view, a modal approach in generalised coordinates was used to describe the dynamic behaviour of the

system. In this regard, the linearisation was straightforward, as the transformation of second order structural dynamics equations of motion into a linear continuous-time state-space model is widely presented in the literature. The states of this system were then the generalised coordinates and the inputs were the forces acting on the structure. For the integration of both aerodynamic and structural model into a linear monolithic aeroelastic state-space model, the structural model was converted from continuous-time into discrete-time formulation. The inputs of the aerodynamic model, e.g. the panel normal vectors and their first time derivatives, were then expressed using the states of the structural system and vice versa. This finally resulted in a linear aeroelastic state-space model consisting of a dynamics matrix and a state vector containing the states of the two original models (wake circulations, generalised coordinates). However, the system was extended by an additional state, which is used to model the unsteady forces that occur due to the acceleration of the elastic motion of the wing. This state is only calculated from the original states of the system and is necessary as these cannot be used to express the acceleration term. The aeroelastic stability could then be analysed by solving the homogeneous eigenvalue problem for the dynamics matrix. The real and imaginary parts of the resulting complex eigenvalues represent the damping ratios and frequencies, whereas the system is considered stable when all damping ratios are negative. Since the developed aeroelastic state-space model mainly consists of aerodynamic states, an algorithm for the extraction of eigenvalues corresponding to the relevant structural states (generalised coordinates) was implemented. In order to take into account the effects of geometric nonlinearities on the aerodynamic and structural properties, the proposed method was integrated into the static coupling solution sequence of the aeroelastic solver. This ensured that the stability is analysed at steady aeroelastic equilibrium, considering the deformed aerodynamic grid and the changed natural modes due to the deflection of the structure.

The verification of the linearised aerodynamic model was done using an unsteady vortex lattice solver in the time domain. This was possible because the developed state-space systems are in discrete-time formulation, which can be used for time-marching. A harmonically oscillating wing was chosen as verification test case and a range of different onflow velocities, amplitudes and reduced frequencies were used. The results of the steady and unsteady forces in the z direction from both solutions were compared in the time domain and were almost coincident for the parameter variations shown. Subsequently, the linearised aeroelastic model was verified using a nonlinear modal solver in the time domain. To this end, three arbitrary structural models were created: two single degree of freedom systems with a generic heave and pitch mode respectively and a two degree of freedom system incorporating both

modes. In this case, the results were obtained by simulating the free vibration of each model. These vibrations were introduced by a small initial excitation of the modes included. In addition to the steady and unsteady forces, the evolution of the generalised coordinates over time was compared as well. The simulations were performed for two different reduced frequencies and showed no notable differences in the results between the modal and linearised solver. It was found, however, that the consideration of the acceleration term is mandatory as it accounts for almost half of the unsteady forces. The neglect of these forces would clearly lead to a different dynamic behaviour of the wing. This would inevitably produce incorrect results in the stability analysis. The verification test case was finally applied to the full Pazy wing structural model using the four lowest natural modes. The results of the forces as well as the generalised coordinates showed very good agreement with only small differences appearing in the generalised coordinate of the first out-of-plane bending mode. Thus, the derived linear aeroelastic model was successfully verified for the undeformed case.

After completing the development and verification of the linear models used for the stability analysis, the focus was set on the Pazy wing test case. Static coupling simulations were performed at first for onflow velocities of 30, 40 and 50 m/s and angles of attack ranging from 1 to 10 degrees. The displacements were evaluated at 33 equidistant points located at 44.75% chord in order to be able to compare the results to computational data provided by the Imperial College group. For the lowest onflow velocity, the influence of geometric nonlinearities was found to be rather small, although the maximum tip displacement reached 17% with respect to the wing span. However, the necessity for an application of a geometrically nonlinear solution method for this test case was clearly highlighted at higher velocities. This was emphasised by the maximum tip displacement of 47% with respect to the wing span, which represents a highly nonlinear regime indicated also by the considerable displacement in spanwise direction. Compared to the wing considered as perfectly rigid, the high elasticity of the wing leads to a considerable change in lift distribution. It could be noticed that the maximum loads occur on the outer wing at low angles of attack, but shift towards the wing root with increasing angle of attack. Furthermore, a significant increase in total lift forces was observed due to the elastic deformation of the wing, ranging from 14% to 30% for the highest onflow velocity. Following the static coupling simulations, the influence of the geometric nonlinearities on the structural properties, such as eigenvalues and eigenvectors, was investigated. These were obtained from a modal analysis in Nastran, which was performed on the deformed structure computed from the static coupling simulations. The eigenvalues were then plotted as a function of the

normalised tip displacement. Significant changes appeared mainly in the frequencies of the third and the fifth mode, which are the first torsion and first in-plane bending mode. Both modes showed a decrease in frequency with increasing tip displacement, which was expected to affect the aeroelastic stability in the deformed case. This was particularly relevant for the first torsion mode, as its frequency reaches the frequency of the second out-of-plane mode at 30% tip displacement, which is within the normal operating range of the Pazy wing. The aeroelastic stability was determined subsequently by means of the proposed method. Simulations were performed for velocities ranging from 10 to 120 m/s for 0 degrees angle of attack and from 10 to 90 m/s for 1 to 5 degrees angle of attack. Root locus plots were used to present the eigenvalues in the complex plane, whereas the modes are regarded unstable when they cross from the left- to the right-hand plane. Significant changes in the evolution of the first three complex modes were mainly noticed between 0 and 2 degrees angle of attack. An evaluation of the frequency and damping trends revealed that the first flutter instability evolves from coupling of the first torsion with the second out-of-plane bending mode. The first flutter mode becomes stable again at higher onflow velocities and a second instability occurs, which incorporates 1st Torsion, 2nd OOP and 1st OOP bending. With increasing angle of attack, the flutter onset velocities of both instabilities are reduced due to the effects of geometric nonlinearities on the modal properties of the structure. Interestingly, the velocity range of the first flutter mode is reduced, which results in a region of stability between the first and the second flutter region above 10% tip displacement. This stable region expands as the angle of attack is increased. In addition, the flutter boundaries seemed to be restricted by a maximum tip displacement. A major drawback of the current implementation of stability analysis was found to be the neglect of forces in the flow direction. This caused an instability of the 1st IP bending mode, although this mode showed no contributions of other modes and thus can normally be regarded stable.

The validation of the proposed method for stability analysis was first performed using the aeroelastic flutter solution sequence SOL145 in Nastran. As the Nastran aeroelastic solution sequences are limited to small deformations, the results could only be compared for the undeformed case. Nevertheless, a validation by means of this solver seemed favourable, since deviations due to a model mismatch were prevented by using the same full FE model. The velocities as well as the frequencies were in very good agreement for all three flutter points, with only small deviations of 2% in the 1st flutter velocity. The third instability probably represents torsional divergence and is only observed due to the larger velocity range investigated. Regarding the frequency trends of both solutions, no considerable deviations were found. Consequently, the

proposed method was proved to be valid for the undeformed wing. The results of the static coupling simulations and the stability analysis of the deformed wing were validated with data from the Imperial College group. These were computed using an equivalent beam model rather than the full FE model. The emerging differences in the displacement fields were within a tolerable range of 6% and could be attributed to the different modelling approaches. Larger deviations had to be noticed in the flutter onset velocities. Especially the velocities of the first flutter mode already showed a considerable discrepancy for the undeformed wing. This was likely caused by a mismatch between the beam and the full FE model, which was first discovered when comparing the deflections from the static coupling simulations. The deviations in the first flutter instability, however, remained almost in the same magnitude for all angles of attack investigated. In contrast, a significant diverging behaviour was found for the second flutter onset velocity above 1 degree angle of attack. A reason for this could not be determined, although it might possibly involve the influence of geometric nonlinearities due to the occurring large deformations.

Overall, it could be demonstrated that the linear state-space models developed are suitable to describe the dynamic behaviour due to small disturbances at static equilibrium points. In addition, the proposed method for stability analysis seems to provide reliable results for an undeformed wing, although further investigations for large deformations are inevitable.

5.2 Outlook and Future Research

Several shortcomings of the proposed method were discovered during the application to the Pazy wing test case. Especially the lack of forces acting in the flow direction clearly affects the stability of modes involving in-plane motions. Hence, the integration of (induced) drag forces into the linearised aerodynamic state-space model is preferable to overcome this problem. For the aeroelastic state-space model the treatment of the acceleration term leaves room for improvement. This is approximated using a first order difference scheme in the current implementation. However, the acceleration of the generalised coordinates can be obtained directly from the structural state-space model in continuous-time formulation. Although the inclusion of this analytical solution for the acceleration would lead to higher accuracy, only small differences are to be expected. In this context, it would be interesting to investigate how the results of the stability analysis are affected when the unsteady acceleration term is neglected. Another aspect is the verification of the linearised aeroelastic model. In this thesis this

was only performed for the undeformed wing, but should also be done for the deformed structure in the future, especially at large deformations. Regarding the eigenvalue analysis of the dynamics matrix, a problem identified is the imbalance between the number of aerodynamic and structural states. A method for model order reduction should therefore be implemented in order to reduce the large number of aerodynamic states and save computational costs.

Concerning the Pazy wing test case, the goal of validating the simulation results with experimental data has not yet been achieved, but will therefore have high priority in the future. In this context, a drawback of the full FE model used was the behaviour of the shell elements modelling the skin. As these exhibited buckling even at small out-of-plane deformations, all simulations presented in this thesis were performed using the model without skin. A very simple way to consider the stiffness of the skin would be a modification of the thickness of the aluminum spar or its material properties, such as Young's modulus. Nevertheless, it seems reasonable to investigate how the skin and its prestressing could actually be included in the model, e.g. by applying a thermal simulation in a preprocessing step. Another aspect identified during the wind tunnel test campaign at Technion was the possible influence of wind tunnel walls on the experimental results, as the wing approaches the walls when undergoing large deformations. This could also be modelled in the vortex lattice solver, but is seen as a secondary feature. Regarding the results of the stability analysis of the Pazy wing, the extension of the proposed method to investigate limit cycle oscillations seems useful. Finally, the developed method could also be enhanced to describe the behaviour of the free-flying aircraft.

Appendix A

A.1 Vectors and Equivalent Matrices of the Linearised Aerodynamic Model

In the following, the transformation of the vectors ${}^{q|c}\boldsymbol{V}_{rb}$, $\boldsymbol{n}$ and the matrix $\boldsymbol{R}$ into equivalent matrices mentioned in Section 3.2.2 is discussed. This transformation is necessary to allow matrix multiplication and to ensure that the resulting matrices of the state-space model are of the correct dimension. In general, the vector $\boldsymbol{V}_{rb}$ and $\boldsymbol{n}$ are column vectors of dimension $3n_b$ containing the velocity or normal vector components of each (bound) aerodynamic panel. The equivalent matrix $\tilde{\boldsymbol{V}}_{rb}$ is of dimension $3n_b \times n_b$ and includes the velocity vector $\boldsymbol{V}_{rb,i}$ of each panel in diagonal form:

$$\boldsymbol{V}_{rb} = \begin{Bmatrix} {}^{x}V_{rb,1} \\ {}^{y}V_{rb,1} \\ {}^{z}V_{rb,1} \\ {}^{x}V_{rb,2} \\ {}^{y}V_{rb,2} \\ {}^{z}V_{rb,2} \\ \vdots \\ {}^{z}V_{rb,n_b} \end{Bmatrix}, \qquad \tilde{\boldsymbol{V}}_{rb} = \begin{bmatrix} {}^{x}V_{rb,1} & 0 & \dots & 0 \\ {}^{y}V_{rb,1} & 0 & \dots & 0 \\ {}^{z}V_{rb,1} & 0 & \dots & 0 \\ 0 & {}^{x}V_{rb,2} & \dots & 0 \\ 0 & {}^{y}V_{rb,2} & \dots & 0 \\ 0 & {}^{z}V_{rb,2} & \dots & 0 \\ \vdots & 0 & \ddots & \vdots \\ 0 & \dots & 0 & {}^{z}V_{rb,n_b} \end{bmatrix}. \tag{A.1}$$

The equivalent matrix $\tilde{\boldsymbol{n}}$ for the panel normal vectors $\boldsymbol{n}$ is found in the same manner. Concerning the skew-symmetric matrix $\boldsymbol{R}$ representing the cross-product with the vector $\boldsymbol{r}$, its equivalent matrix $\tilde{\boldsymbol{R}}$ is of dimension $3n_b \times 3n_b$. It comprises the skew-

symmetric matrix $\boldsymbol{R}_i$ of each panel in block diagonal form:

$$\boldsymbol{R}_i = \begin{bmatrix} 0 & -r_z & r_y \\ r_z & 0 & -r_x \\ -r_y & r_x & 0 \end{bmatrix}, \qquad \tilde{\boldsymbol{R}} = \begin{bmatrix} \boldsymbol{R}_1 & 0 & \dots & 0 \\ 0 & \boldsymbol{R}_2 & \dots & 0 \\ \vdots & \vdots & \ddots & \vdots \\ 0 & 0 & \dots & \boldsymbol{R}_{n_b} \end{bmatrix}. \tag{A.2}$$

A.2 Matrices for the Calculation of the Euler Angles

A brief description of the Euler angles illustrated for the Pazy wing test case in Section 4.2.2 is supplemented here. Generally, the Euler angles are used to describe the orientation of a (local) coordinate system B relative to a reference system A. In this particular case, the angles ϕ, θ and ψ specify the orientation of the local body-fixed coordinate systems at each of the 33 evaluation points with respect to the global body-fixed coordinate system of the undeformed wing. Concerning the chosen X'Y'Z' convention, the angle ϕ describes a rotation around the x' axis of the local system, which is naturally coincident with the x axis of the reference system at the beginning of the operation. Subsequently, the angles θ and ψ represent rotations around the y' and the z' axis of the local system, as shown in Fig. A.1. In most cases, the Euler angles are given and the orientation of the local system can be found using a so-called *rotation matrix* ${}^{A}_{B}\boldsymbol{R}$. This matrix contains column-wise the unit vectors giving the principal directions of the local coordinate system B in terms of the reference system A. However, here the orientation of the local systems is known and the Euler angles are to be determined. For this particular case, the rotation matrix is simply established

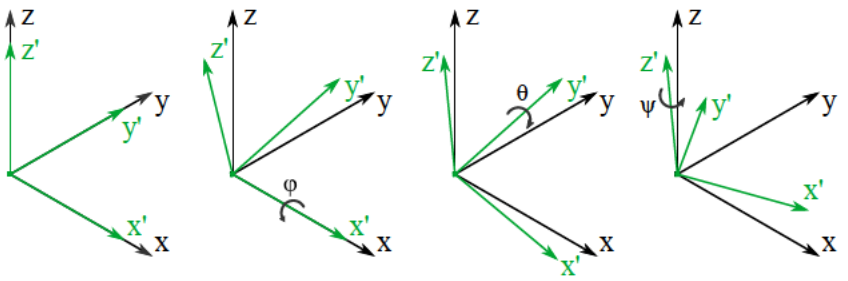

Figure A.1: Geometrical definition of the Euler angles according to the X'Y'Z' convention; Reference coordinate system A in black and local (rotated) coordinate system B in green

using the unit vectors ${}^{A}\hat{\boldsymbol{x}}_B$, ${}^{A}\hat{\boldsymbol{y}}_B$ and ${}^{A}\hat{\boldsymbol{z}}_B$, which represent the axis directions of the body-fixed system B with respect to system A. By application of the X'Y'Z' convention for this rotation matrix, which is [37]

$$
{}^{A}_{B}\boldsymbol{R}_{X'Y'Z'}(\phi,\theta,\psi) = \begin{bmatrix} {}^{A}\hat{\boldsymbol{x}}_B & {}^{A}\hat{\boldsymbol{y}}_B & {}^{A}\hat{\boldsymbol{z}}_B \end{bmatrix} = \begin{bmatrix} r_{11} & r_{12} & r_{13} \\ r_{21} & r_{22} & r_{23} \\ r_{31} & r_{32} & r_{33} \end{bmatrix} \tag{A.3}
$$

$$
= \begin{bmatrix} \cos\theta\cos\psi & -\cos\theta\sin\psi & \sin\theta \\ \sin\phi\sin\theta\cos\psi + \cos\phi\sin\psi & -\sin\phi\sin\theta\sin\psi + \cos\phi\cos\psi & -\sin\phi\cos\theta \\ -\cos\phi\sin\theta\cos\psi + \sin\phi\sin\psi & \cos\phi\sin\theta\sin\psi + \sin\phi\cos\psi & \cos\phi\cos\theta \end{bmatrix},
$$

the Euler angles can then be calculated by

$$\phi = \arctan2(-r_{23}, r_{33}) \,, \tag{A.4a}$$

$$\theta = \arctan2(r_{21}, r_{11}) \,, \tag{A.4b}$$

$$\psi = \arcsin r_{13} \,. \tag{A.4c}$$

Bibliography

[1] Lee, D. S., et al. The contribution of global aviation to anthropogenic climate forcing for 2000 to 2018. *Atmospheric environment (Oxford, England : 1994)*, 2020.

[2] International Civil Aviation Organization. Resolution A 39-3: Consolidated statement of continuing icao policies and practices related to environmental protection - Global Market-based Measure (MBM) scheme, October 2016.

[3] International Civil Aviation Organization. 2019 environmental report: Aviation and environment. URL: `https://www.icao.int/environmental-protection/Pages/envrep2019.aspx` [cited 10/12/2020].

[4] Airbus. ZeroE: Towards the world's first zero-emission commercial aircraft, 09/21/2020. URL: `https://www.airbus.com/innovation/zero-emission/hydrogen/zeroe.html` [cited 10/01/2020].

[5] Ritter, M., Dillinger, J. and Meddaikar, Y. M. Static and dynamic aeroelastic validation of a flexible forward swept composite wing. In *58th AIAA/ASCE/AHS/ASC Structures, Structural Dynamics, and Materials Conference*, Reston, Virginia, 2017. American Institute of Aeronautics and Astronautics.

[6] Avin, O., Drachinsky, A., Ben-Shmuel, Y. and Raveh, D. Design of an experimental benchmark of a highly flexible wing. In *60th Israel Annual Conference on Aerospace Sciences*. Tel Aviv, 2020.

[7] Zimmer, M. Integral design and optimisation process for a highly flexible generic long range jet transport with flight mechanic derivative constraints. In *AIAA Scitech 2021 Forum*, Reston, Virginia, 2021. American Institute of Aeronautics and Astronautics.

[8] Ritter, M. *An Extended Modal Approach for Nonlinear Aeroelastic Simulations of Highly Flexible Aircraft Structures*. PhD thesis, TU Berlin, 2018.

[9] Noll, T. E., et al. Investigation of the helios prototype aircraft mishap: Volume I mishap report. NASA Langley Research Center, 2001.

[10] Ritter, M., Cesnik, C. E. and Krüger, W. R. An enhanced modal approach for large deformation modeling of wing-like structures. In *56th AIAA/ASCE/AHS/ASC Structures, Structural Dynamics, and Materials Conference*, Reston, Virginia, 2015. American Institute of Aeronautics and Astronautics.

[11] Cea, A. and Palacios, R. Nonlinear modal aeroelastic analysis from large industrial-scale models. In *AIAA Scitech 2019 Forum*, Reston, Virginia, 2019. American Institute of Aeronautics and Astronautics.

[12] Bisplinghoff, R. L., Ashley, H. and Halfman, R. L. *Aeroelasticity*. Dover Books on Aeronautical Engineering. Dover Publications, Newburyport, 2013.

[13] Wright, J. R. and Cooper, J. E. *Introduction to aircraft aeroelasticity and loads*. Aerospace series. Wiley, Chichester, repr. edition, 2008.

[14] Collar, A. R. The expanding domain of aeroelasticity. *The Aeronautical Journal*, 50(428):613–636, 1946.

[15] Hodges, D. H. and Pierce, G. A. *Introduction to structural dynamics and aeroelasticity*, volume 15 of *Cambridge aerospace series*. Cambridge University Press, Cambridge, second edition, 2011.

[16] Murua, J., Palacios, R. and Graham, J. M. R. Applications of the unsteady vortex-lattice method in aircraft aeroelasticity and flight dynamics. *Progress in Aerospace Sciences*, 55:46–72, 2012.

[17] Katz, J. and Plotkin, A. *Low speed aerodynamics*, volume 13 of *Cambridge aerospace series*. Cambridge University Press, Cambridge, second edition, 2001.

[18] Bathe, K.-J. *Finite element procedures*. Prentice Hall, Englewood Cliffs, NJ, 1996.

[19] MSC Software. *MSC Nastran 2017: Nonlinear User's Guide SOL 400*. MacNeal-Schwendler Corporation, 2016.

[20] Freymann, R. *Strukturdynamik: Ein anwendungsorientiertes Lehrbuch*. Springer-Verlag Berlin Heidelberg, 2011.

[21] Degroote, J., Bathe, K.-J. and Vierendeels, J. Performance of a new partitioned procedure versus a monolithic procedure in fluid–structure interaction. *Computers & Structures*, 87(11-12):793–801, 2009.

[22] Mayr, M., Klöppel, T., Wall, W. A. and Gee, M. W. A temporal consistent monolithic approach to fluid-structure interaction enabling single field predictors. *SIAM Journal on Scientific Computing*, 37(1):B30–B59, 2015.

[23] Mauermann, T. *Flexible Aircraft Modelling for Flight Loads Analysis of Wake Vortex Encounters*. PhD thesis, TU Braunschweig, 2010.

[24] Beckert, A. and Wendland, H. Multivariate interpolation for fluid-structure-interaction problems using radial basis functions. *Aerospace Science and Technology*, 5(2):125–134, 2001.

[25] Ritter, M., Hilger, J. and Zimmer, M. Static and dynamic simulations of the Pazy wing aeroelastic benchmark by nonlinear potential aerodynamics and detailed FE model. In *AIAA Scitech 2021 Forum*, Reston, Virginia, 2021. American Institute of Aeronautics and Astronautics.

[26] Patil, M. J., Hodges, D. H. and Cesnik, C. E. S. Nonlinear aeroelastic analysis of aircraft with high-aspect-ratio wings. In *39th Structures, Structural Dynamics and Materials Conference*, 1998.

[27] Patil, M. J., Hodges, D. H. and Cesnik, C. E. S. Nonlinear aeroelasticity and flight dynamics of high-altitude long-endurance aircraft. *Journal of Aircraft*, 38(1):88–94, 2001.

[28] Xie, C., Liu, Y., Yang, C. and Cooper, J. E. Geometrically nonlinear aeroelastic stability analysis and wind tunnel test validation of a very flexible wing. *Shock and Vibration*, 2016(3):1–17, 2016.

[29] Murua, J. *Flexible Aircraft Dynamics with a Geometrically-Nonlinear Description of the Unsteady Aerodynamics*. PhD thesis, Imperial College London, 2012.

[30] Åström, K. J. and Murray, R. M. *Feedback systems: An introduction for scientists and engineers*. Princeton Univ. Press, Princeton, NJ, 2008.

[31] Schulz, G. and Graf, C. *Regelungstechnik 2: Mehrgrößenregelung, Digitale Regelungstechnik, Fuzzy-Regelung*. De Gruyter, München, 3. aufl. edition, 2013.

[32] MSC Software. *MSC Nastran 2012 Quick Reference Guide*. MacNeal-Schwendler Corporation, 2011.

[33] SAE International. Guidelines for development of civil aircraft and systems ARP4754A. S-18 Aircraft and Sys Dev and Safety Assessment Committee, 2010.

[34] Sargent, R. G. Verification and validation of simulation models. In *Simulation Conference (WSC), Proceedings of the 2010 Winter*, pages 166–183, Piscataway, N.J., 2010. IEEE.

[35] Avin, O., Raveh, D. E., Drachinsky, A. and Ben-Shmuel, Y. An experimental benchmark of a very flexible wing. In *AIAA Scitech 2021 Forum*, Reston, Virginia, 2021. American Institute of Aeronautics and Astronautics.

[36] Goldstein, H., Poole, C. P. and Safko, J. L. *Classical mechanics*. Addison Wesley, San Francisco, NJ, 3. ed. edition, 2002.

[37] Craig, J. J. *Introduction to robotics: Mechanics and control*. Pearson education international. Pearson Prentice Hall, Upper Saddle River, NJ, international edition, 2005.

[38] Norton, W. J. Structures flight test handbook. Air Force Flight Test Center Edwards Air Force Base, 1990.

[39] Albano, E. and Rodden, W. P. A doublet-lattice method for calculating lift distributions on oscillating surfaces in subsonic flows. *AIAA Journal*, 7(2):279–285, 1969.

[40] MSC Software. *MSC Nastran Version 68 Aeroelastic Analysis User's Guide*. MacNeal-Schwendler Corporation, 2014.

[41] del Carre, A., Muñoz-Simón, A., Goizueta, N. and Palacios, R. Sharpy: A dynamic aeroelastic simulation toolbox for very flexible aircraft and wind turbines. *Journal of Open Source Software*, 4(44):1885, 2019.

[42] del Carre, A., Goizueta, N., Muñoz-Simón, A. and Palacios, R. Simulation of high aspect ratio planes in python [sharpy] — sharpy 1.2 documentation, 2020. URL: `https://ic-sharpy.readthedocs.io/en/master/index.html#` [cited 18.12.2020].

[43] GitHub. Imperialcollegelondon/sharpy Github repository, 2020. URL: `https://github.com/imperialcollegelondon/sharpy` [cited 18.12.2020].

[44] Goizueta, N., Drachinsky, A. and Wynn, A. and Raveh, D. E., and Palacios, R. Flutter predictions for very flexible wing wind tunnel test. In *AIAA Scitech 2021 Forum*, Reston, Virginia, 2021. American Institute of Aeronautics and Astronautics.

Hochschule für Angewandte Wissenschaften Hamburg
Hamburg University of Applied Sciences

Erklärung zur selbstständigen Bearbeitung einer Abschlussarbeit

Gemäß der Allgemeinen Prüfungs- und Studienordnung ist zusammen mit der Abschlussarbeit eine schriftliche Erklärung abzugeben, in der der Studierende bestätigt, dass die Abschlussarbeit „– bei einer Gruppenarbeit die entsprechend gekennzeichneten Teile der Arbeit [(§ 18 Abs. 1 APSO-TI-BM bzw. § 21 Abs. 1 APSO-INGI)] – ohne fremde Hilfe selbständig verfasst und nur die angegebenen Quellen und Hilfsmittel benutzt wurden. Wörtlich oder dem Sinn nach aus anderen Werken entnommene Stellen sind unter Angabe der Quellen kenntlich zu machen."

Quelle: § 16 Abs. 5 APSO-TI-BM bzw. § 15 Abs. 6 APSO-INGI

Dieses Blatt, mit der folgenden Erklärung, ist nach Fertigstellung der Abschlussarbeit durch den Studierenden auszufüllen und jeweils mit Originalunterschrift als letztes Blatt in das Prüfungsexemplar der Abschlussarbeit einzubinden.
Eine unrichtig abgegebene Erklärung kann -auch nachträglich- zur Ungültigkeit des Studienabschlusses führen.

Erklärung zur selbstständigen Bearbeitung der Arbeit

Hiermit versichere ich,

Name: Hilger

Vorname: Jonathan

dass ich die vorliegende Masterarbeit bzw. bei einer Gruppenarbeit die entsprechend gekennzeichneten Teile der Arbeit – mit dem Thema:

Nonlinear Aeroelastic Simulations and Stability Analysis of a Highly Flexible Wing

ohne fremde Hilfe selbständig verfasst und nur die angegebenen Quellen und Hilfsmittel benutzt habe. Wörtlich oder dem Sinn nach aus anderen Werken entnommene Stellen sind unter Angabe der Quellen kenntlich gemacht.

- die folgende Aussage ist bei Gruppenarbeiten auszufüllen und entfällt bei Einzelarbeiten -

Die Kennzeichnung der von mir erstellten und verantworteten Teile der -bitte auswählen- ist erfolgt durch:

Hamburg	28.01.2020	[redacted]
Ort	Datum	Unterschrift im Original